

**Alloy design of Bi systems for high temperature solders
and their characterizations**

(高温はんだ用 Bi 系合金の設計と特性評価)

July 2018

Meiqi Yu

CONTENTS

Chapter 1 Background and objectives

1.1 Introduction	2
1.2 Development of high-temperature solders	4
1.2.1 Pb-Sn solder alloys.....	6
1.2.2 Au-based solder alloys.....	7
1.2.2.1 Au-Sn	7
1.2.2.2 Au-Ge.....	8
1.2.3 Zn-based solder alloys.....	9
1.2.3.1 Zn-Al.....	9
1.2.3.2 Zn-Sn.....	10
1.2.4 Bi-based solder alloys	11
1.3 Development of alloy design methods	13
1.3.1 Semi-empirical mode material design calculation method	13
1.3.2 Thermodynamic auxiliary solder design	14
1.3.3 Molecular orbital theory calculation and design method	15
1.3.3.1 Ab initio molecular orbital method	15
1.3.3.2 DV-X α cluster method	16
1.4 Objective of this study.....	19
References.....	21

Chapter 2 The relation between electronic parameter and mechanical properties for Bi alloys

2.1 Introduction	28
2.2 Composition of alloys	30
2.2.1 Electronic parameter representing alloying effects	30
2.2.2 Selection of experimentally alloys	33
2.3 Experimental procedure	34
2.3.1 Materials and manufacturing process.....	34
2.3.2 Evaluation of some properties.....	36

2.4 Results and discussion.....	38
2.4.1 Microstructures	38
2.4.2 Characteristics on binary Bi-Cu/Ag/Zn alloys at 293 K.....	40
2.4.2.1 Tensile properties at 293 K	40
2.4.2.2 ΔM_k parameter and mechanical properties.....	45
2.4.3 Tensile properties on binary Bi-Cu/Ag/Zn alloys at 423 K.....	48
2.5 Summary.....	54
References.....	55

Chapter 3 Promising compositions of Bi alloys and their characterizations

3.1 Introduction	58
3.2 Experimental procedure	60
3.2.1 Materials and manufacturing process.....	60
3.2.2 Evaluation of some properties.....	60
3.3 Results and discussion.....	68
3.3.1 Microstructures	68
3.3.2 Mechanical properties on ternary alloys.....	69
3.3.2.1 Tensile properties at 293 K	69
3.3.2.2 Temperature dependence of tensile properties.....	70
3.3.2.3 Relation between mechanical properties and ΔM_k	74
3.3.3 Melting points.....	77
3.3.4 Wettability.....	78
3.3.5 Thermal conductivity.....	80
3.4 Summary.....	81
References.....	82

Chapter 4 Practical applications of high temperature solders

4.1 Introduction	86
4.2 Experimental procedure	88
4.2.1 Materials and manufacturing process.....	88
4.2.2 Evaluation of some properties.....	88
4.3 Results and discussion.....	92
4.3.1 Heat cycle behaviors	92

4.3.1.1 Comparison of Bi system alloy and practically used alloys in heat cycle measurements	92
4.3.1.2 Microstructures of solder/Cu diffusion couples	99
4.3.1.3 Growth behavior of intermetallic compounds	105
4.3.1.4 Diffusion mechanism between solder alloys and Cu	108
4.3.2 Shearing test of Bi-5.0Ag-0.5Cu and Cu substrates with Bi coating	111
4.3.3 Comparison between promising alloys and Pb-xSn alloys in view of soldering	114
4.4 Summary	116
References	117
Chapter 5 Conclusions	119
Acknowledgements	123
Published papers in regards to this thesis	124
Presentations	125

Chapter 1

Background and objectives

1.1	Introduction.....	2
1.2	Development of high-temperature solders	4
1.2.1	Pb-Sn solder alloys	6
1.2.2	Au-based solder alloys.....	7
1.2.2.1	Au-Sn	7
1.2.2.2	Au-Ge.....	8
1.2.3	Zn-based solder alloys	9
1.2.3.1	Zn-Al.....	9
1.2.3.2	Zn-Sn	10
1.2.4	Bi-based solder alloys.....	11
1.3	Development of alloy design methods.....	13
1.3.1	Semi-empirical mode material design calculation method.....	13
1.3.2	Thermodynamic auxiliary solder design.....	14
1.3.3	Molecular orbital theory calculation and design method.....	15
1.3.3.1	Ab initio molecular orbital method	15
1.3.3.2	DV-X α cluster method	16
1.4	Objectives of this study	19
	References.....	21

1.1 Introduction

High-temperature solders are extensively utilized as die-attach solders in power semiconductor packaging, chip connections, solder ball connections, the bonding of semiconductor devices on to solder alloys and so on ^{1, 2)}. The application of power-electronics are extended to various automobile, aerospace, energy production and military industries ³⁻⁶⁾. For a long time, Pb-Sn solder alloy with a Pb content of 85-97 mass.% Pb are the currently used as high-temperature solders in high-temperature applications ⁷⁻¹⁰⁾. Pb-5Sn and Pb-10Sn are the common compositions of Pb-Sn high-temperature solders, which having melting ranges of 573-587 K and 541-574 K, respectively ⁴⁾. The microstructures of the high-lead content solders are very stable and both aging temperature and aging duration has little effect on the microstructures ¹¹⁾. The microstructure with any intermetallic compounds (IMCs) makes the wide applications of high-lead content solders. Furthermore, because of the stability of the lead oxide layer and the small galvanic potential difference between Pb and Sn, the corrosion does not impact the reliability of high-lead content solders ^{12, 13)}.

High-lead content solders are an extremely soft alloy. The high-lead content solders exhibit excellent fatigue resistance, because of the softness of the alloy makes the joint structure keep reliable by relaxation of the thermal stresses ^{14, 15)}. On the other hand, the softness of high-lead content solders lead to thermo-mechanical failure by creep. In summary, high-lead content solders are considered to be the ideal choice of high-temperature solders due to the good wettability, thermal conductivity, fatigue resistance, reliability and low cost ^{16, 17)}.

In late 20th century, because of the protection of the environment has attracted worldwide attention with the continuous improvement of living standards, the use of Pb was limited ¹⁸⁾. Pb is a heavy metal element. It is easy to accumulate in the human body, especially the combination of lead ions and proteins, which would inhibit the normalization of protein. Moreover, lead ions are also vulnerable to human nervous system, that causing mental disorders. Lead is more harmful to infants and children. It will destroy their intelligence quotient and normal development. In 1998, Japan revised the law on the recycling of home electronics to promote the development of lead-free

electronics ¹⁹⁾. In June 2000, the Association Connecting Electronics Industries (IPC) published the 4th edition of Lead-Free Roadmap, which advising the US companies to launch lead-free electronics in 2001 and prohibit lead content electronics in 2004 ²⁰⁾. In February 2003, WEEE (Waste Electrical and Electronic Equipment) and RoHS (EU Directive on the Restriction of the use of certain Hazardous Substances in electrical and electronic equipment) orders are formally approved. These orders require the electrical and electronic equipment sold in Europe become lead-free ²⁰⁾. In December 2015, the European Commission adopted a new Circular Economy Package, which included the new orders of WEEE and RoHS. The species of the lead-free electrical and electronic equipment are increasing in Europe (e.g. for medical equipment, monitoring and control equipment, external diagnostic medical device). Moreover, the recycling rate of the electrical and electronic products are also increase. From 2019, the minimum recycling rate of each member country needs to reach each year shall account for 65% of the average weight of EEE put into the market in the previous three years, or 85% of the total weight of end-of-life EEE produced by each member country. Therefore, the establishment of lead-free solders has been an inevitable trend in the electronics industry.

Despite significant research and a large number of papers on lead-free solders published in recent years, only few reports on the research and development of high-temperature lead-free solders ⁵⁾. This is because the volume of high-lead content solders used is very little compared with the volume the eutectic Sn-Pb solder alloy. However, with the advent of high-temperature applications, the demand for high-temperature lead-free solders will be increasing sharply ⁴⁾. Thus, the research of high-temperature lead-free solders in electronic industry has great practical significance.

1.2 Development of high-temperature lead-free solders

The current choices for high-temperature solders are derived from Au–Sn, Au–Ge, Zn–Al, Zn–Sn, and Bi–Ag solder alloys, as well as some other solder alloy systems. In order to protect the environment and improve the reliability of products, the high-temperature lead-free solder alternatives should satisfy the following conditions.

Firstly, in designing of high-temperature lead-free solder alloys, the melting behavior is one of the basic critical. The solidus temperature should be higher than 533 K, so that the solder will no melting until it passes secondary reflow at 523 K. And the liquidus temperature should be below 673 K, due to the limitation of the glass transition temperature of the polymers used in the substrate as dielectric materials. Therefore, the melting temperature range (533-623 K) has been defined by the industries in order to ensure efficient process control ²¹⁾. Table 1.1 summarized the melting temperature of typical high-temperature solder alloys.

Table 1.1 Melting temperatures for typical high-temperature solder alloys.

Alloys	Composition (mass.%)	Solidus temperature (K)	Liquidus temperature (K)	References
Pb-Sn	Pb-37Sn	456	521	4
	Pb-30Sn	456	521	
	Pb-20Sn	456	552	
	Pb-10Sn	541	574	
	Pb-5Sn	573	587	
	Pb-2Sn	589	595	
Au-Sn	Au-20Sn	553	553	5
	Au-95Sn	488-490	488-490	33
Au-Ge	Au-28Ge	633	633	68
Zn-Al	Zn-6Al	654	654	4, 5
	Zn-4Al-3Mg-3.2Ga	582	620	80
Zn-Sn	Zn-20Sn	471	656	45
	Zn-30Sn	471	656	
	Zn-40Sn	471	638	
Bi-Ag	Bi-2.5Ag	535.5	535.5	75
	Bi-11Ag	534.4	653.6	14

Secondly, the joints should have excellent mechanical properties. For the high temperature lead-free solder joints formed, the high service temperature makes the joints prone to fatigue and creep failure. In the first-level packaging like chip connections, the joints not only need to meet connection strength, but also should have a lower shear modulus to ensure the good stability and reliability of the electronics at higher service temperature.

Thirdly, the high-temperature lead-free solders should have good fluidity of liquid solder and good wettability between substrates and solders. Moreover, because of the high service temperature and current density for solder joints, good thermal conductivity ($>20 \text{ W}\cdot\text{K}^{-1}\cdot\text{m}^{-1}$) and low electrical resistivity ($<100 \mu\Omega\cdot\text{cm}$) are also basic requirements of high-temperature lead-free solders.

Fourthly, the high-temperature lead-free solders should have the similar coefficient of thermal expansion (CTE) between die and substrate. Due to the different coefficient of thermal expansion between chips and substrates, thermal stress is prone to occur during the thermal cycles in the service process. That may lead to the final failure of electronic components.

Fifthly, the high-temperature lead-free solders should have good workability, that easy to processed into wire, ribbon, or powder for the preparation of solder paste and so on, to meet the different requirements of automated brazing process.

At last, the high-temperature lead-free solders should be non-toxic, pollution-free and appropriate cost. Especially for the new lead-free interconnect technology instead of reflow soldering, the process temperature should be not higher than the existing brazing process temperature and hope to further reduce. Moreover, the solders can make heavy use of existing equipment and improve the degree of automation.

The research on properties such as the melting and solidification behavior²²⁻²⁷⁾, microstructures²⁸⁻³⁷⁾, interfacial compounds and structures³⁸⁻⁴⁹⁾, mechanical properties^{26, 50-56)} and reliability⁵⁷⁻⁶⁴⁾ of the alternatives for high-temperature lead-free solder alloys were introduced in the following.

1.2.1 Pb-Sn solder alloys

High-lead containing solders have been commonly used as high-temperature solders. Common compositions are Pb-5Sn and Pb-10Sn. In the case of high-lead content solders, the concentration of Sn influenced the formation and growth of interfacial intermetallics between the solder and substrate interface^{9, 65, 66}). Wang et al reported that the wettability between Pb-xSn and Cu substrate were improved with the content of Sn. Moreover, an IMC was occurred between high-lead solders and Cu substrate⁶⁷⁻⁶⁹). There was a spalling phenomenon between Cu substrate and Cu₃Sn of IMC layer, which is result of the high interfacial free energy between Cu and Cu₃Sn⁶⁹). The spalling formed from the Pb-rich regions between Cu and Cu₃Sn layer⁶⁷). And the spalling region grow with the increasing reaction time⁶⁷). The Sn in the Pb-Sn alloy formed the IMC with the Cu substrate. Due to the decrease of Sn content in Pb-Sn alloy, the local thermodynamic equilibrium between Cu substrate and Cu₃Sn was broken⁶⁷). And then the spalling becomes continuous. The grown of spalling also depend on the Sn content in the solder. With the lower Sn contents of 0.5 and 1 mass.%, the solder had already spalled with Cu substrate after 20 min, however, with the higher Sn contents of 3 and 5 mass.%, the spalling was not finished after 600 min⁶⁸). It is considered that the Pb atoms penetrating the Cu₃Sn layer through the grain boundary lead to the slower spalling rate of Cu₃Sn^{67, 68}).

In recent years, with the decreasing scale of chip, the solder joints to connect the chip and substrate become smaller and smaller. Moreover, because of the increasing electrical power for chip, the solder joints should have good mechanical properties and high reliability. The creep and fatigue were most common reason of the failures for high temperature solders. The high temperature creep behavior of Pb-5In, Pb-5Sn-2.5Ag, Pb-3Sn-2Ag-2In was investigated by Schoeller et al⁷⁰). It revealed that the stress exponent of these alloys was between 3 and 8. The change of the stress exponent with temperature was based on the rate controlling mechanism for dislocation creep⁷⁰). A transition in the controlling mechanism from pipe to lattice diffusion was observed around $0.7T_m$, where T_m is the melting point of the solder alloys⁷⁰).

In present, high-lead containing solders are still widely used in high temperature

applications. The mechanical properties like tensile property, creep property, fatigue behavior and so on were investigated by many researchers. The reports of possible alternatives for high-temperature lead-free solders were listed below.

1.2.2 Au-based solder alloys

Au-based solder alloys exhibit high strength, excellent electrical and thermal conductivities, good resistance of corrosion and fatigue, which make them available to be high-temperature lead-free solder alloys.

1.2.2.1 Au-Sn

There are several compositions of Au-Sn system solder alloys satisfied the solidification criterion for high-temperature solders. The eutectic Au-Sn alloy Au-20Sn (mass. %) is commonly used in electronic and optoelectronic packaging^{23, 71}). The melting point of Au-20Sn is about 553 K, which fits the requirement of solidification behavior²⁸). Moreover, the results of T. Zhou et al show that the tensile strength, shear modulus, joint shear strength, electrical resistivity and thermal conductivity are 275 MPa, 25 GPa, 47.5 MPa, 0.164 $\mu\Omega\text{m}$ and 57 $\text{W}\cdot\text{K}^{-1}\cdot\text{m}^{-1}$, respectively⁵¹). Therefore, it is being considered as a high-temperature solder. Moreover, it also has excellent fatigue and creep resistance. F. Yost et al. employed the microstructural evolution of Au-20Sn solder alloy²⁹). The microstructure of the as-cast Au-20Sn solder alloy has ζ and ζ' Au_5Sn with the dendritic shape and eutectic of ζ - Au_5Sn and δ - AuSn at room temperature. The microstructure of Au-20Sn after thermally aged at 150 °C for 1 week was comprised some large Au_5Sn grains on the eutectic structure. In contrast, the microstructure of Au-20Sn after thermally aged at 473 K for 1 week was only contained ζ - Au_5Sn and δ - AuSn phases. The temperature near 473 K is the transforming temperature for ζ' Au_5Sn phase transformed into ζ - Au_5Sn phase. It considered that the ζ - and ζ' - Au_5Sn phases have different crystallography and properties, that ζ - Au_5Sn is more stable at higher temperatures. Because of the transformation, the thermal expansion and the moduli measurements are changed. That cause the cracking and decrease the joint reliability.

The reflow reactions of the Au-20Sn solder on a Cu substrate were investigated by H. M. Chung et al³²⁾. The eutectic of ζ -(Au, Cu)₅Sn and δ -(Au, Cu)Sn were observed in the microstructure of the solder when the reflow time was 60 s. Due to the Cu diffusion from the Cu substrate into the molten solder matrix, the dendritic ζ -(Au, Cu)₅Sn phase were grown after the reflow time of 60 min. In this system, because of the same behavior between Cu and Au, the composition of the solder changed from eutectic into hypo-eutectic with the increasing Cu concentration. This transformation is a eutectic reaction and a fine lamellar microstructure. On the other hand, both ζ -(Au, Cu)₅Sn and δ -(Au, Cu)Sn phases will grow during subsequent cooling. Therefore, the microstructure of fine lamellar eutectic and coarse eutectic was observed. It was also revealed that with the decreasing volume of the solder, the dendrites grew faster.

In addition, practical applications of Au-20Sn were also investigated^{55, 62, 72)}. Y. C. Liu et al study the effect of temperature from 298 to 473 K on hardness and creep behavior of Au-20Sn solder alloy⁶²⁾. This research reveals that the hardness of Au-20Sn decreases with the increasing temperature. Moreover, creep makes a large contribution to the plastic deformation during the nano-indentation process. G. S. Zhang et al compare the tensile creep behavior between Au-20Sn and Sn-37Pb solder alloys⁷²⁾. The results exhibit that compared with Sn-37Pb solder alloy, Au-20Sn solder alloy shows lower steady-state creep rates and better anti-creep performance.

1.2.2.2 Au-Ge

Au-Ge system solder alloys do not have intermetallic compounds (IMC) which is same with Pb-Sn system alloys. The eutectic melting point of Au-Ge composition is 633 K. It slightly deviates from the permissible liquidus temperature for high-temperature soldering. The addition of little amounts of Sb to Au-Ge system solder alloy would not only decrease the melting point, but also improve the ductility. Au-0.24Ge-0.05Sb is one of the promising candidate alloys for step soldering proposed by V. Chidambaram⁷³⁾. The microstructures of the Au-0.24Ge-0.05Sb solder alloy contain three phases: Au phase, Ge phase and AuSb₂ IMC. There is an age-softening effect of the Au-0.24Ge-0.05Sb solder alloy due to the expansion of Au phase. However, the softening effect

can be attributed to the refinement of the Ge phase that increase in hardness during aging. Soft matrix and hard dispersed phases would be ideal for applications demanding both creep and fatigue resistances. It was determined that the addition of In to the Au–Ge eutectic would further enhance the hardness of the alloy due to the effective lattice strains induced by the In atoms. Au-0.18Ge-0.10In solder alloy is a promising candidate alloy for applications for high strength, low elastic modulus and stability of microstructure at high-temperatures. The primary strengthening mechanism in the case of Au-Ge-In system alloys was determined to be solid solution strengthening

1.2.3 Zn-based solder alloys

Zn-based solder alloy is currently study by many research groups, mainly included Zn-Al, Zn-Sn system alloys and so on.

1.2.3.1 Zn-Al

Zn-Al system solder alloys are commonly used in the high-temperature range of high-temperature solder, the range of operating temperature is about 650-723 K^{5,34, 74}). Small additions of Cu, Sn, Mg and Ge into Zn-Al alloys would reduce the melting point of this alloy and make the alloys adhere to the required solidification criterion for high-temperature soldering^{36, 47, 75}). Interfacial reactions between Cu substrate and Zn-4Al and Zn-4Al-1Cu (mass.%) solder alloys during the temperature range from 693 to 803 K were investigated by Takaku et al⁴⁶). The growth of IMCs is considered to be controlled by volume diffusion during aging. The Cu₅Zn₈ phase was creating from substrate side and CuZn₄ phase from solder side. In particular, the growth rate of Cu₅Zn₈ was quite fast over 473 K. With the addition of Cu to Zn-4Al solders, the suppression of the consumption of the Cu substrate was observed, which resulted in a decrease of the activation energy of IMC growth and subsequently enhanced the growth of the IMC layers, particularly the Cu-Zn IMCs.

T. Shimizu et al investigate Zn-4Al-3Mg-3Ga solder alloy to replace Pb-5Sn solder alloy for the use of die-attaching⁷⁵). According to the research, the solidus and liquidus temperature of Zn-4Al-3Mg-3Ga solder alloy are 582 and 620 K, respectively. There

are never failure found in the temperature range from 208 to 423 K in the die-attaching test until 1000 cycles or at the atmosphere of 358 K and 85% humidity until 1000 h.

The microstructure and shear strength of the high-temperature Zn-4Al-3Mg-xSn (x= 0, 7 and 13 mass.%) solder alloys were investigated in the temperature range of 298-473 K by R. Mahmudi et al ⁷⁶). The shear yield stress and ultimate shear strength of all the alloys were reduce with the addition of Sn. The presence of the soft Sn reduces the volume fraction of the eutectic structure and the hard MgZn₂ and Mg₂Zn₁₁.

However, the wettability of Zn-Al system solder alloys is relatively poor due to the oxygen affinity of Zn. According to the report from N. Kang et al, the increase of Al content from 4.0 mass.% to 6.0 mass.% can improve the wettability and electrical resistivity of Zn-Al, and also the hardness and tensile strength ²⁶).

1.2.3.2 Zn-Sn

Zn-Sn system solder alloys do not exist the IMCs phase in the microstructure, in addition it has good mechanical properties and excellent electrical and thermal conductivity, it is considered a promising solder alloy of high-temperature lead-free solder alloy ⁵⁶). Zn-xSn alloys (x = 20 mass.%, 30 mass.% and 40 mass.%) were proposed by K. S. Kim et al^{44, 48, 49, 77}). The research indicated that the Zn-Sn system solder alloys are suitable for high temperature solder applications including the excellent electrical properties, oxidation resistance at high temperature, and the improved ductility compared with other Zn-based system solder alloys due to the microstructure with no IMCs ^{49,77}). Moreover, the stability during reflows, shear strength and the thermal conductivity were also observed in these research ⁴⁸). The results demonstrate that the shear strength of the Zn-Sn system solder alloys and Cu joint was 30-34 MPa, being higher than that of a Pb-5Sn solder (26.2 MPa). In addition, there was no significant change in the shear strength of the joint after multiple reflows up to 533 K. On the other hand, the thermal conductivities of Zn-Sn system solder alloys are 100-106 W·K⁻¹·m⁻¹, which are higher than both Au-20Sn (59.1 W·K⁻¹·m⁻¹) and Pb-5Sn (35.6 W·K⁻¹·m⁻¹) solder alloys.

R. Mahmudi et al studied the shearing strength of Zn-Sn system solder alloys at high temperature by shear punch testing ⁵⁶⁾. In the temperature range of 298-425 K, the shear strength decreased with the increasing Sn concentration due to soft Sn-rich matrix and hard Zn-rich particles contained in the microstructure of the alloys. This structure exhibits similar behavior to composite materials, and the volume fraction and strength of each phase controls the deformation resistance. It is also concluded by the authors that the yield stress of Zn-Sn system solder alloys at high temperatures should higher than Pb-5Sn solder alloy.

1.2.4 Bi-based solder alloys

Bi is a non-toxic heavy metal, and both the shear modulus (12 GPa) and melting point (544 K) are very close to Pb-5Sn solder alloy ⁷⁸⁾. Therefore, Bi-based solder alloys become promising alternatives for high-temperature lead-free solder.

Bi-Ag system solder alloys contain only a single invariant eutectic reaction at 97.5% Bi (mass. %). There are no IMCs phases and low solubility of silver in Bi solid-solution strengthening. The microstructure and properties of Bi-2.5/11Ag (mass.%) solder alloys for high-temperature applications were investigated by J. M. Song et al ⁴⁵⁾. The results show that Bi-Ag alloys exhibited a non-equilibrium solidification structural feature and a large undercooling ⁴⁴⁾. Pure Bi shows greater undercooling than Bi-Ag solder alloys. Primary Ag, Bi and the eutectic of Bi and Ag are existed in the microstructure. The addition of Ag content effectively increase the tensile strength of Bi-Ag solder alloys compared with pure Bi. Furthermore, Bi-11Ag solder alloy has higher fracture strain than pure Bi due to the resisted of crack growth by primary Ag. On the other hand, the cooling rate of the Bi-11Ag solder alloy was found that air cooled Bi-11Ag solder alloy showed higher elongation than quenched ones by M. Shimoda et al ⁵²⁾. J. E. Spinelli et al found that hardness is shown to be directly affected by both solute microsegregation and morphologies of the phases forming the Bi-Ag solder alloys ⁷⁹⁾. The interfacial morphology and tensile properties of the joints between Cu and Ni were also investigated by J. M. Song et al ⁸⁰⁾. At 623 K, Cu dissolved into liquid Bi-Ag as the composition of Cu-35at%Bi-5at% Ag without forming IMCs. In contrast,

Ni reacted with liquid Bi-Ag forming NiBi_3 of IMCs on the interface. The joint of Bi-Ag solder alloys and Cu shows a better tensile strength because of the brittle IMCs at the interface. M. Nahavandi et al tested the wetting angles of Bi-1.5, 2.5 and 3.5Ag solder alloy ⁸¹⁾. It is revealed that the wetting angle decreases with the increasing Ag content. And 11.17 degree wetting angle is shown for Bi-3.5Ag solder alloy, which means that it could easily spread on a Cu substrate.

The additions of Ge and Sb into Bi-Ag system alloys effect the properties of these solder alloys ^{82, 83, 84)}. J. N. Lalena et al add small amount of Ge into Bi-Ag solder alloy ⁸²⁾. With the small amount addition of Ge, the Bi-11Ag-0.5Ge solder alloy shows lower thermal conductivity and wettability, however, the lower shear modulus result in a high thermal fatigue resistance. The composition of Bi-2.6Ag-0.1Cu-xSb solder alloys were studied by B. Kim et al ⁸³⁾. The presence of Sb occurred Cu-Sb and Ag-Sb IMCs, and emerged lower wettability or higher hardness. H. Zhang et al compared the tensile properties of pure Bi, Bi-2.5Ag, and Bi-1.0Ag-0.3Sn-0.03Ge with Pb-2.5Ag-2.5Sn ⁸⁴⁾. The results reported that the addition of Sn and Ge formed finer microstructure with small grain size. The tensile strength and elongation of Bi-1.0Ag-0.3Sn-0.03Ge were lower than those of Pb-2.5Ag-2.5Sn at room temperature and the brittle fracture occurs in Bi phases.

1.3 Development of alloy design methods

It's a general method of material design adopted by most researchers to confirm material components with best performance through seeking rules by a large number of technological tests. Until now, almost all literatures on development of solder alloy introduce the experimental method that adopts "tentative" test. Although some tests adopt orthogonal test method to reduce tests amount, however, this "tentative" test is not only time-consuming and laborious, but also needs significant economic losses. This method will still take the essential aspect of solder alloys design methods for a long term.

The alloy design refers to that researching alloy with specific target performance, under guidance of theory, to confirm which alloy element needing to be added into base metal and its quantity, and to forecast the property. Based on scientific, efficient, economical and predictive requirements of science development to material design, it will be the certain trend to conduct material design through calculation method. Along with the condition that continuous development of metal materials on theory of microstructure, phase structure, atomic structure (or electronic structure), energy band theory, chemical bond theory, electronic theory and also the continuous development of computer technology, the material scientific design continues to mature, and moves toward practical stage gradually. The following contents will introduce variety methods on alloy design.

1.3.1 Semi-empirical mode material design calculation method

This is a method that predicts material structure and property based on existing experimental data. Since 1996, Japan Engineering Manufacturing Center (RACE) has been funded by Japan Science and Technology Association for a long term, and has established LPF (Linus Pauling File) database. This database covers structure, diffraction, composition, intrinsic properties and other information of alloys, intermetallic compounds, ceramics, minerals and so on⁸⁵⁾. At least 200,000 data items related to structure, diffraction, intrinsic properties, and 35 thousand data items recorded since 1900 are stored in this knowledge information system. Based on this

powerful material database with an accuracy beyond 95% to seek laws, in principle, prediction for material properties can be realized only by entering atomic number and considering of possible compound composition ⁸⁵). This method has not been applied in the field of solder alloy design

, but LPF researchers think that, based on LPF database, a knowledge-information system can be established by taking advantage of existing science principles, and new materials can be predicted and developed systematically by calculation.

1.3.2 Thermodynamic auxiliary solder design

Based on basic theory of thermodynamics, to establish a thermodynamic model can conduct solder alloy phase equilibrium calculation, optimize phase diagram and predict new alloy system. There are relevant researches aiming at binary, ternary and even quaternary solder alloys.

Beijing University of Science and Technology has determined the Ag-Sn binary phase model through Redlich-Kister polynomial and chemical metering composition model; conducted system optimization by adopting software developed by Lukas et al., and the calculated alloy phase diagram satisfies thermodynamic experimental data ⁸⁶). T. M. Korhonen, has conducted Sn-In-Ag phase equilibrium calculation through minimum Gibbs energy calculation according to second law of thermodynamics ⁸⁷). The Muggianu expression of three-phase structure thermodynamic model extending from binary to ternary is as bellow ⁸⁸):

$$G = \sum_{i=1}^3 x_i G_i^0 + RT \sum_{i=1}^3 x_i \ln(x_i) + \sum_{i=1}^2 \sum_{j=i+1}^3 x_i x_j \cdot \sum_{n=0}^2 L_{ij}^n (x_i - x_j)^n + x_1 x_2 x_3 L_{123}$$

where, G_i^0 is the Gibbs free energy of element i , n is phase state, x_i and x_j are the mole fraction of i and j , L_{ij}^n is the interaction energy of i and j in n phase, L_{123} is the three-component interaction energy. Through calculation, the solder alloy that can conduct reflow soldering within temperature range approaching to Pb-Sn eutectic temperature can be determined. The composition of the alloy is 3.5% Ag, 20% In, 76.5% Sn. The experiment has confirmed the correctness of calculation results.

The Sweden Royal Institute of Technology has developed Thermo-Cacl

thermochemical software, and S. W. Yoon et al. has applied it into phase equilibrium calculations for quaternary alloys. Firstly, based on phase equilibrium, select several alloy compositions that have eutectic temperature with Sn that is approaching to Pb-Sn eutectic temperature, then conduct Sn-Bi-In-Zn system lead-free solder alloy thermodynamic auxiliary synthesis design and performance evaluation⁸⁸). Comparing the result of DSC with thermodynamic calculated phase transitions and melting temperature values, both conclusions are consistent. Finally, determined to take Sn-Bi-5In-6An solder alloy as replacement of Pb-Sn solder alloy.

1.3.3 Molecular orbital theory calculation and design method

Molecular orbital theory refers to research electronic motion status based on quantum chemistry calculation. This method can design and predict the material structure and performance from the microscopics. The molecular orbital theory is based on non-relativistic approximation, Born-Oppenheimer approximation and orbital approximation, its basic concepts are: regard molecule as a whole; atomic orbitals corresponding to each atomic in molecule consist several molecule orbitals; then arrange atomics in a series of molecular orbits, and atomics belong to whole molecule. Among them, ab initio method and Discrete Variational (DV)- $X\alpha$ cluster method are adopted in the field of material design more frequently.

1.3.3.1 Ab initio molecular orbital method

The ab initio method is a quantum theory all-electronic calculation method that uses only Planck's constant, electron rest mass and electricity quantity three physical constants without any empirical parameters to solve the quantum electronic theory. This method is based on three approximations of molecular orbital theory. In principle, any suitable exact solution of approaching to self-constant field limit can be obtained as long as one suitable function is selected and the number of self-consistent iterations is sufficient. The ab initio method is rather better than semi-empirical method, can obtain the electronic motion status of various systems (ions, molecules, clusters and chemical reaction systems) and relevant microscopic information, and is able to explain or predict

reasonably atomic bonding, molecular structure, chemical reaction process, nature of material and related experimental observations. However, due to complexity of the calculation system, the calculated amount and occupied computer storage spaces of the ab initio method increase dramatically, and this puts forward new tasks for computer technology constantly. On the other hand, the error of the ab initio method is mainly from non-relativistic approximations and orbital approximations. At present, the configuration interaction method is mainly adopted to correct these errors, however, this method increases the demand for computer memory and machine hour obviously, so that this method is hard to realize for larger molecules. This method has already been widely used in the field of material research in Japan and the United States, but it has not been reported to be used in the field of solder alloys.

1.3.3.2 DV- $X\alpha$ cluster method

$X\alpha$ method was put forward firstly by Slater in 1951. This method takes electronic exchange function as statistical average value, and substitutes into Hartree-Fock function to achieve $X\alpha$ equation. DV- $X\alpha$ cluster method is based on Hartree-Fock-Slater approximation, and can provide rather accurate electronic structure even for larger size cluster system. In this method, the potential energy of Slater's local electronic exchange involves the interaction between electrons. V_{XC} is given by equation below:

$$V_{XC} = -3\alpha[3\rho(r)/8\pi]^{1/3}$$

where, $\rho(r)$ is the local electron density, the parameter α is fixed value 0.7. The calculation adopts self-consistent electronic approximation, and uses discrete sampling method to integrate matrix elements. Hamiltonian function matrix elements and overlapping integrals are calculated by the method of random sampling⁸⁶). The molecular orbital is consisted by linear combination of atomic orbit. Compared with the ab initio method, DV- $X\alpha$ cluster method doesn't have unique physical model, but only is an improvement in computational methods. Its accuracy is generally slightly lower than the ab initio method. But because it has adopted the localized density functional approximation of exchange potential, so that it doesn't need to calculate a large number

of multi-center integrals, and its calculated quantity is only 1/100 of the ab initio method. This method is one of the common methods of calculating heavy atom-containing molecules and solid atom clusters.

In 1984, M. Morinaga, et al. adopted DV-X α cluster method to research the electronic structure of elements of Fe, Ni and Ti system alloys, and obtained Fermi level parameters of 20 alloy elements, and put forward the d-electrons concept for evaluation of alloy phase stability and various properties⁹⁰). The two parameters, Bo and Md were used in this approach. In 1993, they also predicted the mechanical properties of Al system alloys through the same way, and established alloy design method by DV-X α cluster method⁸⁸). In this prediction, a new parameter Mk (s-orbital energy level of alloy element) was introduced to describe the properties of the alloys⁹¹). In 1994, R. Ninomiya proposed a quantitative method for predicting the mechanical properties of magnesium alloys based on electronic structure⁸⁹). The average value of Mk reflects mechanical properties of the alloy. Figure 1.1 is the relations of Mk average value ($\Delta \overline{Mk}$) and alloy hardness⁸⁹). Figure 1.2 is the relation of $\Delta \overline{Mk}$ and alloy tensile strength⁸⁹). This method is extremely convenient and effective in predicting mechanical properties of multi-component Mg alloys and design of high-performance Mg alloys.

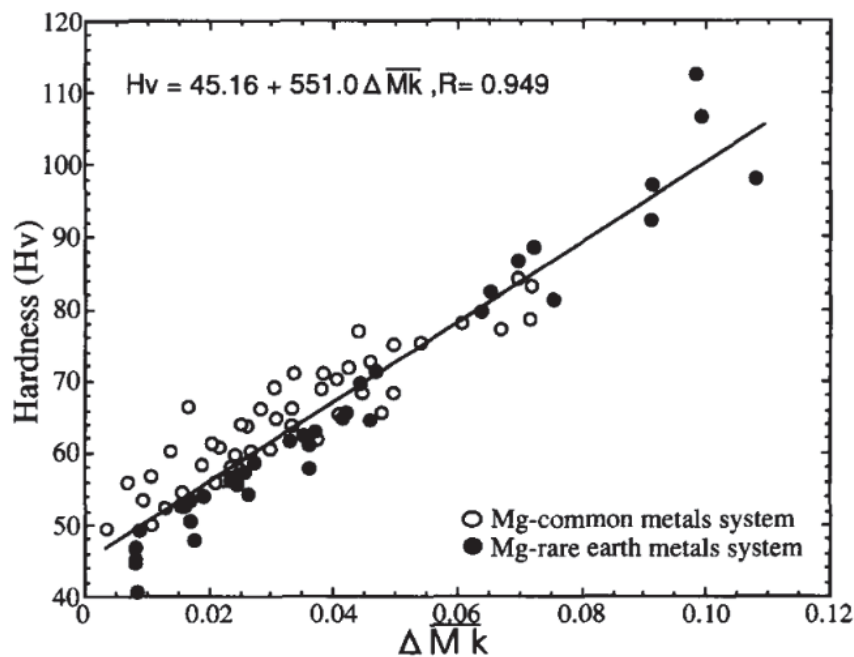


Fig. 1.1 Correlation of the Vickers hardness with $\Delta \overline{Mk}$ for magnesium alloys⁸⁹).

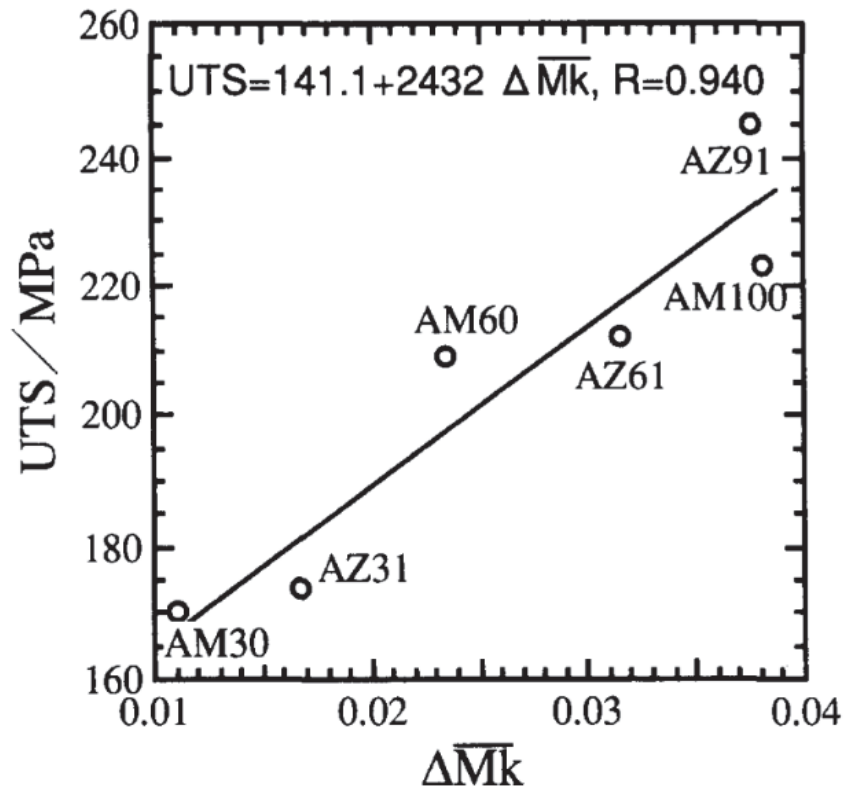


Fig. 1.2 Correlation of the tensile strength with $\Delta \overline{Mk}$ for magnesium alloys ⁸⁹).

1.4 Objectives of this study

With the rapid development of the electronics industry and the increasing attention to environmental issues, the research of high temperature lead-free solders is imminent. However, there is still no obvious cost-effective alternate for high-lead content high-temperature solders. Table 1.2 summarizes the key advantages and disadvantages of the alloys covered before. Au-based alloys have high strength and excellent creep resistance. However, the high cost of gold is the major problem of developing Au-based alloys as an alternative candidate to high-temperature solder. On the other hand, Zn-based system solder alloys show low cost and the microstructure with no IMCs, but the high corrosive of Zn and poor wettability limited the application. In the case of the similar melting temperature of pure Bi to traditional high-lead content high-temperature solder alloys and the affordable cost of Bi, Bi-based solder alloys is a very prospective high-temperature solder alloy.

Table 1.2 Advantages and disadvantages of solder alloys for high-temperature applications.

Alloys	Advantages	Disadvantages
Pb-Sn	Ideal melting temperature, good wettability, stable microstructure, excellent mechanical properties	Toxic
Au-Sn	Good creep resistance	Expensive, brittle Au-Sn IMCs
Au-Ge	Low elastic modulus, stable microstructure, relatively high strength	Expensive, difficult to manufacture
Zn-Al	Low cost, easy to manufacture, no IMCs formed under equilibrium	High corrosive, poor wettability
Zn-Sn	Low cost, no IMCs formed under equilibrium, ductility improved compared to Zn-Al	High corrosive, formation of liquid phase at 199 °C
Bi-Ag	Acceptable melting point, affordable cost	Low thermal conductivity

The main problem for Bi-based solder alloys is the mechanical properties and the low thermal conductivity. This is due to the brittle of Bi, and the low thermal conductivity of Bi ($\lambda = 8 \text{ W}\cdot\text{K}^{-1}\cdot\text{m}^{-1}$), which is much lower than high-lead content solders like Pb-5Sn ($\lambda = 35 \text{ W}\cdot\text{K}^{-1}\cdot\text{m}^{-1}$)⁸². Thus, some alloy elements is added in Bi to facilitate the mechanical properties and thermal conductivity. Table 1.3 shows the target values of high-temperature lead-free solder alloy.

Table 1.3 Target values of high-temperature lead-free solder alloys.

Properties	Target values	References
Ultimate tensile strength at RT (MPa)	>20	
Fracture strain at RT (%)	>5	
Fracture strain at high temperature (%)	>30	
Solidus temperature (K)	>533	85
Wetting angle (degree)	<90	
Thermal conductivity, ($\text{W}\cdot\text{K}^{-1}\cdot\text{m}^{-1}$)	>20	85

The method of material design based on theoretical calculation has the characteristics of saving time, high efficiency and economy, especially the prediction of material properties will make it become the main trend of material design. In this study, DV-X α cluster method is used to design the Bi-based high-temperature solder alloys by the parameter ΔMk , which is average value of s-orbital energy levels (Mk). The possibility for prediction of the mechanical properties at room and high temperatures by the parameter ΔMk were investigated.

References

- 1) F. W. Gayle, G. Becka, A. Syed, J. Badgett, G. Whitten, T. Y. Pan, A. Grusd, B. Bauer, R. Lathrop, J. Slattery: *JOM* **53** (2001) 17-21.
- 2) S. J. Kim, K. S. Kim, S. S. Kim, K. Sukanuma, G. Izuta: *Electron. Mater.* **38** (2009) 2668-2675.
- 3) S. J. Kim, K. S. Kim, S. S. Kim, C. Y. Kang, K. Sukanuma: *Mater. Trans.* **49** (2008) 1531-1536.
- 4) K. Sukanuma, S. J. Kim, K. S. Kim: *JOM* **61** (2009) 64-71.
- 5) V. Chidambaram, J. Hattel, J. Hald: *Microelectron. Eng.* **88** (2011) 981-989.
- 6) C. Wang, H. Chen, P. Li: *Mater. Chem. Phys.* **136** (2012) 325-333.
- 7) H. Jiang, R. Hermann, W. Plumbridge: *Mater. Sci.* **31** (1996) 6455-6461.
- 8) O. Nousiainen, J. Putaala, T. Kangasvieri, R. Rautioaho, J. Vahakangas: *Electron. Mater.* **35** (2006) 1857-1865.
- 9) H. Wang, X. Ma, F. Gao, Y. Qian: *Mater. Chem. Phys.* **99** (2006) 202-205.
- 10) K. S. Kim, C. H. Yu, N. H. Kim, N. K. Kim, H. J. Chang, E. G. Chang: *Microelectron. Reliab.* **43** (2003) 757-763.
- 11) H. Schoeller, S. Bansal, A. Knobloch, D. Shaddock, J. Cho: *Electron. Mater.* **38** (2009) 802-809.
- 12) C. Andersson, J. Liu: *Int. Fatigue.* **30** (2008) 917-930.
- 13) I. Ohnuma, X. J. Liu, H. Ohtani, K. Ishida: *Electron. Mater.* **28** (1999) 1164-1171.
- 14) Y. Shi, W. Fang, Z. Xia, Y. Lei, F. Guo, X. Li: *Mater. Sci* **21** (2010) 875-881.
- 15) X. J. Liu, I. Ohnuma, C. P. Wang, M. Jiang, R. Kainuma, K. Ishida, M. Ode, T. Koyama, H. Onodera, T. Suzuki: *Electron. Mater.* **32** (2003) 1265-1272.
- 16) X. J. Liu, K. Oikawa, I. Ohnuma, K. Ishida, R. Kainuma: *JOM* **55** (2003) 53-59.
- 17) B. Kim, C. W. Lee, D. Lee: *Alloy. Compd.* **592** (2014) 207-212.
- 18) X. J. Liu, M. Kinaka, Y. Takaku, I. Ohnuma, R. Kainuma, K. Ishida: *Electron. Mater.* **34** (2005) 670-679.
- 19) X. J. Liu, C. P. Wang, F. Gao, I. Ohnuma, K. Ishida: *Electron. Mater.* **36** (2007)

- 1429-1441.
- 20) X. J. Liu, F. Gao, C. P. Wang, K. Ishida: *Electron. Mater.* **37** (2008) 210-217.
 - 21) F. Gao, C. P. Wang, Y. Y. Li, X. J. Liu, Y. Takaku, I. Ohnuma, K. Ishida: *Electron. Mater.* **36** (2009) 2096-2105.
 - 22) J. H. Kim, S. W. Jeong, H. M. Lee: *Mater. Trans.* **43** (2002) 1873-1878.
 - 23) G. S. Matijasevic, C. C. Lee, C. Y. Wang: *Thin. Solid. Films.* **223** (1993) 276-287.
 - 24) C. Datian, W. Zhifa, W. Huabo, L. Jinwen: *Rare. Metal. Mat. Eng.* **37** (2008) 690-693.
 - 25) T. Takahashi, S. Komatsu, H. Nishikawa, T. Takenoto: *Electron. Mater.* **39** (2010) 1241-1247.
 - 26) N. Kang, H. S. Na, S. J. Kim, C. Y. Kang: *Alloy. Compd.* **467** (2009) 246-250.
 - 27) S. W. Chen, C. C. Chen, W. Gierlotka, A. R. Zi, P. Y. Chen, H. J. Wu: *Electron. Mater.* **37** (2008) 992-1002.
 - 28) D. G. Ivey: *Micron.* **29** (1998) 281-287.
 - 29) F. Yost, M. Karnowsky, W. Drotning, J. Gieske: *Metall. Mater. Trans. A* **21** (1990) 1885-1889.
 - 30) B. Djurfors, D. G. Ivey: *Mater. Sci. Eng. B* **90** (2002) 309-320.
 - 31) J. Doesburg, D. G. Ivey: *Mater. Sci. Eng. B* **78** (2000) 44-52.
 - 32) H. M. Chung, C. M. Chen, C. P. Lin, C. J. Chen: *Alloy. Compd.* **485** (2009) 219-224.
 - 33) J. Yoon, H. Chun, J. Koo, H. Lee, S. Jung: *Scripta. Mater.* **56** (2007) 661-664.
 - 34) J. Glazer: *Electron. Mater.* **23** (1994) 693-700.
 - 35) H. Song, J. Ahn, J. Morris: *Electron. Mater.* **30** (2001) 1083-1087.
 - 36) Y. H. Zhu: *Mater. Process. Technol.* **73** (1998) 18-24.
 - 37) M. Furukawa, Y. Ma, Z. Horita, M. Nemoto, R. Z. Valiev, T. G. Langdon: *Mater. Sci. Eng. A* **241** (1998) 122-128.
 - 38) C. C. Chang, Y. W. Wang, Y. S. Lai, C. R. Kao: *Electron. Mater.* **39** (2010) 1289-1294.
 - 39) J. W. Yoon, B. I. Noh, S. B. Jung: *Mater. Sci. Mater. EI* **22** (2011) 84-90.
 - 40) J. M. Koo, J. W. Yoon, S. B. Jung: *Mater. Res.* **23** (2008) 1631-1641.

- 41) C. P. Lin, C. M. Chen, Y. W. Yen, H. J. Wu, S. W. Chen: *Alloy. Compd.* **509** (2011) 3509-3514.
- 42) S. W. Chen, A. R. Zi, P. Y. Chen, H. J. Wu, Y. K. Chen, C. H. Wang: *Mater. Chem. Phys.* **111** (2008) 17-19.
- 43) D. Frear, P. Vianco: *Metal. Mater. Trans. A* **25** (1994) 1509-1523.
- 44) S. Kim, K. S. Kim, K. Suganuma, G. Izuta: *Electron. Mater.* **38** (2009) 873-883.
- 45) J. M. Song, H. Y. Chuang, Z. M. Wu: *Metall. Mater. Trans. A* **38** (2007) 1371-1375.
- 46) Y. Takaku, K. Makino, K. Watanabe, I. Ohnuma, R. Kainuma, Y. Yamada: *Electron. Mater.* **38** (2009) 54-60.
- 47) Y. Takaku, L. Felicia, I. Ohnuma, R. Kainuma, K. Ishida: *Electron. Mater.* **37** (2008) 314-323.
- 48) S. Kim, K. S. Kim, S. S. Kim, K. Suganuma: *Electron. Mater.* **38** (2009) 266-272.
- 49) J. E. Lee, K. S. Kim, K. Suganuma, J. Takenaka, K. Hagio: *Mater. Trans.* **46** (2005) 2413-2418.
- 50) H. Solomon: *Electron. Mater.* **19** (1990) 929-936.
- 51) T. Zhou, B. Tom, O. Martin, S. H. Jia: *Ins. Electron. Pack.* **8** (2005) 6-7.
- 52) M. Shimoda, T. Yamakawa, K. Shiokawa, H. Nishikawa, T. Takenoto: *Trans. JWRI* **41** (2012) 51-54.
- 53) A. R. Geranmayeh, R. Mahmudi, M. Kangoie: *Mater. Sci. Eng. A* **528** (2011) 3967-3972.
- 54) J. W. Yoon, H. S. Chun, B. I. Noh, J. M. Koo, J. W. Kim, H. J. Lee: *Microelectron. Reliab.* **48** (2008) 1857-1863.
- 55) R. Chromik, D. Wang, A. Shugar, L. Limata, M. Notis, R. Vinci: *Mater. Res.* **20** (2005) 2161-2172.
- 56) R. Mahmudi, M. Eslami: *Mater. Sci. Mater. Electron.* **1** (2010) 1-5.
- 57) W. Shengmin, L. A. Keer, S. Vaynman, L. R. Lawson: *Compon. Pack. Technol. IEEE Trans.* **25** (2002) 23-31.
- 58) R. Chang, F. McCluskey: *Electron. Mater.* **38** (2009) 1855-1859.
- 59) K. Shinohara, Q. Yu: *Int. Fatigue.* **33** (2011) 1221-1234.

- 60) H. Jiang, R. Hermann, W. J. Plumbridge: *Mater. Sci.* **31** (1996) 6455-6461.
- 61) J. W. Nah, K. W. Paik, J. O. Suh, K. N. Tu: *Appl. Phys.* **94** (2003) 7560-7566.
- 62) Y. C. Liu, J. W. R. Teo, S. K. Tung, K. H. Lam: *Alloy. Compd.* **448** (2008) 340-343.
- 63) K. A. Lee, Y. M. Jin, Y. Sohn, J. Namkung, M. C. Kim: *Met. Mater. Int.* **17** (2011) 7-14.
- 64) A. R. Geranmayeh, R. Mahmudi: *Mater. Sci.* **40** (2005) 3361-3366.
- 65) C. Chang, Y. Lin, Y. Lai, C. Kao: *Electron. Mater.* **38** (2009) 2234-2241.
- 66) M. H. Tsai, W. M. Chen, M. Y. Tsai, C. R. Kao: *Alloy. Compd.* **504** (2010) 341-344.
- 67) C. C. Chang, H. Y. Chung, Y. S. Lai, C. R. Kao: *Electron. Mater.* **39** (2010) 2662-2668.
- 68) M. H. Tsai, Y. W. Lin, H. Y. Chuang, C. R. Kao: *Mater. Res.* **24** (2009) 3407-3411.
- 69) J. W. Jang, L. N. Ramanathan, J. K. Lin, D. R. Frear: *Appl. Phys.* **95** (2004) 8286-8289.
- 70) H. Schoeller, S. Bansal, A. Knobloch, D. Shaddock, J. Cho: *Mater. Sci. Eng. A* **528** (2011) 1063-1070.
- 71) J. Y. Tsai, C. W. Chang, Y. C. Shieh, Y. C. Hu, C. R. Kao: *Electron. Mater.* **34** (2005) 182.
- 72) G. S. Zhang, H. Y. Jing, L. Y. Xu, J. Wei, Y. D. Han: *Alloy. Compd.* **476** (2009) 138-141.
- 73) V. Chidambaram, J. Hald, J. Hattel: *Alloy. Compd.* **490** (2010) 170-179.
- 74) F. Cay, C. Kurnaz: *Mater. Des.* **26** (2005) 479-485.
- 75) T. Shimizu, H. Ishikawa, I. Ohnuma, K. Ishida: *Electron. Mater.* **28** (1999) 1172-1175.
- 76) R. Mahmudi, D. Farasheh: *Microelectron. Reliab.* **54** (2014) 1592-1597.
- 77) J. E. Lee, S. K. Kim, K. Suganuma, M. Inoue, G. Izuta: *Mater. Trans.* **48** (2007) 584-593.
- 78) T. Hehenkmap, R. Kossak: *Z. Metall.* **74** (1983) 195-198.
- 79) J. E. Spinelli, B. L. Silva, N. Cheung, A. Garcia: *Mater. Char.* **96** (2014) 115-

- 125.
- 80) J. M. Song, H. Y. Chuang, Z. M. Wu: *Electron. Mater.* **35** (2006) 1041-1049.
- 81) M. Nahavandi, M. A. A. Hanim, Z. N. Ismarrubie, A. Hajalilou, R. Rohaizuan, M. Z. S. Fadali: *Electron. Mater.* **43** (2014) 579-585.
- 82) J. N. Lalena, N. F. Dean, M. W. Weiser: *Electron. Mater.* **31** (2002) 1244-1249.
- 83) B. Kim, C. Lee, D. Lee, N. Kang: *Alloys. Compd.* **592** (2014) 207-212.
- 84) H. Zhang, S. Ikuo, S. Masayoshi, W. Hirohiko: *Mater. Trans.* **57** (2016) 873-880.
- 85) P. Villars, N. Onodera, S. Iwata: *Alloys. Compd.* **279** (1998) 1-7.
- 86) Y. Xie, Z. Qiao: *Phase. Equilibria.* **17** (1996) 208-250.
- 87) T. M. Korhonen, J. K. Kivilahti: *Electron. Mater.* **27** (1998) 149-158.
- 88) S. W. Yoon, J. R. Son, H. M. Lee: *Actamater.* **45** (1997) 951-960.
- 89) R. Nomiya, H. Yukawa, M. Morinaga: *Alloys. Compd.* **215** (1994) 215-232.
- 90) M. Morinaga, S. Nasu, H. A. Jsaïto: *Phys. Condes. Matter.* **3** (1991) 6817-6828.
- 91) M. Morinaga, S. Kamado: *Model. Simul. Mater. Sci. Eng.* **1** (1993) 151-164.

Chapter 2

The relation between electronic parameter and mechanical properties for Bi alloys

2.1	Introduction.....	28
2.2	Composition of alloys	30
2.2.1	Electronic parameter representing alloying effects	30
2.2.2	Selection of experimentally alloys	33
2.3	Experimental procedure.....	34
2.3.1	Materials and manufacturing process	36
2.3.2	Evaluation of some properties	38
2.4	Results and discussion	38
2.4.1	Microstructures	40
2.4.2	Characteristics on binary Bi-Cu/Ag/Zn alloys at 293 K.....	40
2.4.2.1	Tensile properties at 293 K.....	40
2.4.2.2	ΔM_k parameter and mechanical properties.....	45
2.4.3	Tensile properties on binary Bi-Cu/Ag/Zn alloys at 423 K.....	48
2.5	Summary	54
	References.....	55

2.1 Introduction

In late years, elimination of lead was promoted in industrial fields, according to RoHS (EU Directive on the Restriction of the use of certain Hazardous Substances in electrical and electronic equipment) order and the ELV (End of Life Vehicles) threshold of EU¹⁾. Therefore, the development of lead-free solders was carried out actively in the world. However, the development of lead-free solders for high temperature applications has not yet advanced^{2, 3)}. Many research groups paid the attention to the Au–Sn, Zn–Sn and Bi–Ag system alloys as a candidate of lead-free alloys, in the viewpoint of heat, electricity and melting point properties⁴⁻¹⁰⁾. However, Au system alloys were restricted in the application of high temperature solders because of high cost of Au. The application of Zn system alloys was also limited because of oxidability of Zn. On the other hand, the melting point of Bi was 544 K, which was similar with the conventional Pb–Sn alloys. Moreover, Bi possessed not only cheap cost but also no harm to human bodies and environment. Bi system alloys were one of candidate of lead-free alloys for high-temperature solders with great promise^{11, 12)}.

So far, the development of alloys with high performance had been performed relying on many trial-and error experiments and a few empirical rules. In order to develop new alloys more efficiently, a theoretical approach was strongly needed for the alloys design. The d-electrons concept on the basis of the theoretical calculation of electronic structures of alloys had been proposed on the basis of the Discrete Variational (DV)- $X\alpha$ ¹³⁻¹⁵⁾ cluster calculation, by Morinaga et.al^{16, 17)}. This concept was devised at first for austenitic Ni, Co and Fe alloys, and phase boundary or some physical and chemical properties were predicted by electronic parameters. The two parameters, Bo and Md, were used in this approach. The Bo which was the bond order showed the overlapping of electron clouds between atoms. Therefore, it was a measure of the covalent bond strength between atoms. The covalency increased with increasing Bo. The value of Md was related to the charge transfer, and hence to the electronegativity of elements. The Md was also found to be associated with the atomic radius. Both the electronegativity and the atomic radius were classical parameters which have been used in describing the nature of the chemical bond between atoms in solids.

The concept of alloys design had spread over the world since 1964 when PHACOMP (Phase Computation) had been proposed¹⁸⁾. This was a prediction method for the appearance of the undesirable brittle phases in the face-centered cubic (fcc) matrix. The parameter used for this prediction is electron vacancy number (N_v) that was the number of vacancies or electron holes existing above the Fermi level in the metal d-band proposed by Pauling¹⁹⁾. The solid solubility problem of alloys had been treated by the classical parameters of electronegativity and the atomic radius. The solid solubilities in transition-metal based fcc alloys could be treated quantitatively using the Md parameter, compared with the prediction by N_v ²⁰⁾. Therefore, Md-PHACOMP had been to be superior to the current N_v -PHACOMP²⁰⁾. Ti alloys were classified into the α , $\alpha+\beta$ and β types according to the phases existing in alloys. Compositions of forty commercial alloys were plotted on the Bo and Md coordinates. These three types of alloys were clearly separated in the Bo and Md map¹⁷⁾. Moreover, the compositional optimization of Al²¹⁾ system alloys as a simple metal were carried out by using s-orbital energy level (Mk)¹³⁻¹⁵⁾. The interaction between the dislocation density (or hindrance for dislocation migration) and ΔMk were investigated in the previous report²¹⁾. It was concluded that the ΔMk could be used as the indication of solid solution hardening level for ternary Al-1.5Mn-xMg alloys.

In this study, DV-X α cluster method was also used to obtain the s-orbital energy levels (Mk) of some alloying elements in a Bi cluster. In contrast, the tensile properties were measured using binary Bi-Cu/-Ag/-Zn alloys with a eutectic system. Their tensile and hardness properties were tried to arrange by this electronic parameter, as well as Ni, Al, Ti alloys. Further, the possibility for the prediction of the mechanical properties by this parameter was explored, as case study of Bi alloy design for the high temperature application.

2.2 Composition of alloys

2.2.1 Electronic parameter representing alloying effects

The Mk parameter was calculated in the cluster (MBi_7) presenting by an octahedron as a model of triclinic Bi. This cluster was shown in Fig. 2.1, and contained an alloying element M and its surrounding Bi atoms. Therefore, the alloying effects were inevitably involved in this Mk parameter. The values of Mk for alloying elements were listed in Table 2.1. Furthermore, as shown in Figs. 2.2 and 2.3, it was associated with the electronegativity and the atomic radius of elements: namely, the Mk level decreased with increasing electronegativity of pure metals, whereas it increased with increasing the atomic radius, even though there were some differences in the correlations between transition metals and non-transition metals, which agreed with the relation obtained from the MAI_{18} cluster as a model of fcc Al²²⁾. As explained in reference²³⁾, it was well known that the energy level obtained by the $X\alpha$ calculation represented the electronegativity itself²⁴⁾. In addition, the p-orbital energy level may be employed instead of the s-orbital energy level, but the spherical symmetrical s-orbital was probably better for the estimation of the mechanical properties of alloys, compared with the directional p-orbital²⁵⁾.

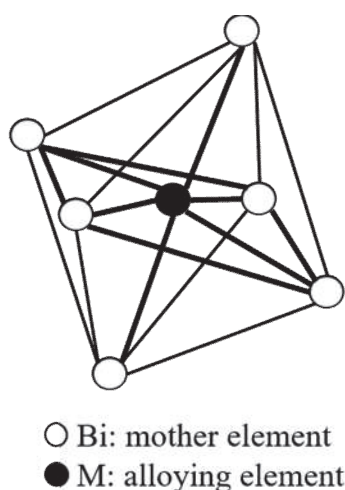


Fig. 2.1 A cluster model used for the calculation.

Table 2.1 The list of Mk of additional elements in a Bi cluster.

Elements	Mk (eV)	Elements	Mk (eV)
Bi	0.92	Ge	-8.56
Ag	4.63	Ti	6.10
Cu	3.47	Ca	6.25
Sn	4.54	Fe	4.20
Mo	5.43	Ni	3.88
Mn	4.48	B	0.65
Zn	2.40	Si	1.09
In	-4.11	K	9.17
Zr	6.24	Mg	4.06
Ga	1.27	V	5.03
Co	4.00	Sc	6.01
Cr	4.48	Li	6.50
Al	1.98	Be	2.46
Na	6.78	Nb	5.69

Employing Mk parameters, the ΔMk in the case of Bi alloys was defined using compositional average, as follow expression (2-1).

$$\Delta Mk = \sum X_M | Mk_M - Mk_{Bi} | \quad (2-1)$$

where, X_M was the molar fraction of alloy element M, Mk_M was the Mk of alloy element M, and Mk_{Bi} was the Mk of mother metal Bi.

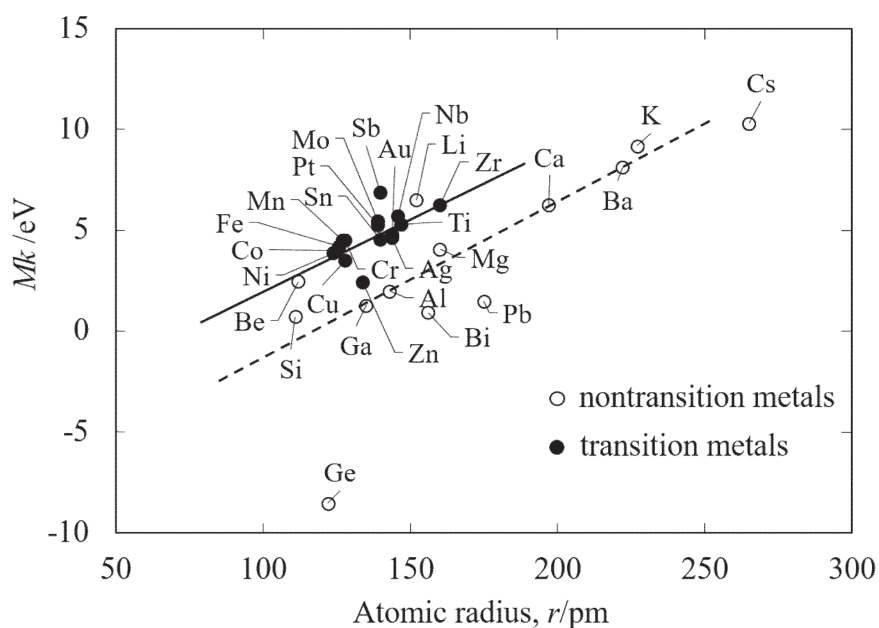


Fig. 2.2 Relation between the atomic radius and Mk of transition metals or nontransition metals added in a Bi cluster model.

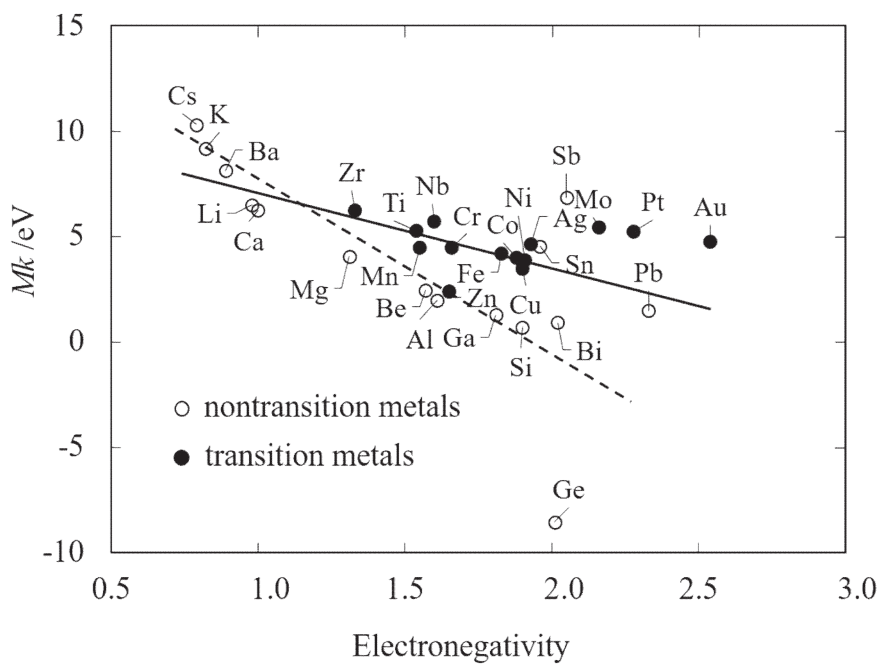


Fig. 2.3 Relation between the electronegativity and Mk of transition metals or nontransition metals added in a Bi cluster model.

2.2.2 Selection of experimentally alloys

The eutectic compositions of Bi-0.15mass.%Cu, Bi-2.5mass.%Ag and Bi-3.7mass.%Zn binary alloys were chosen because of both the low melting temperature and a little amount of ductility by the fine crystallized phases caused in a eutectic reaction. In contrast, pure Cu and Ag with fcc have many slip systems, and Zn was one candidate as high temperature solders. These eutectics exist near to pure Bi at temperatures about 1~16 K below the melting point of Bi, which suggests a little amount reduction in melting points even by the addition of ternary alloying elements in their alloy systems. Further, the alloy compositions near eutectic compositions were also chosen in this study, as listed in Table 2.2. The values of ΔMk were also listed in this table.

Table 2.2 The nominal composition, ΔMk and mean grain size of binary Bi system alloys.

Alloys (mass.%)	Alloys (mol%)	ΔMk	Mean grain size (μm)
Bi-0.15Cu	Bi-0.5Cu	0.013	42
Bi-0.25Cu	Bi-0.8Cu	0.021	42
Bi-0.5Cu	Bi-1.6Cu	0.042	43
Bi-0.75Cu	Bi-2.4Cu	0.062	41
Bi-1.0Cu	Bi-3.2Cu	0.082	37
Bi-2.5Ag	Bi-4.7Ag	0.176	--
Bi-5.0Ag	Bi-9.2Ag	0.343	40
Bi-1.8Zn	Bi-5.6Zn	0.082	40
Bi-3.7Zn	Bi-11.0Zn	0.163	41

2.3 Experimental procedure

2.3.1 Materials and manufacturing process

Bi alloys were cast by gravity casting. Figure 2.4 shows the illustration of the melt equipment. The stick Bi (99.99% of purity), the granular Ag (99.99% of purity), the laminar Cu (99.99% of purity) and the granular Zn (99.99% of purity) were put into the graphite crucible, and it was set in the electric furnace in air. Bi had the 2-3mm diameter and the others had the 1mm thickness. The molten metal was mixed by a ceramic stick at 773 K, and held at this temperature for 1.8 ks, after the melt down of all raw materials. And then the molten metal was poured into the casting mold which was heated to 773 K. The shape of the mold was shown in Fig. 2.5. As shown in Fig. 2.6, the mold was placed on a firebrick and air-cooled to 293 K by placing firebrick on the mold to eliminate variations in the temperature gradient of the molten metal and aimed at reduction of solidification defects.

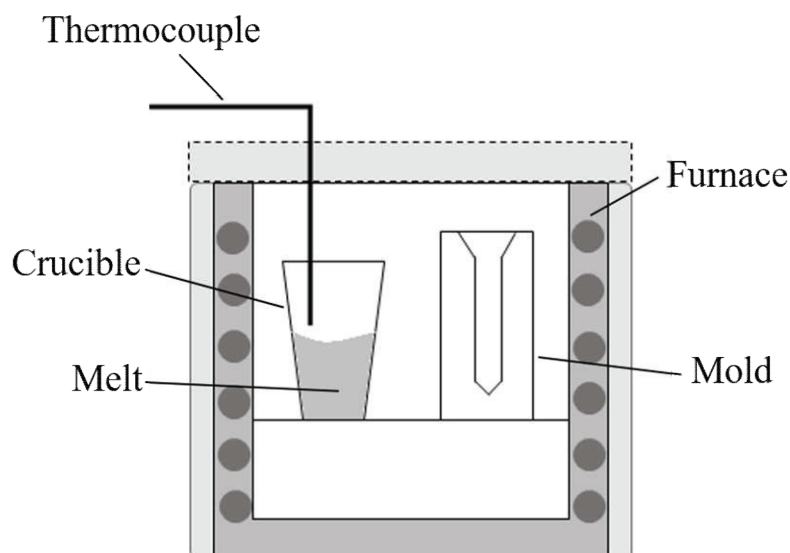


Fig. 2.4 Schematic illustration of the melt equipment.

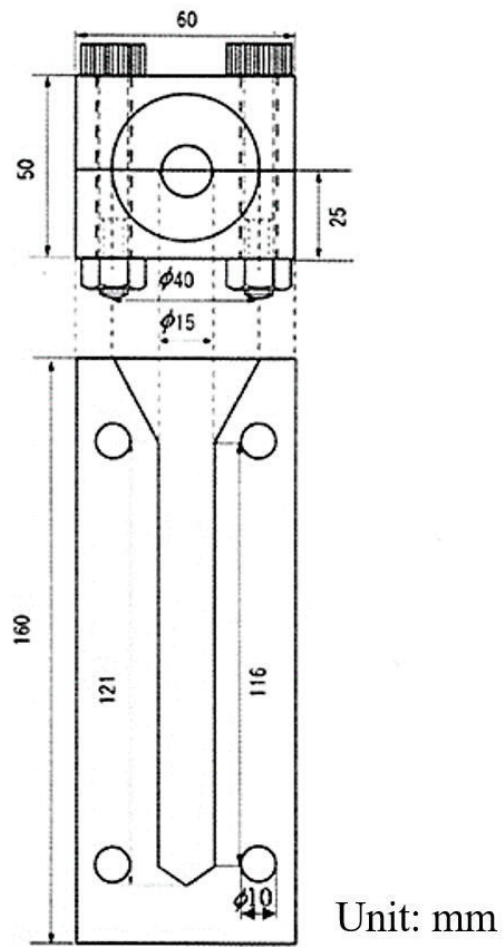


Fig. 2.5 Schematic diagram of mold made of SK5.

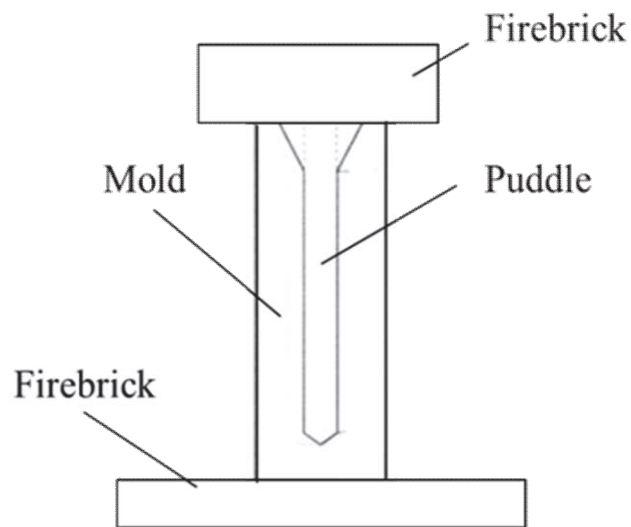


Fig. 2.6 Schematic diagram of mold when air-cooling.

2.3.2 Evaluation of some properties

Microstructural observation of these alloys using as-cast samples by the SEM and quantitative analyses of elements were conducted by the electron probe micro-analyzer (EPMA; JEOL JXA-8200, Japan). The hardness of the as-cast alloys were measured by a Rockwell hardness tester (B scale) at 293 K in air. The values reported for Rockwell on B scale hardness represented the average of seven separate measurements. Tensile tests of the experimental alloys were performed at 293 K and 423 K in air by using a mechanical testing machine (Autograph DCS-R-5000, Shimadzu Corporation, Japan) at the initial strain rate of $3.4 \times 10^{-4} \text{ s}^{-1}$. The dimensions of the gauge section of the tensile test specimen were 6 mm diameter \times 20 mm length, as shown in Fig. 2.7. An infrared furnace was used to raise the test temperature for tensile test at 423 K. Figure 2.8 shows the appearance of the infrared furnace. The infrared furnace is a radiant heating furnace using an infrared lamp of high energy density as a heat source. Reflecting infrared rays on the gold-coated water-cooled aluminum reflecting surface realizes high temperature zone with high precision for a short time. In addition, the SEM was used to examine the fracture surfaces of the tensile samples.

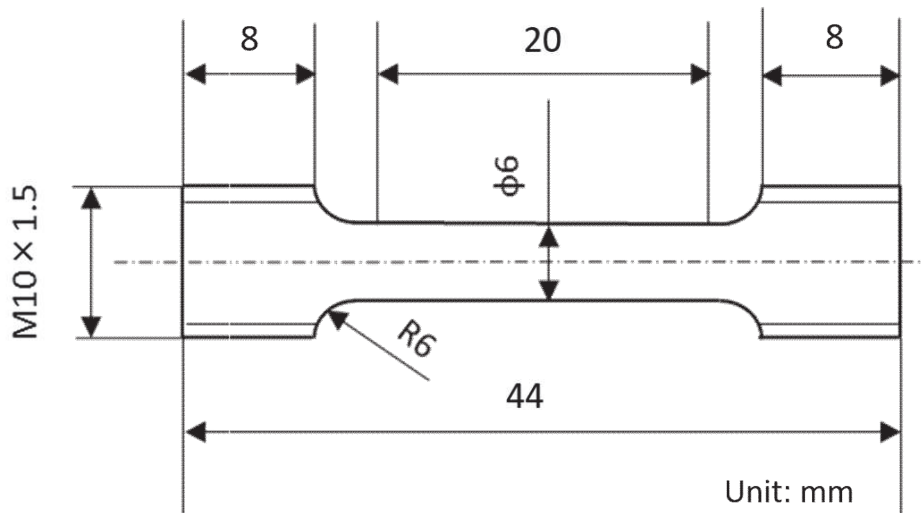


Fig. 2.7 Schematic diagram of tensile specimens.

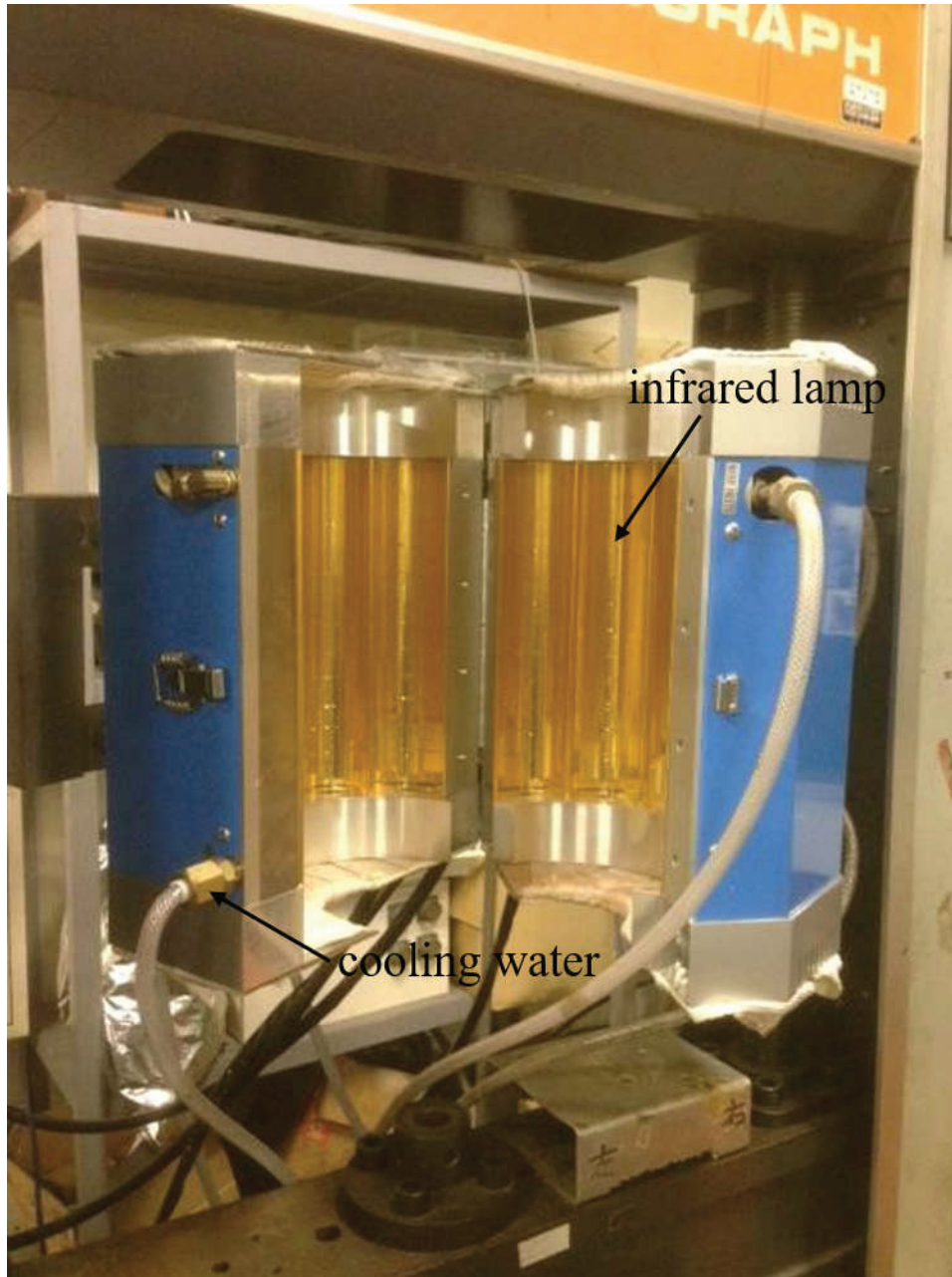


Fig. 2.8 Schematic diagram of infrared furnace.

2.4 Results and discussion

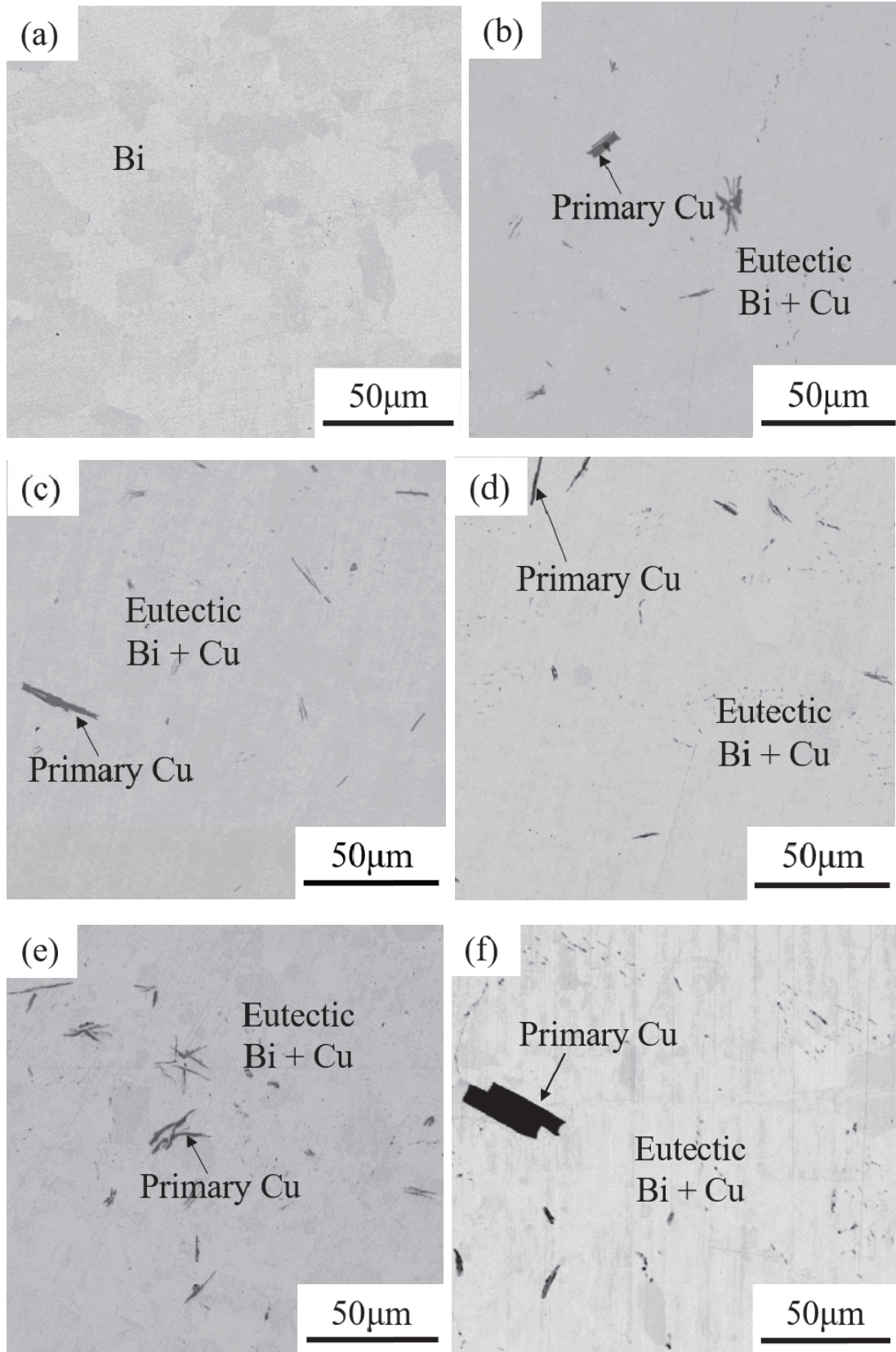
2.4.1 Microstructures

The microstructures of as-cast alloys with binary elements of Cu, Ag and Zn were shown in Fig. 2.9. Pure Bi is a monophasic Bi and consists of equiaxial grains with a size of 45 μm . A primary Cu phase and a eutectic consisting of Bi and Cu are observed in the case of the Bi-0.15–1.0Cu alloys. The amount and size of primary Cu in Bi-1.0Cu were much larger than those of Bi-0.5Cu, which led to the lower value in fracture strain, as mentioned in the term of 2.4.2.1.

Primary Ag solid solution (hereafter called Ag S.S.) and eutectic of Bi and Ag S.S. were observed in Bi-5.0Ag. In contrast, the eutectic of Bi and Ag S.S. were just observed in Bi-2.5Ag. Primary Zn and eutectic of Bi S.S. and Zn were observed in Bi-3.7Zn. In contrast, primary Bi S.S. with the dendritic shape and eutectic of Bi S.S. and Zn were observed in Bi-1.8Zn. The primary phases with plate and rod like shape were crystallized in Bi-1.0Cu, -5.0Ag and -3.7Zn alloys, which resulted in lower values in the fracture strains, as mentioned in the term of 2.4.2.1.

For their experimental alloys, the grain size of matrix was measured by the linear intercept method. The mean grain sizes were listed in Table 2, their values were 37 to 43 μm , showing the almost same level due to the usage of the same solidification condition. The microstructure of the Bi-2.5Ag alloy showed a typical Bi-Ag eutectic structure with the Bi and Ag solid solution formed alternately in normal eutectic cells with the size of 200 μm , as seen in Fig. 2.9 (g). The distance of their interphases was approximately 4.5 μm in the eutectic cells. In contrast, pure Bi showed the grain size of 45 μm .

For the quantitative analyses of alloying elements, the EPMA method was simply employed for convenience. Bi-1.0Cu and Bi-1.8Zn in nominal compositions were measured as Bi-1.0Cu and Bi-1.7Zn, respectively. Therefore, nominal compositions were almost same to chemical ones, and used for the alloy-description in this study.



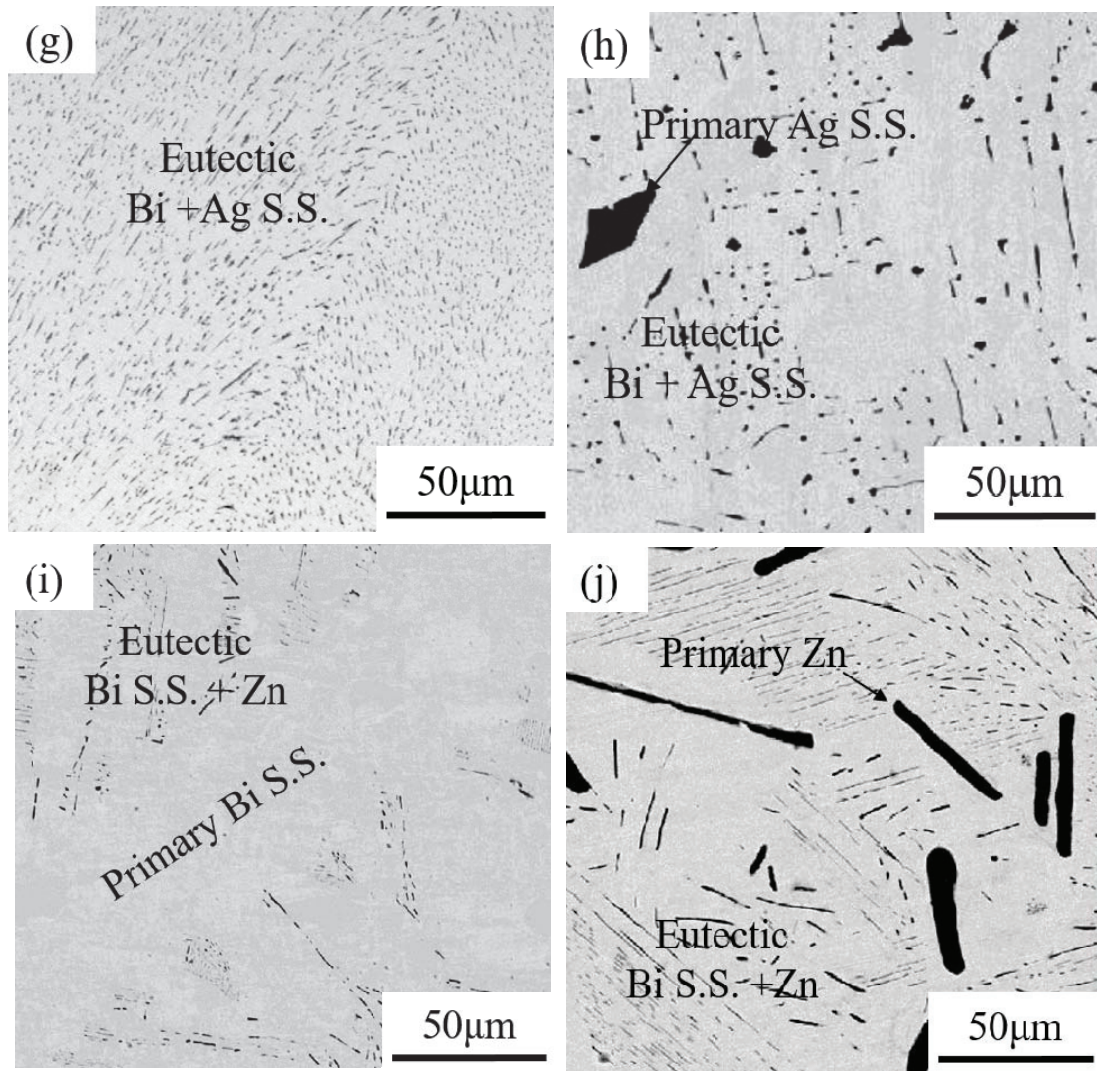


Fig. 2.9 Compositional images of (a) pure Bi, (b) Bi-0.15Cu, (c) Bi-0.25Cu, (d) Bi-0.5Cu, (e) Bi-0.75Cu, (f) Bi-1.0Cu, (g) Bi-2.5Ag, (h) Bi-5.0Ag, (i) Bi-1.8Zn and (j) Bi-3.7Zn alloys.

2.4.2 Characteristics on binary Bi-Cu/Ag/Zn alloys at 293 K

2.4.2.1 Tensile properties at 293 K

Figures 2.10 and 2.11 showed the nominal stress-strain curves of 9 binary Bi-M alloys and pure Bi as a reference, obtained from tensile tests at 293 K. The behavior in the stress-strain curves were changed depending on the kinds and amount of their

alloying elements. As shown in Fig. 2.10, the pure Bi showed a little amount of plastic deformation after elastic deformation, and values of the ultimate tensile strength or fracture stress, and fracture strain were 12 MPa and 0.7%, respectively. Moreover, the values in the ultimate tensile strength of Bi-0.15/1.0Cu, Bi-2.5/5.0Ag and Bi-3.7Zn alloys were 1.1 to 2.5-times larger than that of pure Bi, in 5 alloys showing the low fracture strain less than 4.6%. In contrast, the values in the ultimate tensile strength of Bi-0.25/0.5/0.75Cu and Bi-1.8Zn alloys were 1.2 to 1.4-times larger than that of pure Bi, in 4 alloys showing the larger values more than 9-33% in fracture strain, as shown in Fig. 2.11 indicating the full curves of stress and strain to fracture. The reduction of area was also indicated in this figure. The pure Bi showed lowest value in the reduction of area, which corresponded to the fracture strain of 0.7%. In contrast, the heterogeneity plastic deformation in three dimensions was observed showing the reduction of area of 4.3-40.7 %, in the Bi-0.5Cu alloy with the highest fracture strain of 33%.

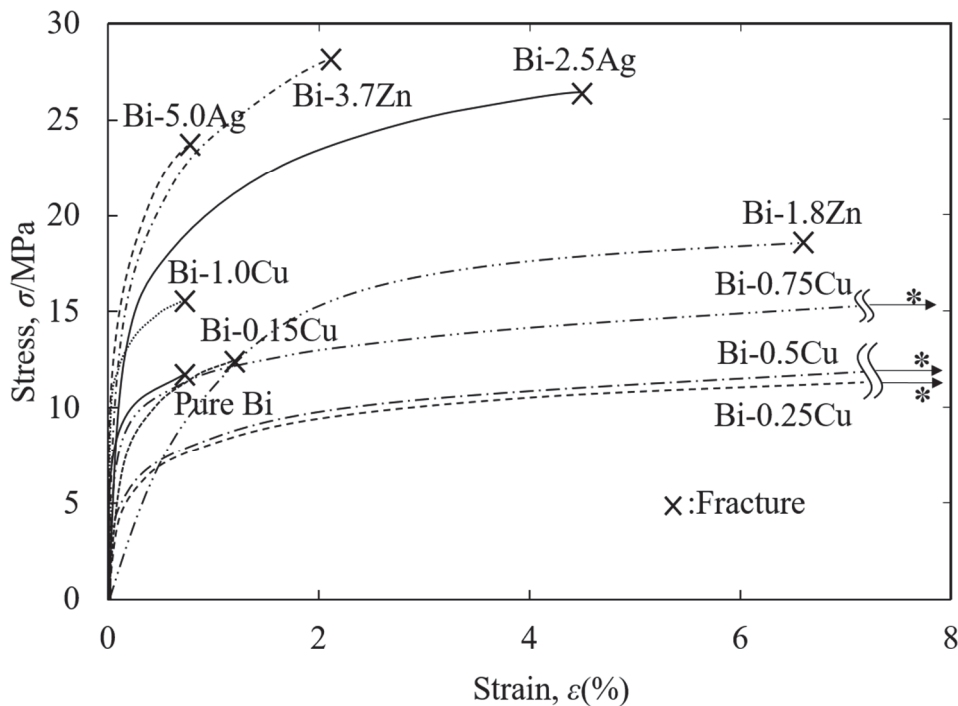


Fig. 2.10 Stress-strain curves of Bi-0.15Cu, Bi-0.25Cu, Bi-0.5Cu, Bi-0.75Cu, Bi-1.0Cu, Bi-2.5Ag, Bi-5.0Ag, Bi-1.8Zn, Bi-3.7Zn and pure Bi at 293 K. * Full stress-strain curves are indicated in Fig. 2.11.

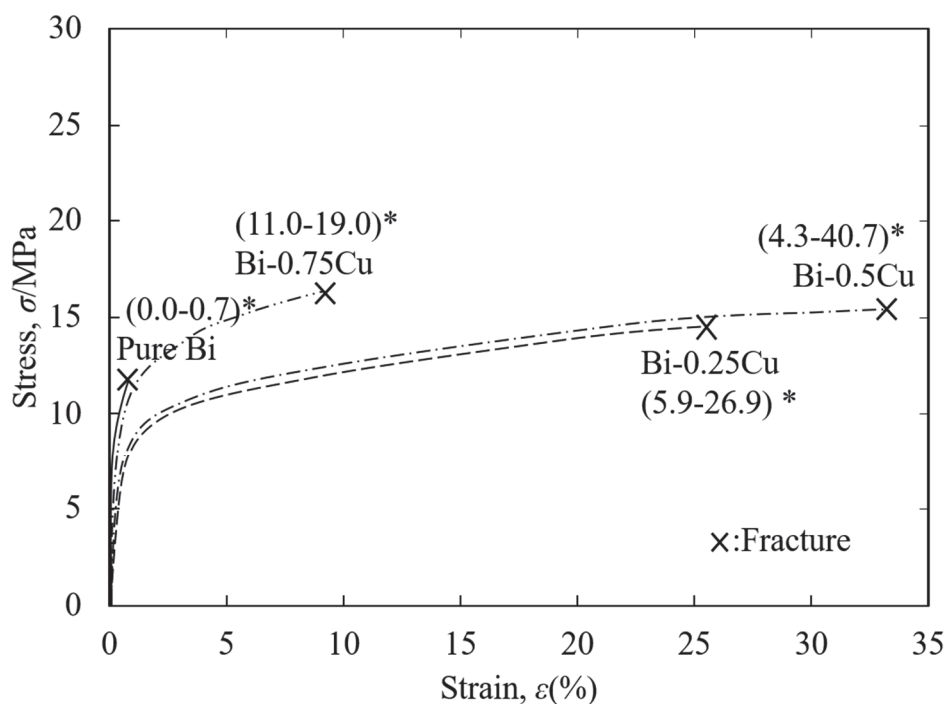
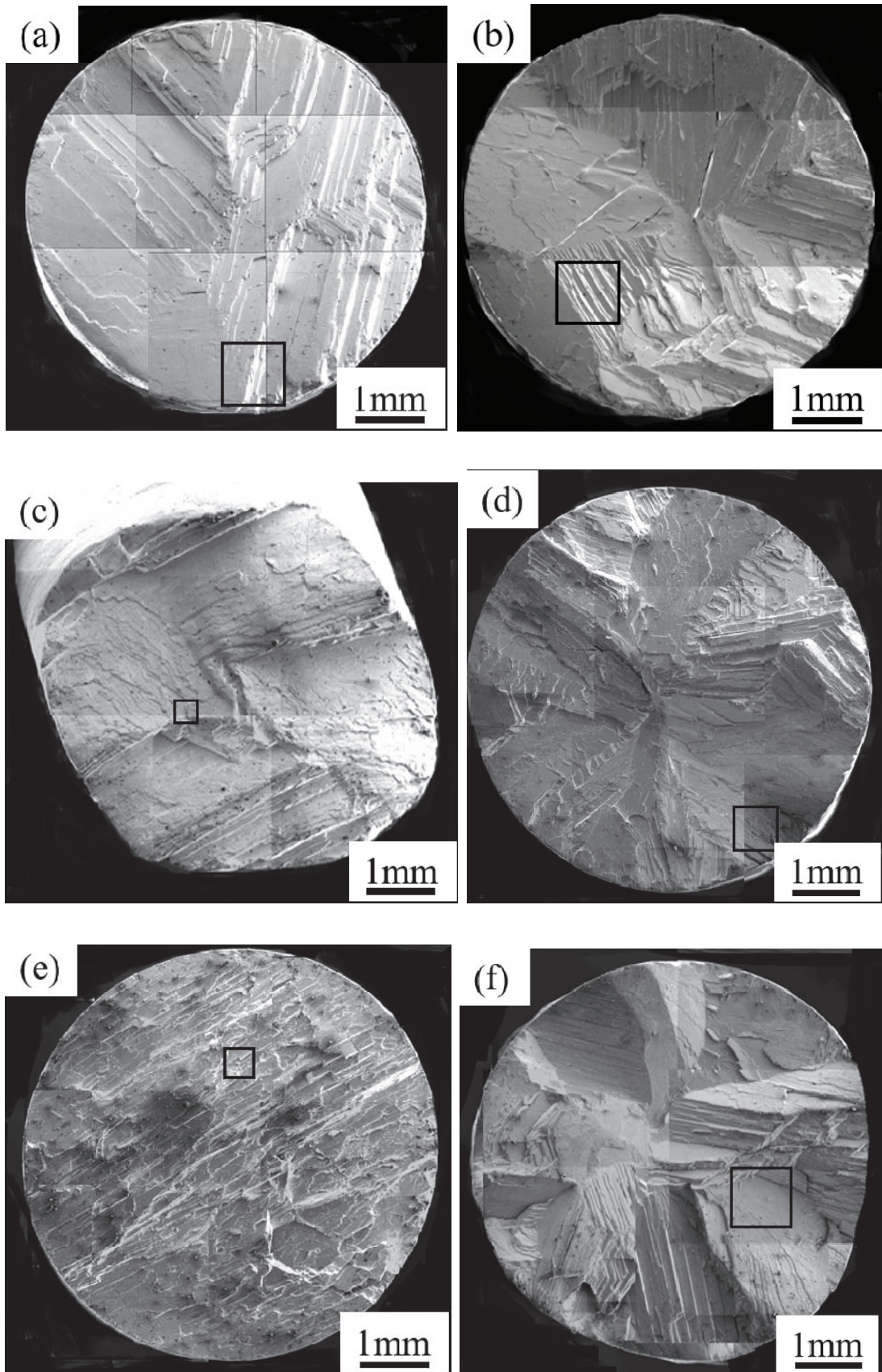


Fig. 2.11 Stress-strain curves of Bi-0.25Cu, Bi-0.5Cu, Bi-0.75Cu alloys and pure Bi at 293 K. * Range of reduction in area (%) after failure.

Some fracture surfaces after tensile tests were shown in Fig. 2.12, as typical examples. The pure Bi, Bi-0.15Cu, Bi-1.0Cu and Bi-5.0Ag samples with lower value in fracture strain, were fully exhibited the typically intra-granular brittle fracture mode showing the cleavage patterns in Bi grains. In contrast, Bi-0.5Cu with the highest value of 33% in fracture strain, did not only showed brittle fracture region, but also showed the secondary cracks and the curvature fracture surfaces, showing the plastic deformed outer rim with the reduction of area 4.3-40.7% as shown in Fig. 2.11. The secondary cracks and the curvature fracture surfaces were caused in deformable Cu parts. The microstructural characteristics including of the morphology and amount of the Cu phase were important because of the sensitivity of microstructure to the plastic deformation amount. The fracture strain behaviors could be comparable among each alloy, because each alloy was manufactured at the same conditions. Further, Bi-1.8Zn with the moderate value of 6.7% in fracture strain, showed the curvature edge in cleavage planes, which resulted from the dispersion of pure Zn particles and formation of Bi-Zn S.S.



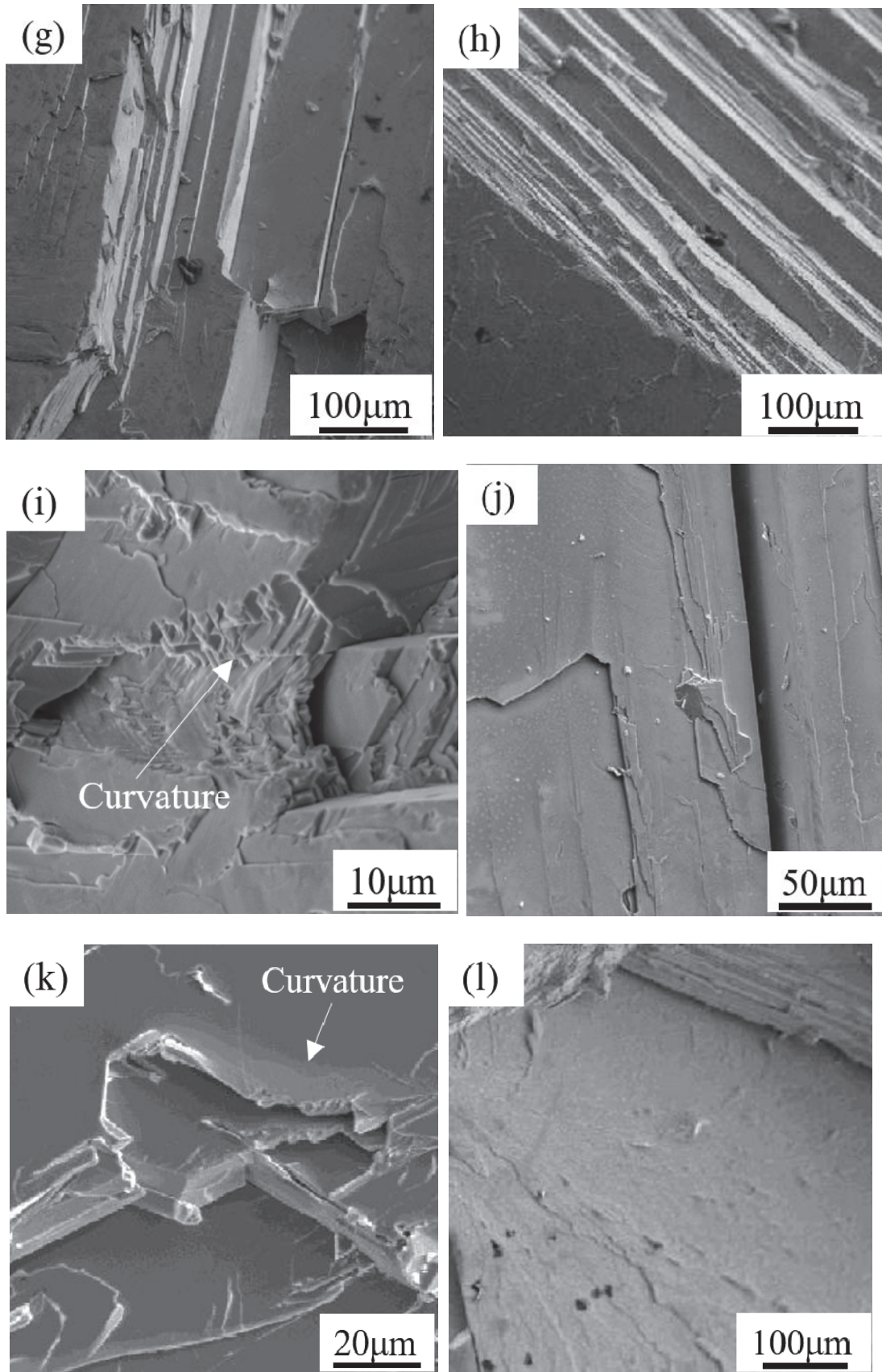


Fig. 2.12 SEM images of fracture surfaces of (a) pure Bi, (b) Bi-0.15Cu, (c) Bi-0.5Cu,

(d) Bi-1.0Cu, (e) Bi-1.8Zn, (f) Bi-5.0Ag alloys and high magnified images for fracture surfaces of (g) pure Bi, (h) Bi-0.15Cu, (i) Bi-0.5Cu, (j) Bi-1.0Cu, (k) Bi-1.8Zn, (l) Bi-5.0Ag alloys at 293 K. Each high magnified image, (g) to (l), corresponds to a black rectangle area of low magnification images in (a) to (f), respectively.

2.4.2.2 ΔMk parameter and mechanical properties

Figure 2.13 shows the relation between values in Rockwell hardness on B scale and ΔMk for binary alloys. The hardness was increased as the ΔMk or the amount of alloying elements were increased in alloys. It is roughly found that the hardness of binary alloys depended on the mixture rule on the basis of that in construction phases. Where, the value of H_{RB} in pure Cu was 90. There was the linear relation between the hardness and ΔMk in Mg alloys with dual phases as a simple metal ²⁵). In contrast, the hardness values were almost constant in the region of ΔMk more than 0.17. Further study is needed in order to understand the relation between the hardness and ΔMk in a more microstructural approach.

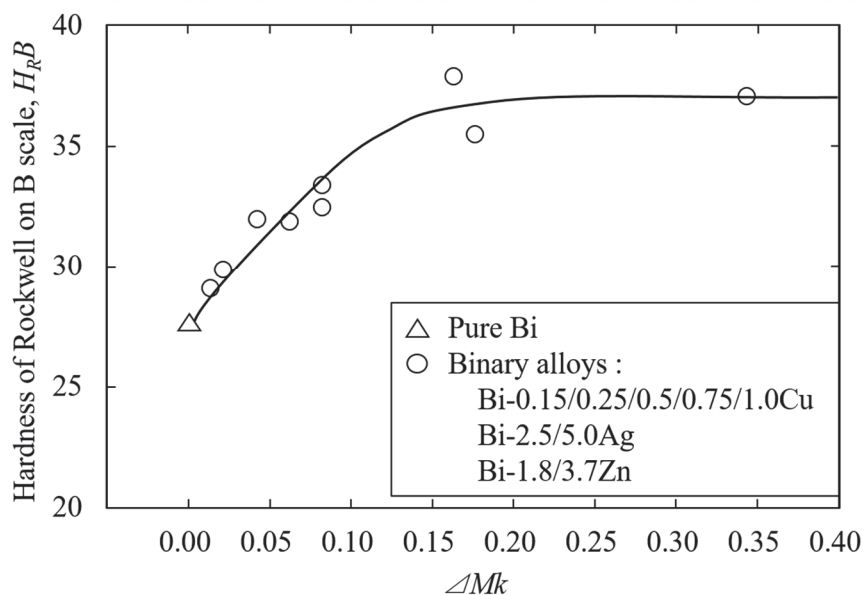


Fig. 2.13 Relation between hardness of Rockwell on B scale and ΔMk of binary Bi system alloys and pure Bi.

Figure 2.14 shows the relation between 0.2% proof stress, ultimate tensile strength or fracture strain and ΔMk for binary alloys at 293 K. The values of the 0.2% proof stress of Bi-0.15Cu, Bi-0.25Cu, Bi-0.5Cu, Bi-0.75Cu, Bi-1.0Cu, Bi-1.8Zn, Bi-3.7Zn, Bi-2.5Ag and Bi-5.0Ag were 8.0, 6.8, 7.1, 9.9, 12.5, 10.0, 18.1, 16.3 and 18.6 MPa, respectively. Figure 2.14 shows that the 0.2% proof stress of binary Bi system alloys were increased with increasing of ΔMk to approximately 0.17, regardless of kinds of alloying elements. And then the 0.2% proof stress became to almost constant with increasing of ΔMk more than 0.17. In contrast, the relationship between ultimate tensile strength and ΔMk of binary system alloys was same as that obtained from the 0.2% proof stress. The value of 0.2% proof stress of pure Bi was 7.5 MPa. It was also plotted in this figure. It is interesting that the values in the measured both strength of pure Bi agreed with the values which were obtained by extrapolation to ΔMk of zero using the predicted line for the both strength in binary alloys.

The behavior of 0.2% proof stress and ultimate tensile strength to ΔMk was same as that obtained from the hardness. As shown in Table 2.2, the values of mean grain sizes were almost same among experimental alloys, which corresponded to the same level for their grain boundary strengthening. It may be considered that there were different levels among the solid solution strengthening of experimental alloys. The mechanical properties of both tension and hardness might be also represented by ΔMk in Bi alloys, which agreed with the results obtained from Mg and Zn alloys^{14, 25}). In contrast, the maximum values, 25 and 33%, in the fracture strain were shown in Bi-0.25Cu and 0.5Cu alloys with ΔMk of 0.021 and 0.042, respectively.

It may be considered on the basis of the fracture behaviors, that the deformation of Bi alloys depended on both patterns of the intra-granular brittle fracture in pure Bi grains and deformable fracture in or near metallic grains of Cu, Ag and Zn by the stress relief in crack propagation. This fracture behaviors are similar to those of the composites consisting of ceramics/metals with nano-size, showing the improvement in fracture toughness values due to the presence of metallic parts²⁶). Therefore, it may be considered that maximum values in fracture strain were shown by the optimization in both the size and amount of Cu particles in eutectic regions in Bi-0.25 and 0.5 Cu alloys.

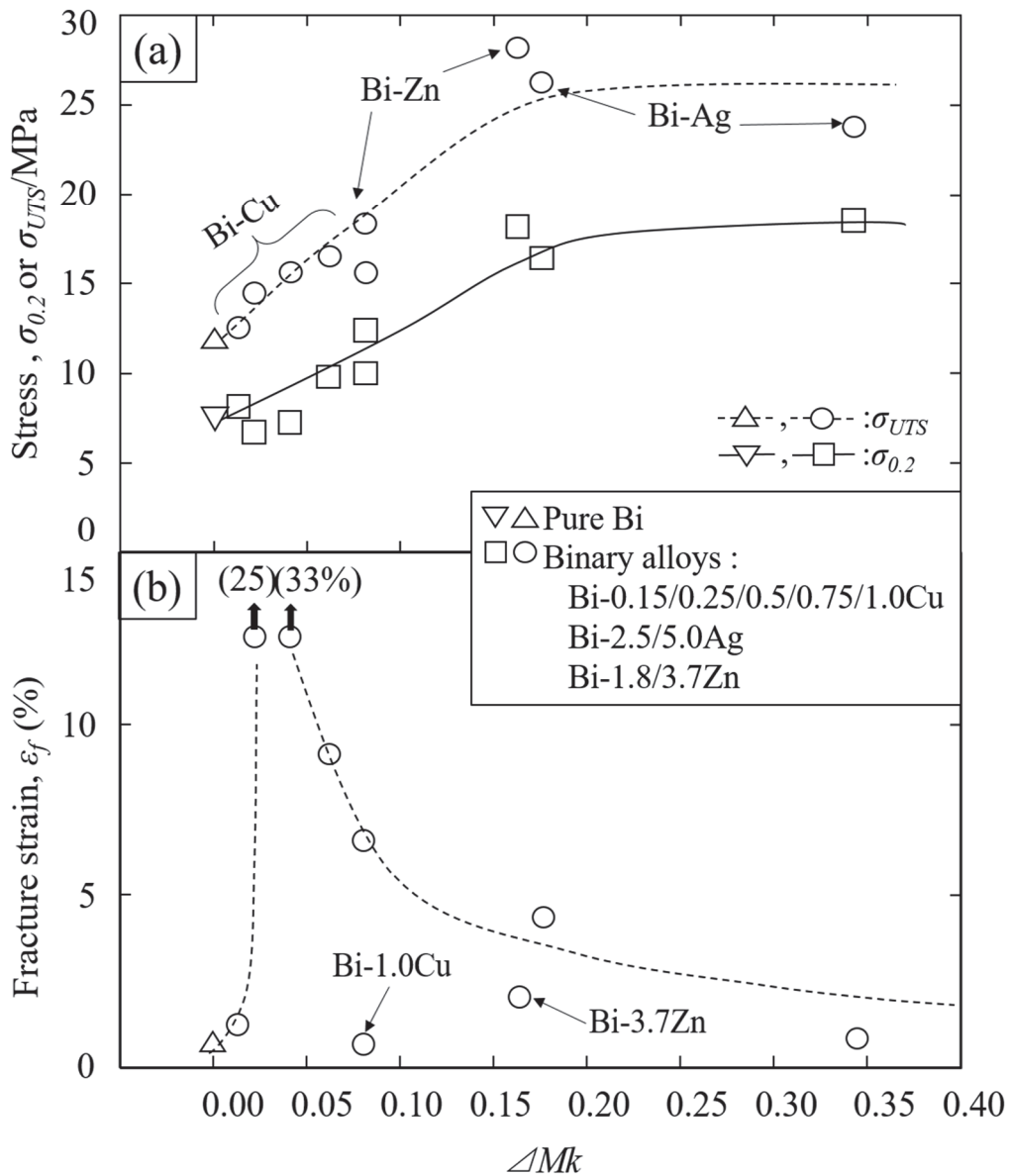


Fig. 2.14 Relation between the (a) 0.2% proof stress, ultimate tensile strength or (b) fracture strain and ΔMk of binary Bi system alloys at 293 K.

There were the Bi area as a continuous phase and little amounts of deformable metallic particles such as Cu, Ag and Zn in alloys. This meant to predominant action for plastic deformation by both the solid solution hardening and grain boundary hardening of their metallic particles, because of limited deformation in Bi grains. It may

be considered that their hardening mechanisms correlate to ΔMk . Actually, in previous work, ΔMk varied linearly with the 0.2% proof stress and tensile strength of commercially available wrought Al alloys (1000-7000 series) with multiple components^{22,25}). Strength properties including both strain hardening and precipitation hardening were treated well in terms of this parameter alone^{22, 25}). Further, it has been concluded that the interaction between the proof stress and dislocation density or hindrance for dislocation migration at the constant strain could be explained by ΔMk , which might lead to the indication of solid solution hardening level using this parameter for Al-1.5Mn-X ternary alloys²¹). Therefore, it may be presumed even under this condition of few or no solubility of each element into Bi, that the mechanical properties were roughly predicted by the values of ΔMk considering on the basis of fracture behaviors, because this parameter correlated to dislocation behaviors such as hindrance for dislocation migration in or near metallic parts by the increase or addition of alloying elements. Further study is greatly needed in order to understand the present ΔMk approach in a more fundamental manner such as the observation of dislocation behaviors by TEM.

2.4.3 Tensile properties on binary Bi-Cu/Ag/Zn alloys at 423 K

Figure 2.15 shows the nominal stress-strain curves for 9 of the binary Bi system alloys as determined through tensile tests at 423 K; that for pure Bi is shown as a reference. Typical softening can be seen in the stress-strain curves as compared to the curves obtained at 293 K. The ultimate tensile strength and fracture strain of pure Bi were 4.2 MPa and 15.4%, respectively. Thus, pure Bi exhibited the lowest ultimate tensile strength and fracture strain. For the Bi-0.15/0.25/0.5/0.75/1.0Cu alloys, the ultimate tensile strengths were 4.4, 4.9, 5.2, 5.8, and 5.4 MPa, respectively. Further, the fracture strains of these alloys were as least twice as large as that of pure Bi, even though their ultimate tensile strength and flow stress values were only slightly greater than those of Bi. In contrast, the ultimate tensile strength values of the Bi-2.5/5.0Ag and Bi-1.8/3.7Zn alloys were 8.8, 9.9 and 8.3, 10.4 MPa, respectively; these are 2.0 to 2.5 times

greater, respectively, than that of pure Bi. Moreover, the fracture strains of the two Bi-Ag/Zn system alloys were similar to those of the Bi-Cu system alloys. Thus, the tensile properties of the Bi alloys at 423 K improved with the addition of the alloying elements, namely, Cu, Ag and Zn.

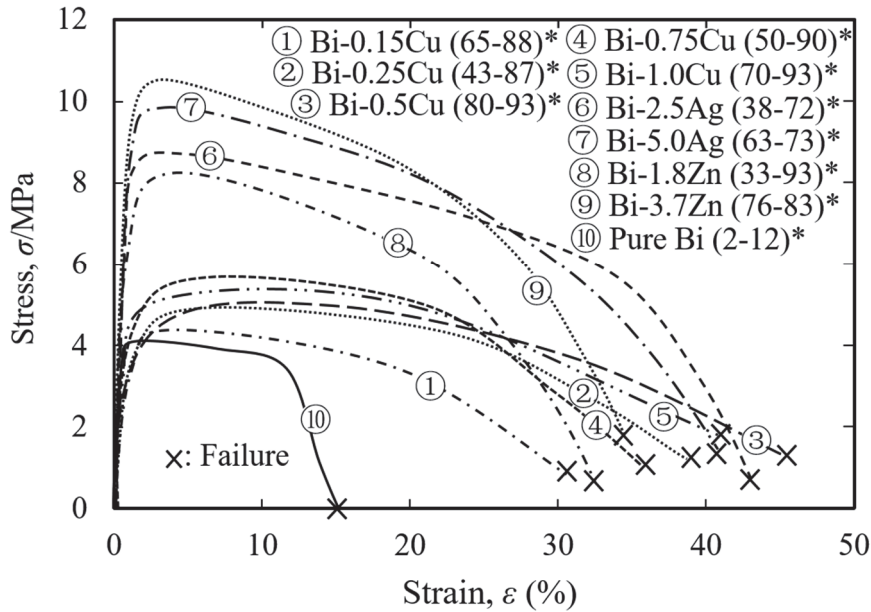
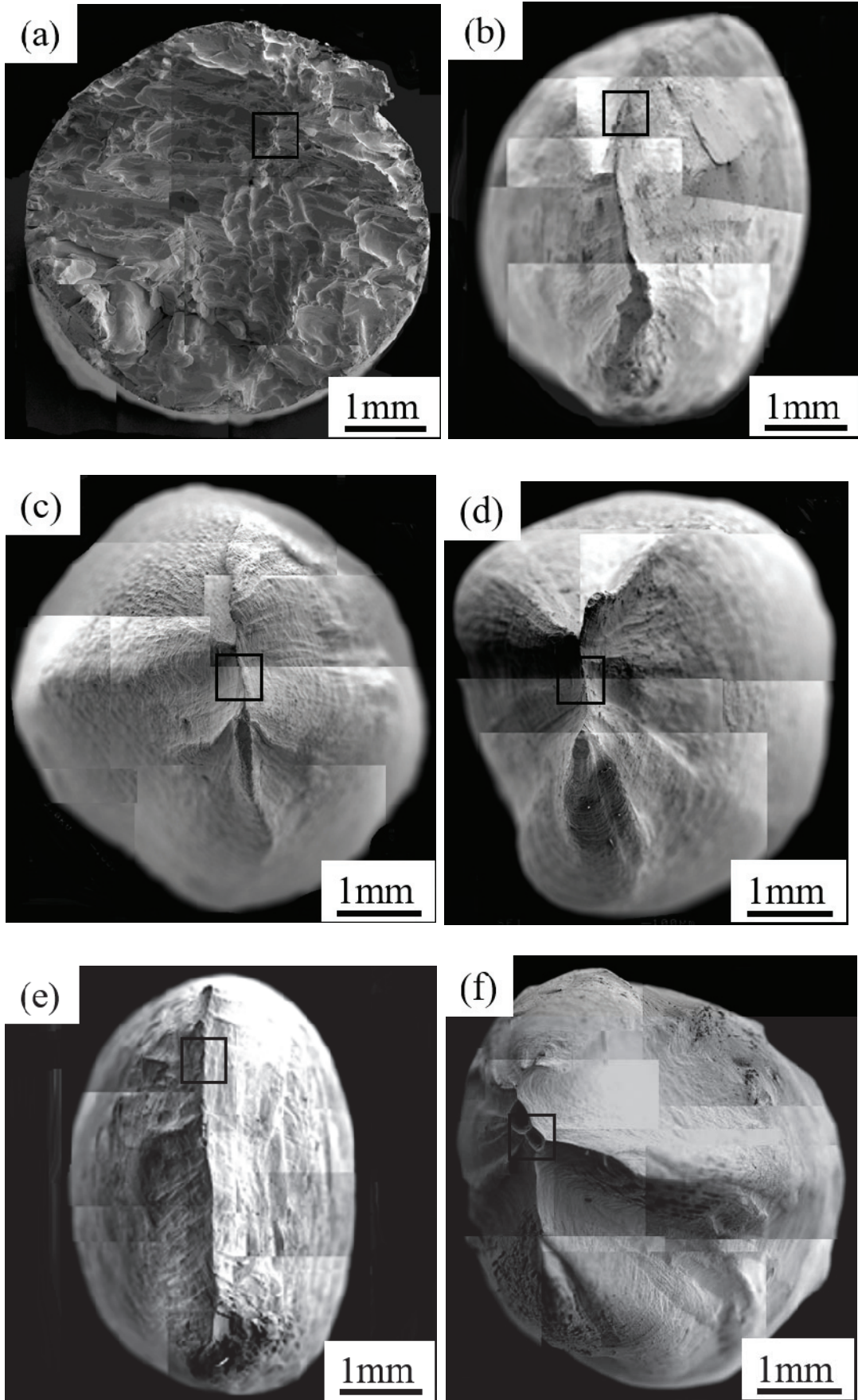


Fig. 2.15 Stress-strain curves of Bi-0.15Cu, Bi-0.25Cu, Bi-0.5Cu, Bi-0.75Cu, Bi-1.0Cu, Bi-2.5Ag, Bi-5.0Ag, Bi-1.8Zn, Bi-3.7Zn alloys and pure Bi at 423 K. * Range of reduction in area (%) after failure.

The typical fracture surfaces of the Bi-0.15/0.5/1.0Cu, Bi-1.8Zn and Bi-5.0Ag alloys and pure Bi after the tensile tests at 423 K are shown in Fig. 2.16. The pure Bi sample has a wavy fracture surface with undeveloped voids; however, the decrease in area (2–12%) was the lowest in this case. In contrast, as shown in Fig. 2.16, the fracture ends of the Bi-0.15/0.5/1.0Cu, Bi-1.8Zn and Bi-5.0Ag alloys tested at 423 K had a dimple-like pattern consisting of several cavities, which were elongated along the stress axis close to failure. This resulted in a very large decrease in area, in keeping with the data shown Fig. 2.15. In addition, the fracture surface of Bi-0.15Cu, which showed the lowest fracture strain, not only exhibited a ductile-fracture-like pattern but also a partially brittle-fracture-like pattern, even at 423 K.



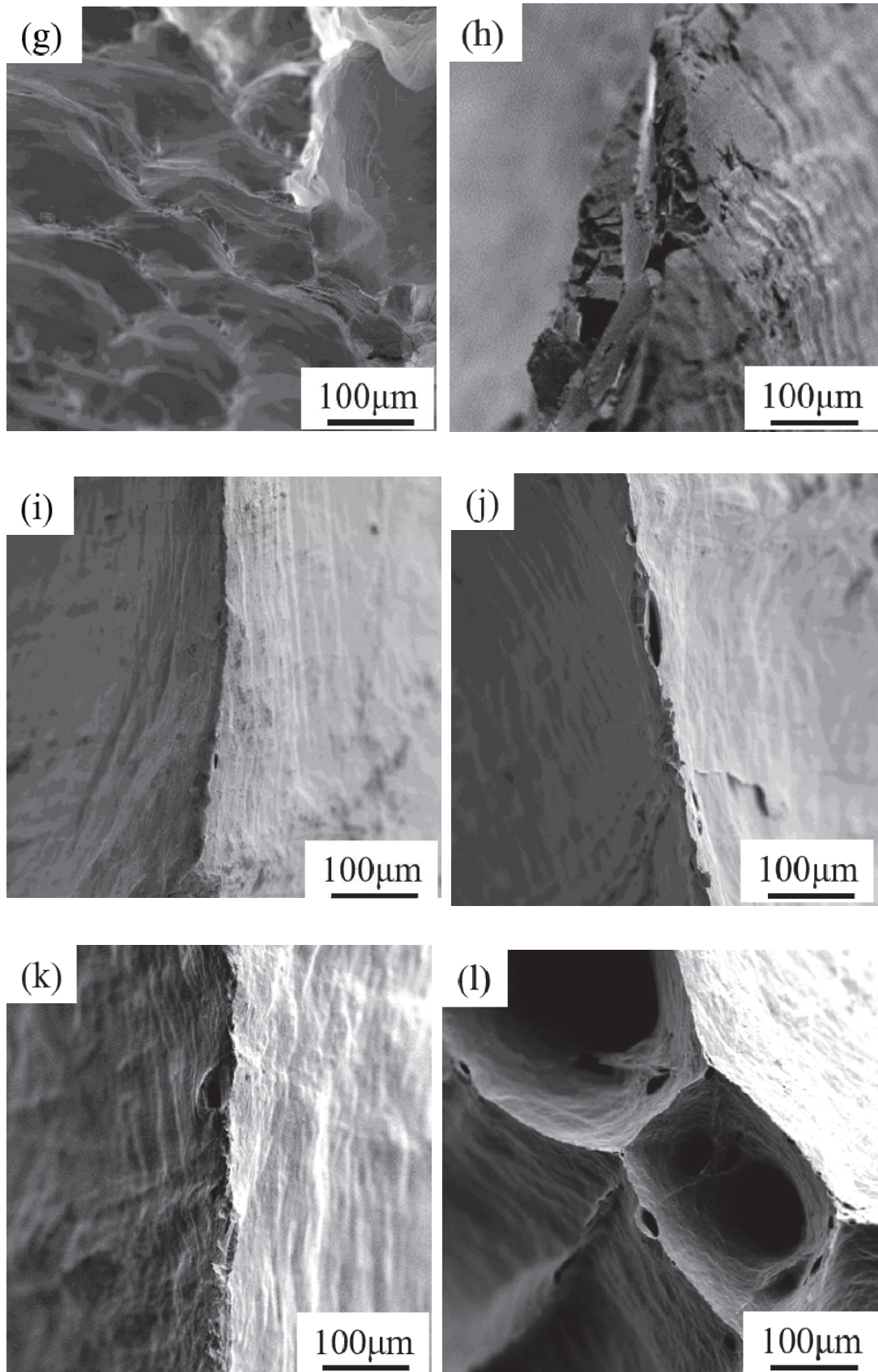


Fig. 2.16 SEM images of fracture surfaces of (a) pure Bi, (b) Bi-0.15Cu, (c) Bi-0.5Cu,

(d) Bi-1.0Cu, (e) Bi-1.8Zn, (f) Bi-5.0Ag alloys and high magnified images for fracture surfaces of (g) pure Bi, (h) Bi-0.15Cu, (i) Bi-0.5Cu, (j) Bi-1.0Cu, (k) Bi-1.8Zn, (l) Bi-5.0Ag alloys at 423 K. Each high magnified image, (g) to (l), corresponds to a black rectangle area of low magnification images in (a) to (f), respectively.

Figure 2.17 shows the relationship between the 0.2% proof stress, the ultimate tensile strength or fracture strain and ΔMk for binary alloys at 423 K. The 0.2% proof stress and ultimate tensile strength increased with an increase in ΔMk till approximately 0.17 and then remained almost constant; this was regardless of the type and amount of binary and ternary alloying elements used. This relationship at 423 K was similar to that seen at 293 K. The 0.2% proof stress and ultimate tensile strength of pure Bi for a ΔMk of 0.00 could be also fitted using the relationship between the parameters and the ΔMk value for the experimental alloys. It is interesting to note that the measured stress levels of pure Bi agreed with those obtained by the extrapolation to ΔMk .

The number of slip systems also in the Bi alloys increased with an increase in the temperature. In addition, the effect of the precipitates on the retardation of the migration of dislocations was different for the different slip planes. Therefore, it may be considered that the relationship between the fracture strain and ΔMk changed with the increase in the test temperature. On the other hand, as shown in Fig. 2.9, the morphologies of the alloys changed with an increase in the amounts of the alloying elements. Thus, the phenomena arising from the retardation of dislocation migration, such as solid-solution hardening, precipitation hardening, and the Orowan effect, also changed. It may also be considered that the relationship between the alloy strength and ΔMk was not proportional to the change. Moreover, when the amounts of the alloying elements added were low levels, the relationship between the alloy strength and ΔMk was linear for both the binary and the ternary Bi system alloys.

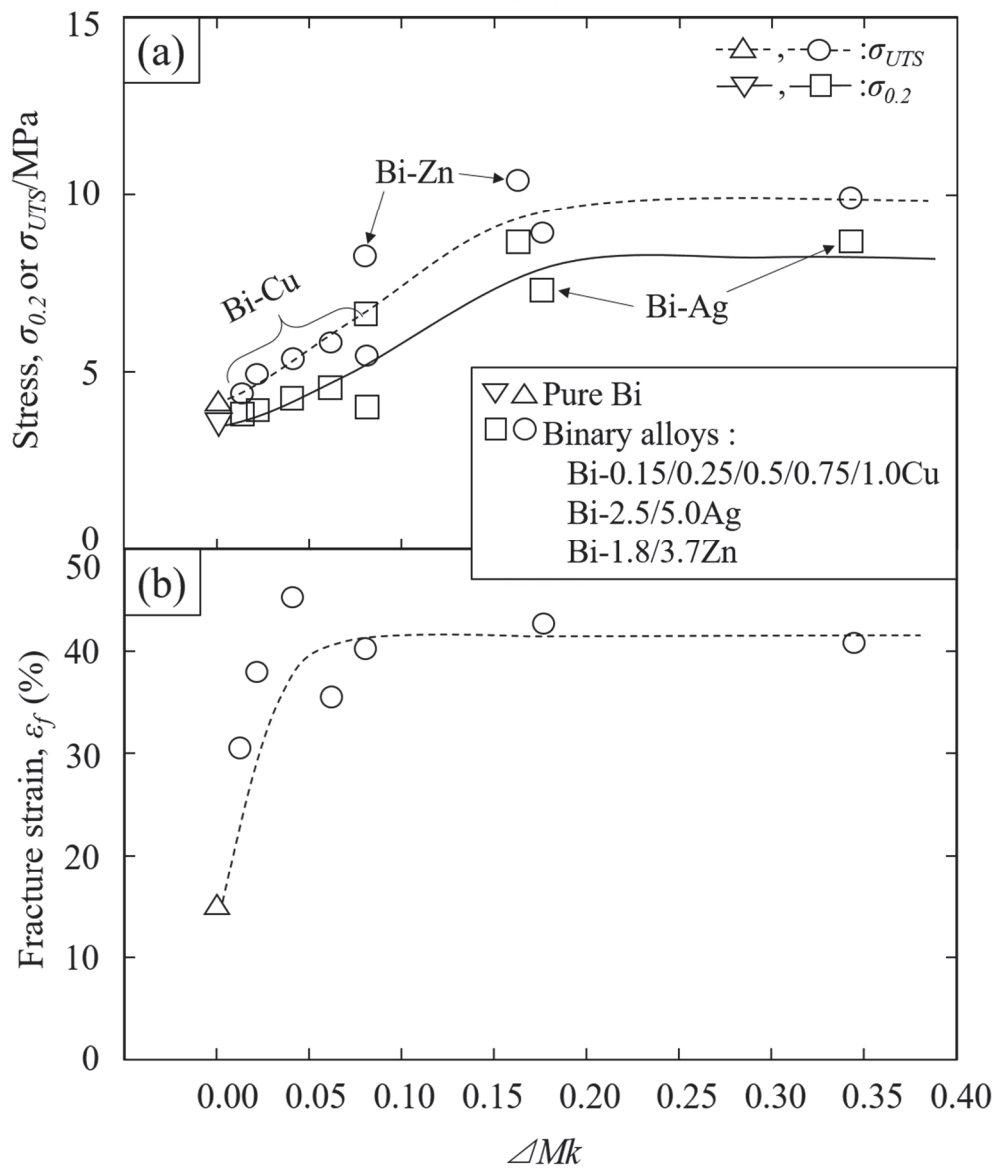


Fig. 2.17 Relation between the (a) 0.2% proof stress, ultimate tensile strength or (b) fracture strain and ΔMk of binary Bi system alloys at 423 K.

2.5 Summary

(1) The values in Rockwell hardness on B scale of binary Bi system alloys were all higher than pure Bi. The hardness was increased as the ΔMk until 0.17. In contrast, the hardness values were almost constant in the region of ΔMk more than 0.17.

(2) The 0.2% proof stress, ultimate tensile strength and fracture strain of binary Bi system alloys were also all higher than pure Bi. The behavior of 0.2% proof stress and ultimate tensile strength to ΔMk was same as that obtained from the hardness. The relationship between 0.2% proof stress, ultimate tensile strength or fracture strain and ΔMk indicated that ΔMk was effective to predict the mechanical properties of Bi solder alloys.

(3) Both 0.2% proof stress and ultimate tensile strength at 423 K for binary alloys were decreased compared with their values at 293 K. Furthermore, the relationship between the strength at 423 K and ΔMk was similar to that observed during tests at 293 K.

References

- 1) K. Tsuruta: Met. Technol. (Jpn.), **74** (2004)1244-1248.
- 2) Fuji Electric: Fuji Electric Journal, **84** (2011) No.1, No.5.
- 3) Nikkei Electronics, Abstract of Seminar: 2010.
- 4) R. Mahmudi, M. Eslami: Mater. Sci. Mater. Electron. **22** (2011) 1168-1172.
- 5) C. Leinenbach, F. Valenza, D. Giuranno, H. Elsener, S. Jin, R. Novakovic: Electron. Mater. **40** (2011) 1533–41.
- 6) T. Gancarz, J. Pstrus, P. Fima, S. Mosinska: Mater. Eng. Perform. **21** (2012) 599–605.
- 7) C. Wang, H. Chen, P. Li: Materials Chemistry and Physics **136** (2012) 325-333.
- 8) J.Y. Tsai, C.W. Chang, Y.C. Shieh, Y.C. Hu, C.R. Kao: Electron. Mater. **34** (2005) 182.
- 9) C. Leinenbach, F. Valenza, D. Giuranno, H.R. Elsener, S. Jin, R. Novakovic: Electron. Mater. **40** (2011) 1533.
- 10) S.J. Kim, K.S. Kim, S.S. Kim, K. Sukanuma: Electron. Mater. **38** (2009) 266.
- 11) K. Sukanuma, S. J. Kim and K.S. Kim: JOM, **61** (2009) 64-71.
- 12) T. Iseki, M. Takamori: J. J. Institute of Electronics Packaging, **15** (2012) 153.
- 13) J. C. Slater, Quantum theory of molecules and solids, Vol.4, McGraw-Hill, New York (1974).
- 14) R. Ninomiya, Doctoral thesis, Toyohashi University of Technology (1996) pp.124-130.
- 15) M. Tsukada, H. Adachi and C. Satoko: Progress in Surface Science **14** (1983) 113.
- 16) M. Morinaga and N. Yukawa: *Computer Aided Innovation of New Materials*, ed. by M. Doyama *et al.*, (North-Holland, 1991) pp. 803-808.
- 17) M. Morinaga, N. Yukawa and H. Adachi: Tetsu-to-Hagane **72** (1986) 555-562.
- 18) W. J. Boesch and J. S. Slaney: Metal Progress **86** (1964) 109-111.

- 19) L. Pauling: Phys. Rev. **54** (1938) 899.
- 20) M. Morinaga, N. Yukawa, H. Adachi and H. Ezaki: *Superalloys* 1984, (The Metallurgical Society of AIME, Warrendale, PA, 1984) pp. 523-532.
- 21) K. Matsugi, S. Yamamura, Z. F. Xu, Y. B. Choi, K. Sugio, G. Sasaki and N. Oda: Materials Transactions **56** (2015) 1675-1682.
- 22) M. Morinaga and S. Kamado: Model. Simul. Mater. Sci. Eng. **1** (1993) 151-164.
- 23) M. Moringa, S. Nasu, H. Adachi, J. Saito and N. Yukawa: J. Journal of Physics, **3** (1991) 6817.
- 24) R. S. Mulliken: J. Chem. Phys, **23** (1955) 1833, 1841, 2339 and 2343.
- 25) R. Ninomiya, H. Yukawa, M. Morinaga: Japan Inst. Light Metals **44** (1994) 171-177.
- 26) T. Sekino, Y. Choa, A. Nakahira and K. Niihara: Materia Japan **38** (1999) 425-428.
- 27) M. Yu, Z. Xu, Y. Choi, K. Matsugi, S. Motozuka, K. Suetsugu and J. Yu: 9th Pacific Rim International Conference on Advanced Materials and Processing (2016) pp. 225-230.

Chapter 3

Promising compositions of Bi alloys and their characterizations

3.1	<i>Introduction</i>	58
3.2	<i>Experimental procedure</i>	60
3.2.1	<i>Materials and manufacturing process</i>	60
3.2.2	<i>Evaluation of some properties</i>	60
3.3	<i>Results and discussion</i>	68
3.3.1	<i>Microstructures</i>	68
3.3.2	<i>Mechanical properties on ternary alloys</i>	69
3.3.2.1	<i>Tensile properties at 293 K</i>	69
3.3.2.2	<i>Temperature dependence of tensile properties</i>	70
3.3.2.3	<i>Relation between mechanical properties and ΔM_k</i>	74
3.3.3	<i>Melting points</i>	77
3.3.4	<i>Wettability</i>	78
3.3.5	<i>Thermal conductivity</i>	80
3.4	<i>Summary</i>	81
	<i>References</i>	82

3.1 Introduction

Solder alloys with high-melting points are used widely in power semiconductor packaging. High-lead-content alloys, which have been employed as high-temperature solder alloys, have a solidus temperature of more than 533 K ¹⁾. In recent years, owing to the RoHS (The Restriction of the Use of Certain Hazardous Substances in Electrical and Electronic Equipment Regulations 2012) and End of Life Vehicles Directives of EU, lead-free high-melting-point solder alloys have been promoted in the electronics industry ²⁾. Therefore, significant efforts are being devoted all over the world towards the development of lead-free solders. However, there have not been significant advances in the development of lead-free solders for high-temperature applications ^{3,4)}. Several research groups have focused on Au-Sn, Zn-Sn, and Bi-Ag system alloys as potential lead-free alloys, based on their thermal and electricity properties and their melting points ⁵⁻¹²⁾. However, Au system alloys find limited use as high-temperature solders because of the high cost of Au ⁵⁾. The applicability of Zn system alloys is also limited because of the oxidability of Zn ⁶⁻⁹⁾. On the other hand, the melting point of Bi is 544 K, which is similar to that of conventional high-temperature Pb-Sn solders ¹⁰⁻¹²⁾. Moreover, Bi is not only cheap but is also not harmful to human health and the environment. Thus, Bi system alloys are being considered for use as Pb-free alloys for high-temperature solders ^{13,14)}.

So far, high-performance alloys have been developed through trial-and-error experiments performed based on a few empirical rules. In order to develop new alloys more efficiently, a theoretical design approach is strongly needed. The concept of d-electrons based on the theoretically determined electronic structures of alloys using discrete variational (DV)-X α ¹⁵⁻¹⁷⁾ cluster calculations was proposed by Morinaga et al. ^{18, 19)}. This concept was first used in the case of austenitic Ni, C, and Fe alloys, wherein the phase boundary as well as a few physical and mechanical properties were predicted based on electronic parameters such as the d-orbital energy level and bond order. Moreover, the compositional optimization of Al ²⁰⁾ system alloys as a simple metal was performed based on the s-orbital energy level (Mk) ¹⁵⁻¹⁷⁾. The relationship between the dislocation density (or hindrance to dislocation migration) and $\angle Mk$ has

also been investigated previously ²¹⁾. It was concluded that the ΔMk value could be used as an indicator of the level of solid-solution hardening in ternary Al-1.5Mn-xMg alloys consisting of a mono phase.

We were able to determine the Mk value of a few alloying elements in a Bi cluster model by using the DV-X α cluster method in chapter 2. It was observed that there exists a relationship between the ultimate tensile strength or fracture strain at 293 K or 423 K and ΔMk in the case of binary Bi-Cu/-Ag/-Zn alloys with near-eutectic compositions. The mechanical properties of the alloys such as their tensile properties and hardness could be predicted based on the ΔMk value. However, these alloys exhibited the desired properties, namely, a ultimate tensile strength of 20 MPa and fracture strain of 5% at 293 K.

In the present study, the high-temperature tensile properties were measured on promising ternary Bi-Cu-Ag system alloys proposed by ΔMk parameter. In contrast, the melting points, thermal conductivities, and wettabilities with respect to Cu of the alloys at high temperatures were also measured, in order to evaluate their suitability for practical applications. The desired characteristics of the high-temperature solders were considered to be a melting point higher than 533 K ¹⁾, and a contact angle on Cu of less than 90 degree.

3.2 Experimental procedure

3.2.1 Materials and manufacturing process

The melt equipment and the casting mold were same with chapter 2. Stick-like Bi (purity of 99.99%), granular Ag (purity of 99.99%), and laminar Cu (purity of 99.9%) were placed in a graphite crucible, which was then set in an electric furnace in air. The diameters of the Bi and Ag samples were 2–3 mm, while the thickness of the Cu sample was 1 mm. Once all the starting materials had melted, the melt was mixed with a ceramic stick at 773 K and held at this temperature for 1.8 ks. Next, the melt was poured into a casting mold heated to 773 K. The resulting ingot which had a diameter of 15 mm and height of 115 mm, was air cooled to 293 K. The compositions of the experimental alloys are listed in Table 3.1.

Table 3.1 The nominal composition, ΔMk and mean grain size of ternary Bi system alloys.

Alloys (mass.%)	Alloys (mol%)	ΔMk	Mean grain size (μm)
Bi-2.0Ag-0.5Cu	Bi-3.8Ag-1.6Cu	0.180	39
Bi-5.0Ag-0.5Cu	Bi-9.2Ag-1.6Cu	0.379	43

3.2.2 Evaluation of some properties

The microstructures of the alloys were observed using scanning electron microscopy (SEM). Tensile tests were performed on the alloys at 293, 323, 348, 373, 423, and 473 K in air using a mechanical testing machine (Autograph DCS-R-5000, Shimadzu Corporation, Japan); the tests were performed using an initial strain rate of $3.4 \times 10^{-4} \text{ s}^{-1}$. The dimensions of the gauge section of the tensile test specimens were 6 mm (diameter) \times 20 mm (length), which same with chapter 2. Moreover, the infrared furnace used in chapter 2 was also used to raise the test temperature in this study. In

addition, the fracture surfaces of the tensile samples were observed by SEM.

Differential Thermal Analysis (DTA) was used to characterize the melting points of the alloys. DTA is a method of measuring the temperature difference between both substances as a function of temperature while changing the temperature of the measurement sample and the reference material (generally Al_2O_3) according to a certain program. That means a sample and a reference substance are placed in a furnace, and the temperature difference ΔT between the both in the temperature rising or temperature decreasing process is detected. A schematic diagram of the DTA device is shown in Fig. 3.1. Place the sample and reference material at symmetrical positions in the furnace and change the temperature of the sample and the reference material by changing the heater of the furnace according to the temperature program. A thermocouple is arranged in a differential type and the temperature difference ΔT between the sample and the reference material is detected. This signal of ΔT is called a DTA signal. The sample temperature T is detected from the thermocouple on the sample side.

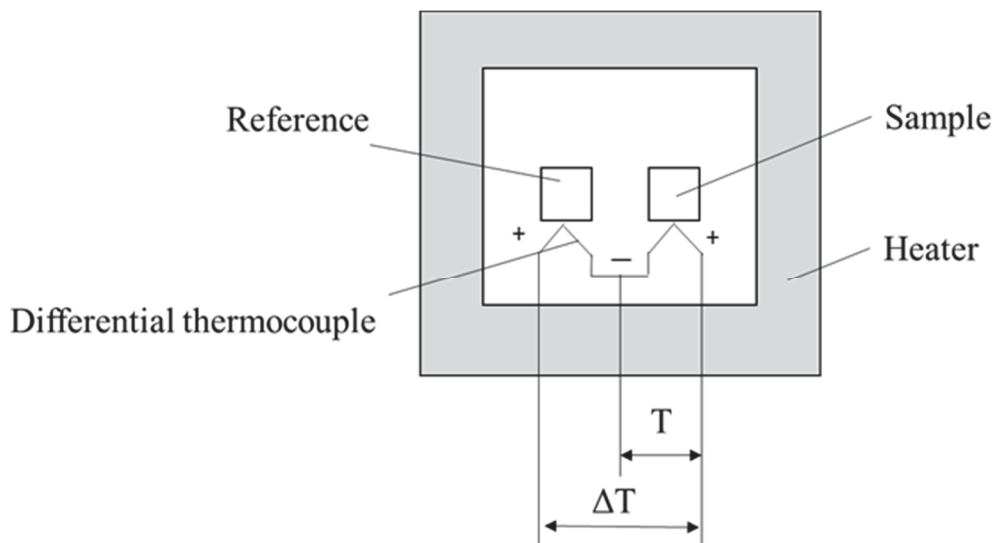


Fig. 3.1 Schematic illustration of differential thermal analysis ²²⁾.

Figure 3.2 shows the time change of the heater, reference material and sample temperature during measurement. Moreover, Fig. 3.3 shows the time change of the temperature difference ΔT between the reference material and sample temperature detected by the differential thermocouple. When the temperature rise of the furnace is

started, the temperature of the sample and the reference material starts to rise slightly with a delay depending on the heat capacity, and then the temperature rises following the temperature of the heater. Since the reference material uses a substance which does not cause a thermal change in the measurement temperature range, the temperature rises at the same slope as the heater. ΔT changes until it reaches a steady state after the start of temperature rise, and after stabilization it becomes a substantially constant amount corresponding to the difference in heat capacity between the sample and the reference material. This content signal is called the baseline. When the temperature rises and a reaction such as melting occurs in the sample, the temperature rise of the sample stops as shown in Fig. 3.2, so ΔT becomes large, and when the reaction is completed, the temperature returns rapidly to the original temperature rise curve, ΔT also return to original. At this time, the signal of ΔT shows the reaction peak as shown in Fig. 3.3. As a result, it is possible to detect the transition temperature, the reaction temperature, etc. of the sample from the DTA signal. As shown in Fig. 3.2, the temperature difference due to heat absorption in the sample is taken in the minus direction and the temperature difference due to heat generation is taken as the plus direction, whereby it is recorded as an endothermic peak and the melting point of the substance can be known.

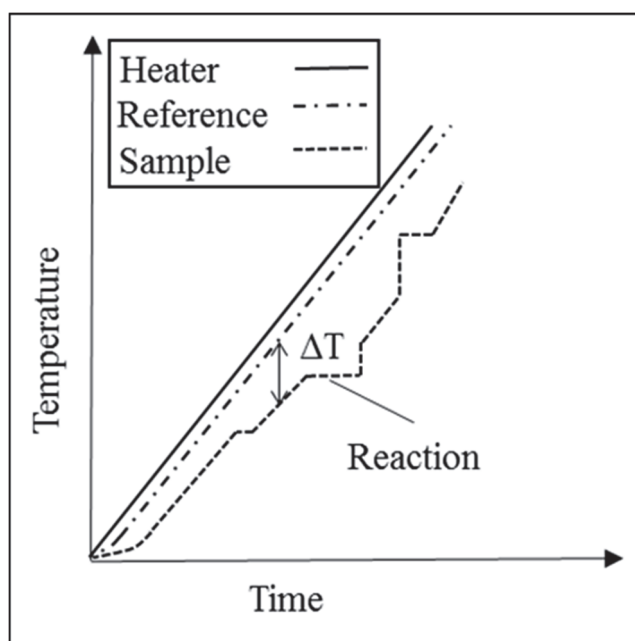


Fig. 3.2 Time change of temperatures for heater, reference and sample ²²⁾.

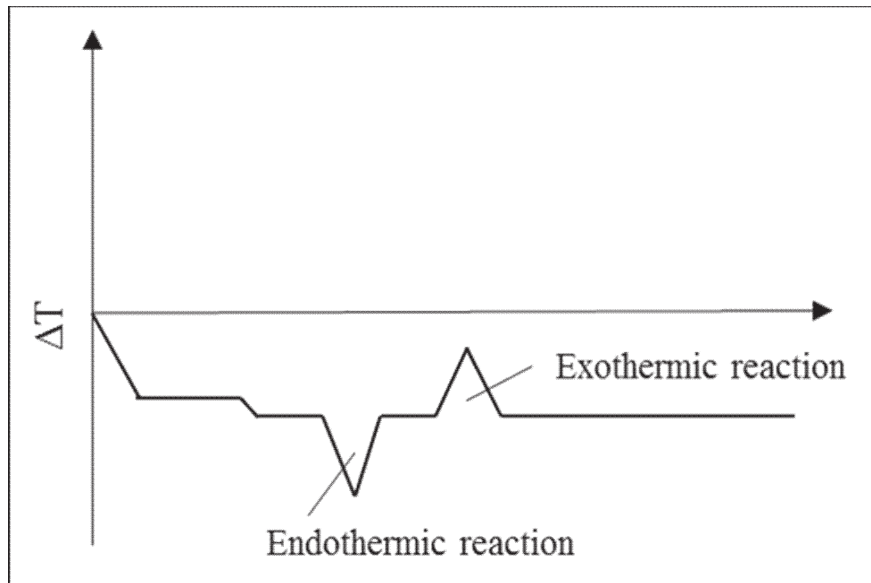


Fig. 3.3 Time change of difference in temperature between reference and sample ²²⁾.

Rectangular samples with dimensions of $3 \times 3 \times 3 \text{ mm}^3$ were employed for the purpose. Al_2O_3 (purity 99.9%) was used as a reference material. The DTA measurements were performed in an Ar atmosphere. A heating rate of 5 K/min was used, and the temperature was varied from 293 to 673 K, with the samples being held for 300 s at 673 K.

Wettability is a basic characteristics of solder. Wettability of solder represents easiness of solder and substrate attachment. Wettability tests were carried out using sessile drop method. Contact angle (θ) made between Bi alloys and the substrate was used to determine the wettability. Wetting relates to the contact between a liquid and a solid surface. It describes the ability of a liquid to spread over a solid surface. The extent of wetting is controlled by the thermodynamic tendency in order to minimize surface free energy. For a liquid droplet on a solid surface as shown in Fig. 3.4. Three forces of interfacial tension γ_s , γ_l and γ_{sl} are the surface tensions of solid–vapor, solid–liquid and liquid–vapor between the molten solder and the substrate. The surface energy of different components can be expressed by:

$$\gamma_s = \gamma_{sl} \cdot \cos \theta + \gamma_l \quad (3-1)$$

This is called Young's equation, and θ is called the contact angle. It is defined that θ will not get wet if $\theta > 90^\circ$, and at $\theta < 90^\circ$ the liquid droplet will wets the solid.

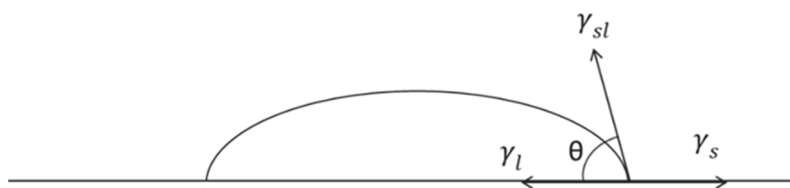


Fig. 3.4 The contact angle of the solder alloy.

As shown in Fig. 3.5, the contact angles between molten droplets of the experimental alloys and a Cu plate (purity of 99.9%) were measured in the atmosphere-controlled chamber with Mo heaters. The molten metal dripping apparatus consists of a Al_2O_3 tube and a glass tube, and a hole with a diameter of 1.0 mm is opened at the tip of the Al_2O_3 tube. This equipment diagram is shown in Fig. 3.6.

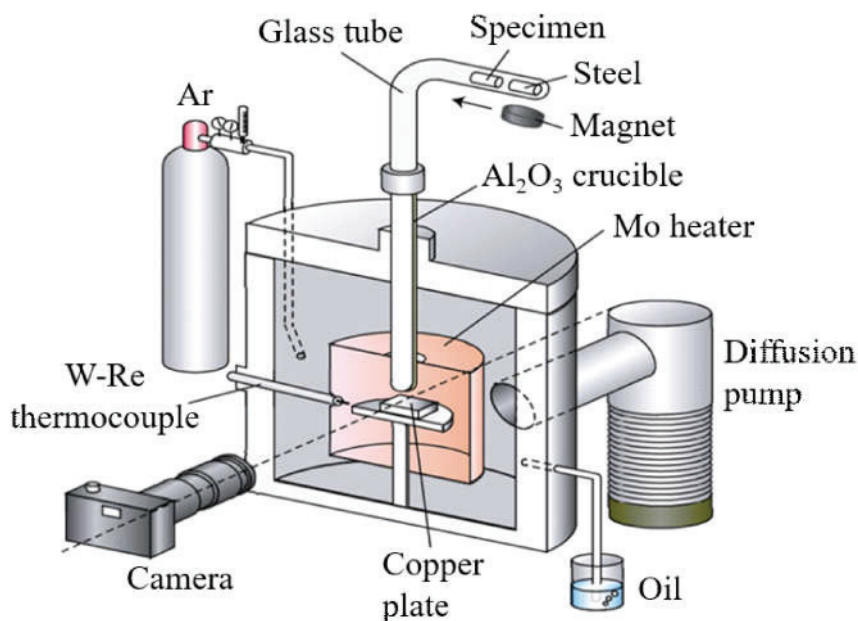


Fig. 3.5 Schematic diagram of contact angle tests.

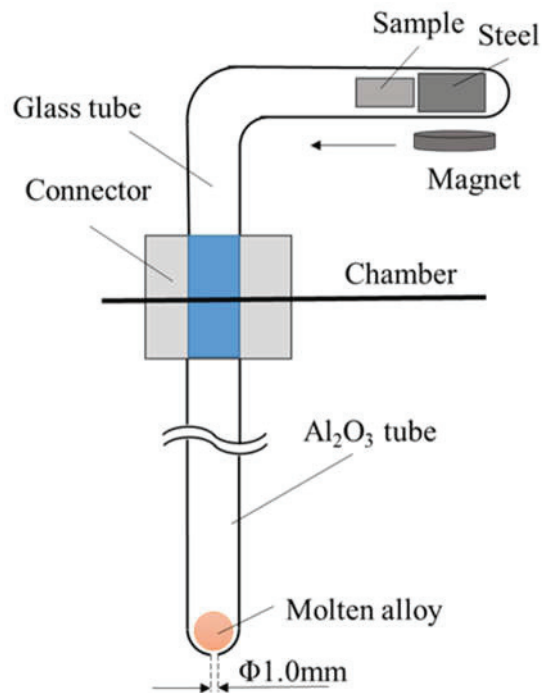


Fig. 3.6 Schematic diagram of sessile dropping tube.

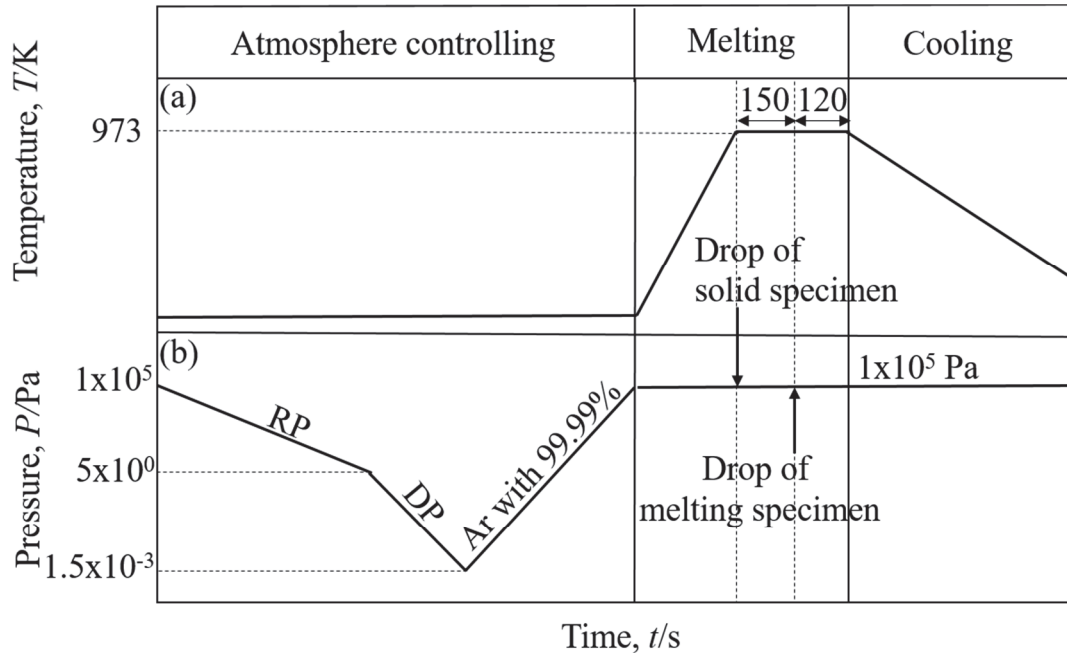


Fig. 3.7 Profiles of (a) temperature of Cu plate and (b) pressure in atmosphere of melting process.

Figure 3.7 shows profiles of press and temperature of Cu plate. First, the vacuum furnace was evacuated to 1.5×10^{-3} Pa and then heated to 973 K while using Ar as the shielding gas at a flow rate of 1.67×10^{-5} m³/s up to a pressure of 1.0×10^5 Pa. Then, a droplet of the molten alloy being tested was placed on the Cu plate at 973 K and photographed after 120 s. The volume of the droplets of the alloys was approximately 111 mm³. The surface of the Cu plate was finished to the polishing by Al₂O₃ particles paste with 0.3 μm.

Since the performance of electronic components such as LEDs and power system semiconductors deteriorates due to heat generation of chip elements, high heat dissipation is required for the bonding material for bonding the element and the substrate. The thermal conductivities of the alloys were measured using a laser flash thermal constant measurement system (TC-700, ULVAC-RIKO Inc., Japan)⁹⁾ at 293, 323, and 373 K. The test samples, which had dimensions of 10 (diameter) × 1 mm³ were also finished to the polishing by Al₂O₃ particles paste with 0.3 μm. The pulse laser light was irradiated on the surface of the sample, and a temperature hysteresis curve was obtained in which the sample temperature increased and decreased again with time, and the thermal conductivity was calculated. A thermocouple was attached to the back surface of the sample. The schematic diagram and the temperature curve are shown in Fig. 3.8.

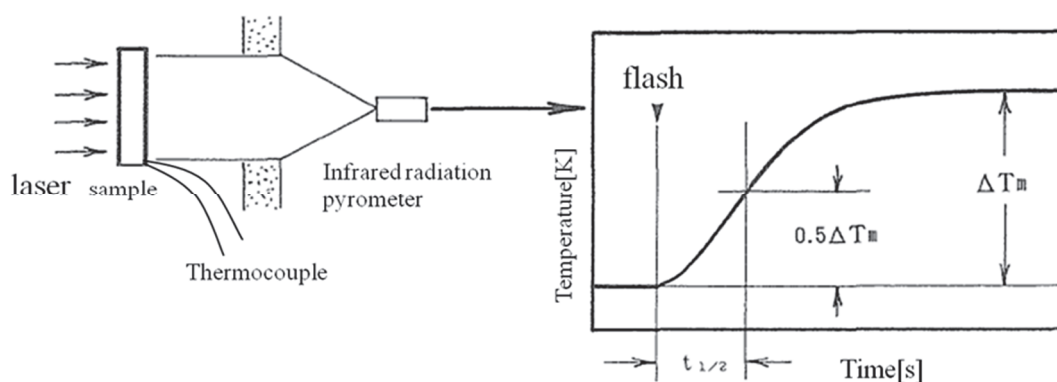


Fig. 3.8 Schematic illustration of the Laser-flash method²³⁾.

ΔT is the rising temperature of the sample, which can be expressed by:

$$\Delta T = \Delta T_m \left\{ 1 + 2 \sum_{n=1}^{\infty} (-1)^n \exp\left(-\frac{n^2 \pi^2 \alpha t}{L^2}\right) \right\} \quad (3-2)$$

where, ΔT_m is the maximum rising temperature, α is the thermal diffusivity of the sample, t is the elapsed time after pulse irradiation, and L is the thickness of the sample. It is reported that $\Delta T / \Delta T_m = 0.5$ when $\alpha t / L^2 = 0.1388$ in the temperature curve of Fig. 3.8. Therefore, by measuring the time ($t_{1/2}$) until the temperature rise ΔT of the sample reaches half of ΔT_m , the thermal diffusivity α can be obtained by the equation (3-3).

$$\alpha = \frac{0.1388 L^2}{t_{1/2}} \quad (3-3)$$

The maximum temperature rise ΔT_m of the sample is related to the specific heat capacity C_p by the equation (3-4).

$$C_p = \frac{Q}{\rho \cdot L \cdot \Delta T_m} \quad (3-4)$$

where, ρ is the density of the sample, and Q is the amount of heat absorbed by the sample when a laser pulse is applied. The thermal conductivity λ was calculated by the formula (3-5) by obtaining the thermal diffusivity α and the specific heat capacity C_p from the temperature curve.

$$\lambda = \alpha \cdot C_p \cdot \rho \quad (3-5)$$

3.3 Results and discussion

3.3.1 Microstructures

The microstructures of the Bi-2.0Ag-0.5Cu and Bi-5.0Ag-0.5Cu alloys consisted of primary phases and a typical eutectic structure composed of Bi, a Ag S.S., and a Cu S.S. in normal eutectic cells formed alternately, as shown in Fig. 3.9. In the Bi-5.0Ag-0.5Cu alloy, which had a large Ag content, an irregular region consisting of a darker needle-like primary Ag S.S. and a light-contrast primary Bi phase surrounding the primary Ag S.S. were also observed; this was indicative of the crystallization of Bi in the depleted region of the Ag S.S. owing to the formation of the primary Ag S.S. because of atomic diffusion under the nonequilibrium state. In particular, the large amount and size of primary phases with the rod like shape in Bi-5.0Ag-0.5Cu led the lower value in fracture strain, compared with Bi-2.0Ag-0.5Cu of a same alloying system, as mentioned in the term of 3.3.2. For their ternary alloys, the grain size of matrix was measured by the linear intercept method. The mean grain sizes were listed in Table 3.1, their values were 39 to 43 μm . Therefore, it is found that the values of mean grain sizes were measured in the almost same level among all experimental alloys.

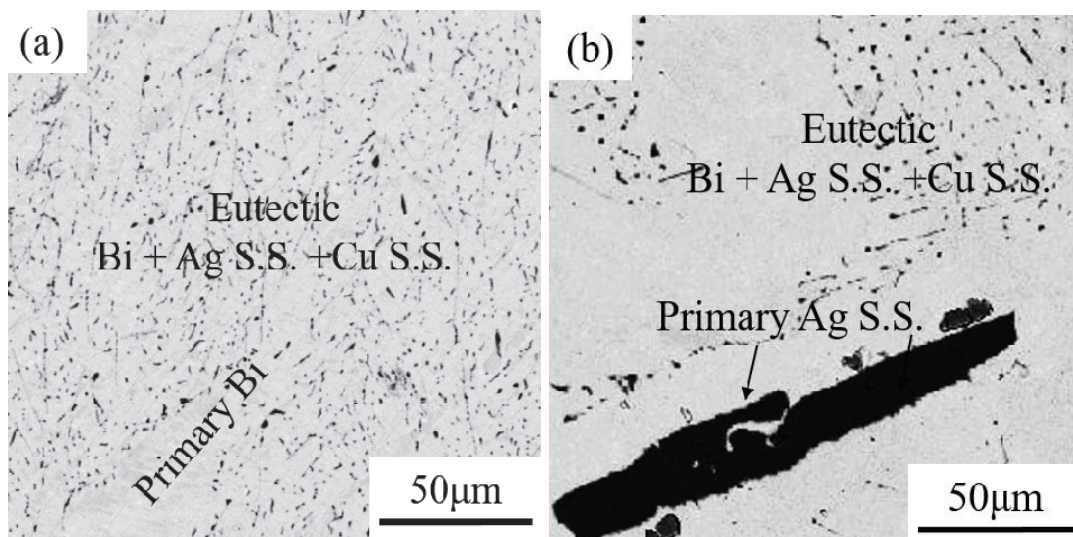


Fig. 3.9 Compositional images of (a) Bi-2.0Ag-0.5Cu and (b) Bi-5.0Ag-0.5Cu alloys.

3.3.2 Mechanical properties on ternary alloys

3.3.2.1 Tensile properties at 293 K

Ternary alloys were tensile tested and their results were shown in Fig. 3.10. Their alloys showed the improved flow stress and strain, compared with pure Bi. The values in the ultimate tensile strength of Bi-2.0Ag-0.5Cu and Bi-5.0Ag-0.5Cu alloys were 2.0 to 2.5-times larger than that of pure Bi. Moreover, the fracture strain of Bi-2.0Ag-0.5Cu and Bi-5.0Ag-0.5Cu were 4.7 and 2.8%, respectively.

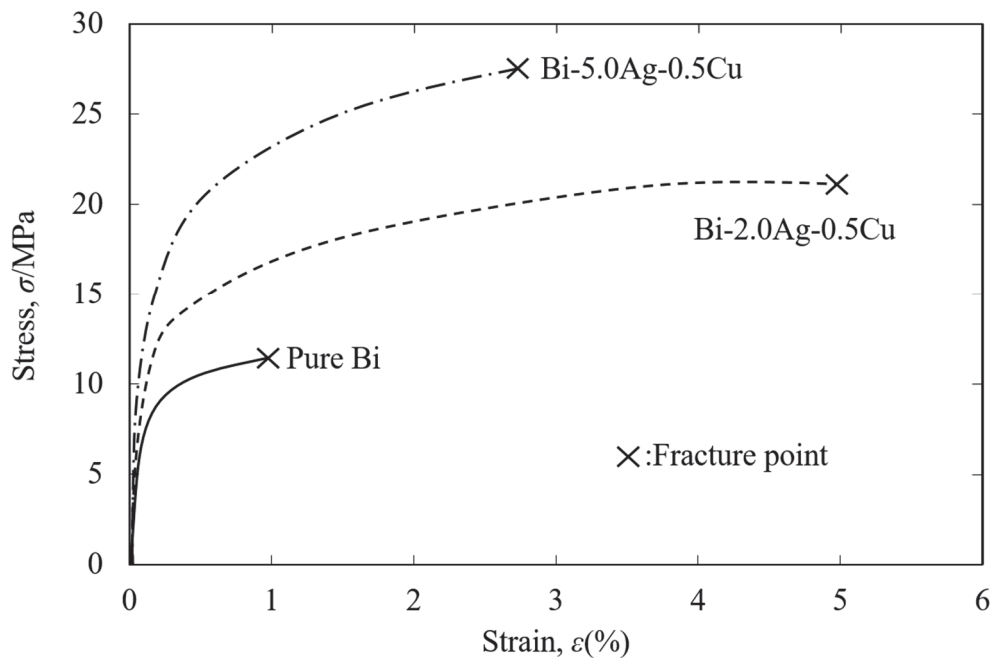


Fig. 3.10 Stress-strain curves of Bi-2.0Ag-0.5Cu, Bi-5.0Ag-0.5Cu and pure Bi at 293K.

The Bi-2.0Ag-0.5Cu with the moderate value of approximate 5% in fracture strain, showed the limited region showing unevenness fracture surfaces and minimized fracture units, as seen in Fig. 3.11. In contrast, the Bi-5.0Ag-0.5Cu samples with lower value in fracture strain, were exhibited the typically intra-granular brittle fracture mode showing the cleavage patterns.

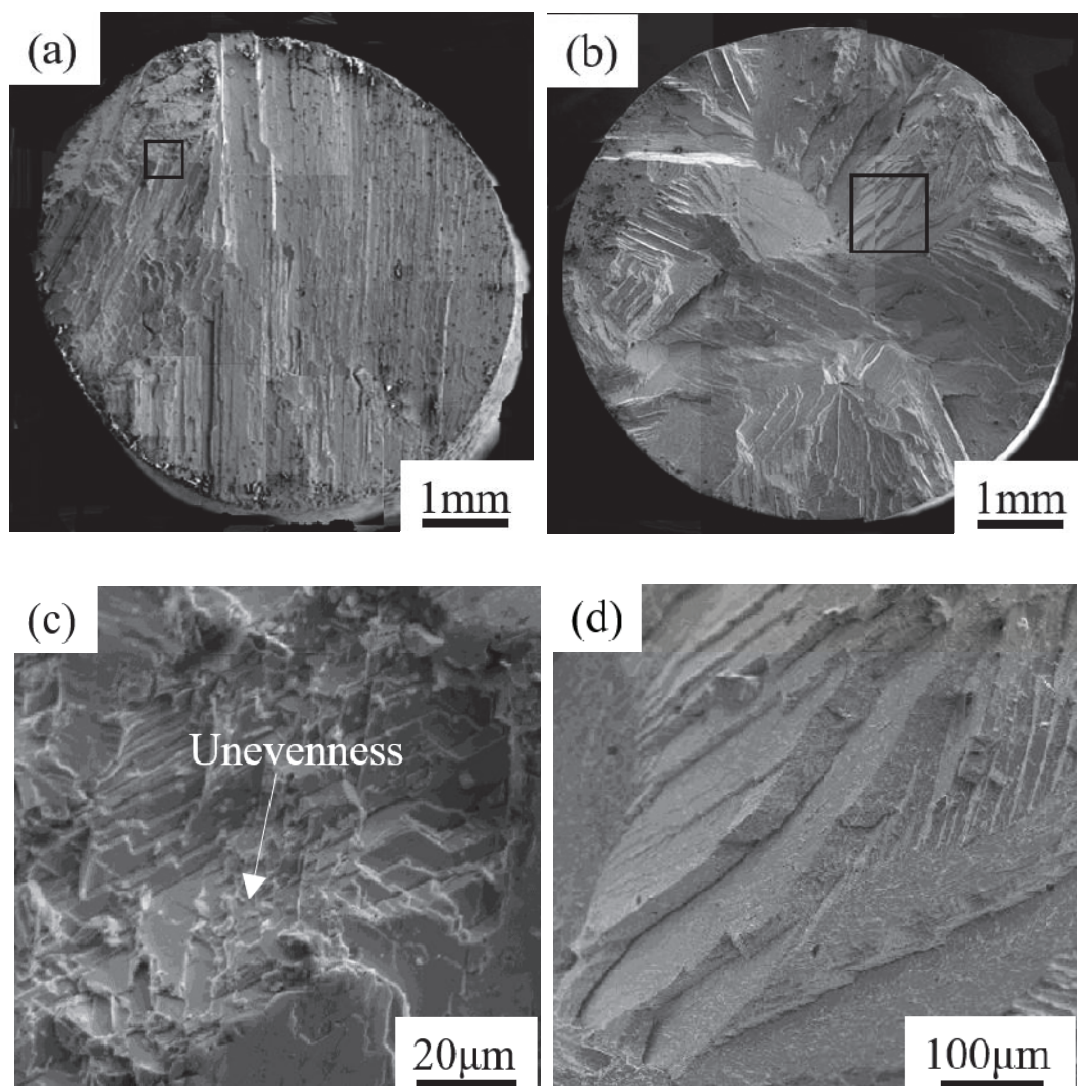


Fig. 3.11 SEM images of fracture surfaces of (a) Bi-2.0Ag-0.5Cu, (b) Bi-5.0Ag-0.5Cu alloys and high magnified images for fracture surfaces of (c) Bi-2.0Ag-0.5Cu, (d) Bi-5.0Ag-0.5Cu alloys at 293 K. Each high magnified image, (c) and (d), corresponds to a black rectangle area of low magnification images in (a) and (b), respectively.

3.3.2.2 Temperature dependence of tensile properties

Figures 3.12 (a) and (b) shows the nominal stress-strain curves as determined at various temperatures of the ternary Bi-2.0Ag-0.5Cu and Bi-5.0Ag-0.5Cu alloys. The flow stress values of both alloys decreased with the increase in the test temperature, owing to the softening of the alloys. Therefore, the stress-strain curves were obtained

at different test temperatures. In general, during plastic deformation, the alloys experienced simultaneous work hardening and dynamic recovery, phenomena which have opposite effects on plastic deformation. Dislocation annihilation occurred more quickly than did dislocation generation, resulting in the weakening of the hardening phenomenon, as the test temperature was increased. This behavior has also been observed in the case of solder materials ²⁴).

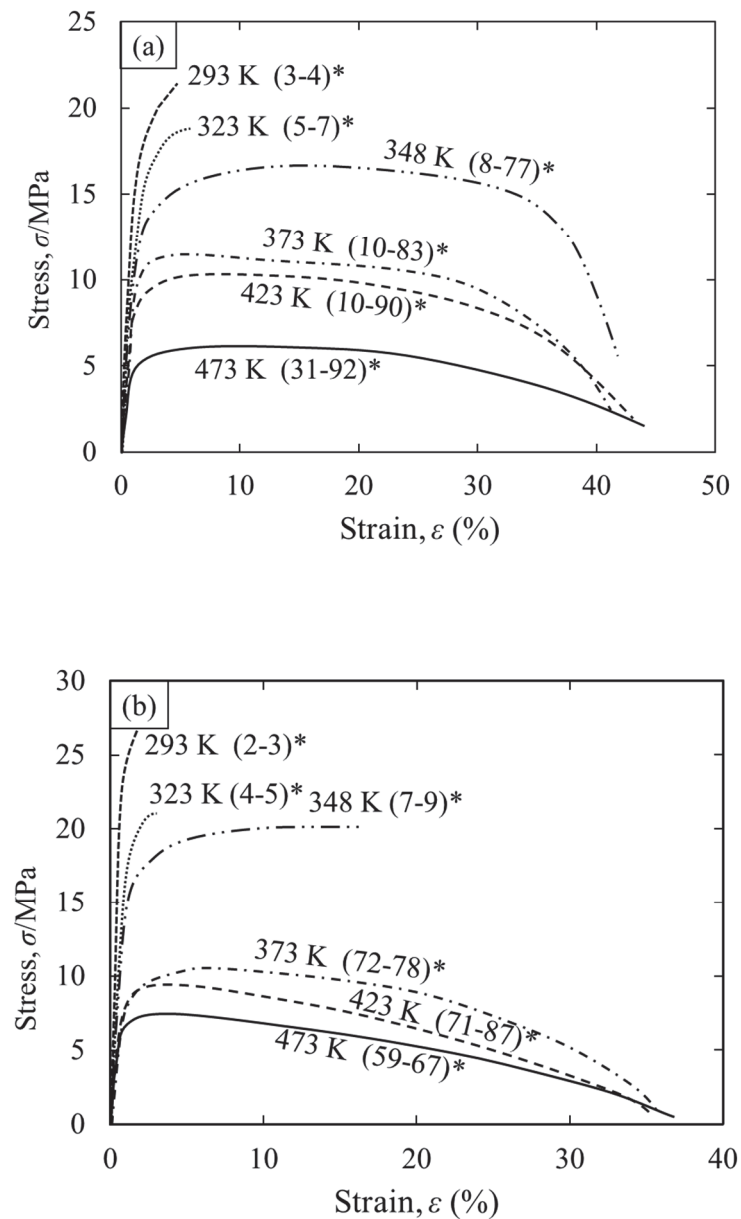
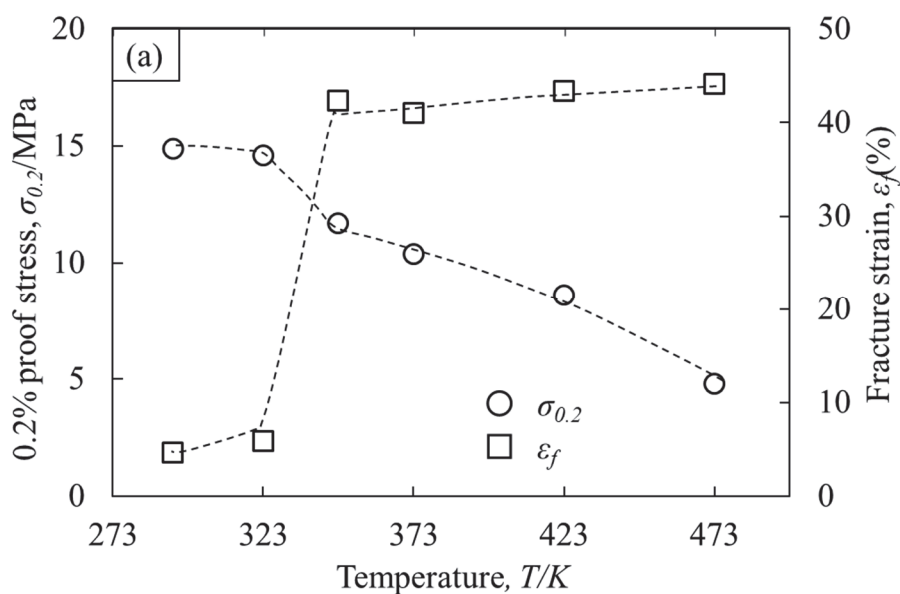


Fig. 3.12 Stress-strain curves of (a) Bi-2.0Ag-0.5Cu and (b) Bi-5.0Ag-0.5Cu at 293, 323, 348, 373, 423 and 473 K. *Range of reduction in area (%) after failure.

Both alloys showed a fracture strain of more than 17% even at 348 K. The temperature dependence of the 0.2% proof stress and fracture strain of the ternary alloys is shown in Fig. 3.13. The 0.2% proof stress decreased with an increase in the temperature. In particular, between 323 and 348 K the temperature dependence of the 0.2% proof stress was stronger than that seen between 293 and 473 K in the case of Bi-2.0Ag-0.5Cu. In contrast, the fracture strain increased sharply from 5.9 to 42.4% between 323 and 348 K; this resulted in a transition from ductility to brittleness in this temperature range. Further, the ductile-to-brittle transition occurred at approximately 348 K in the case of Bi-5.0Ag-0.5Cu. It was found that the decrease in the 0.2% proof stress was correlated to a significant increase in the fracture strain at temperatures between 323 and 373 K. Therefore, these data confirmed the ductile-to-brittle transition temperature. The Bi-2.0Ag-0.5Cu and Bi-5.0Ag-0.5Cu alloys underwent ductile fractures at 348 and 373 K, respectively, with dimples being present on the fracture surfaces. The fracture surfaces of the alloys at temperatures higher and lower than the ductile-to-brittle transition temperatures are shown in Fig. 3.14. The ductile and brittle fracture surfaces shown correspond to the deformation behaviors at temperatures higher and lower than the ductile-to-brittle transition temperatures.



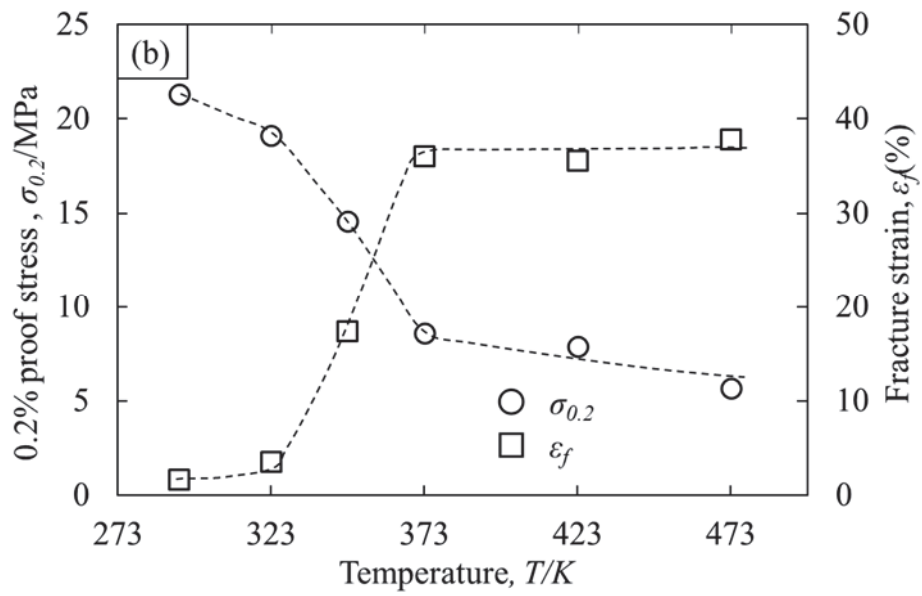
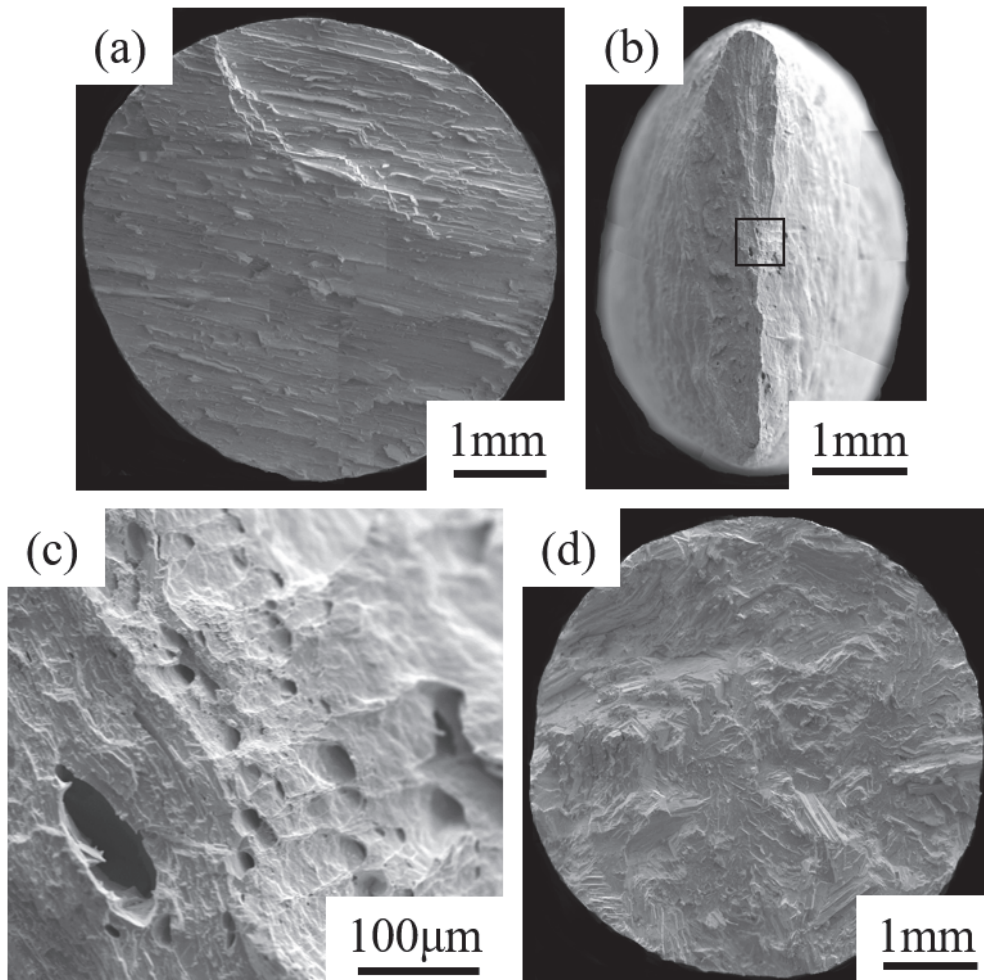


Fig. 3.13 0.2% proof stress and fracture strain at 293-473 K for (a) Bi-2.0Ag-0.5Cu and (b) Bi-5.0Ag-0.5Cu alloys.



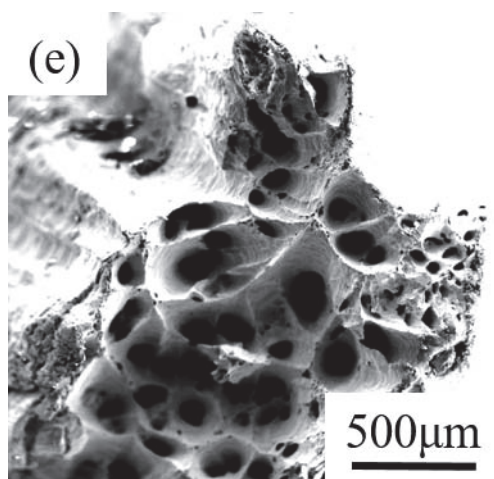


Fig. 3.14 SEM images of fracture surfaces of Bi-2.0Ag-0.5Cu specimens tensile tested at (a) 323 K and (b) 348 K, and Bi-5.0Ag-0.5Cu specimens tensile tested at (d) 348 K and (e) 373 K. High magnified image (c), corresponds to a black rectangle area of low magnification images in (b), respectively.

3.3.2.2 Relation between mechanical properties and ΔMk

The hardness values of ternary alloys were plotted in Fig. 3.15. These alloys showed higher values in hardness as the ΔMk was increased in ternary alloys. Moreover, their 0.2% proof stress, ultimate tensile strength and fracture strain were also replotted in Fig. 3.16. Each value in mechanical properties such as tension and hardness for ternary alloys agreed with their estimation lines obtained from binary alloys, mentioned above. It may be convenient in future that the prediction of mechanical properties by the ΔMk is applied to Bi system alloys with multiple components more than three elements. Actually, the Bi-2Ag-0.5Cu became to a promising alloy as one of high temperature solders which have to satisfy mechanical properties of 20 MPa-UTS and 5%-fracture strain at 293 K.

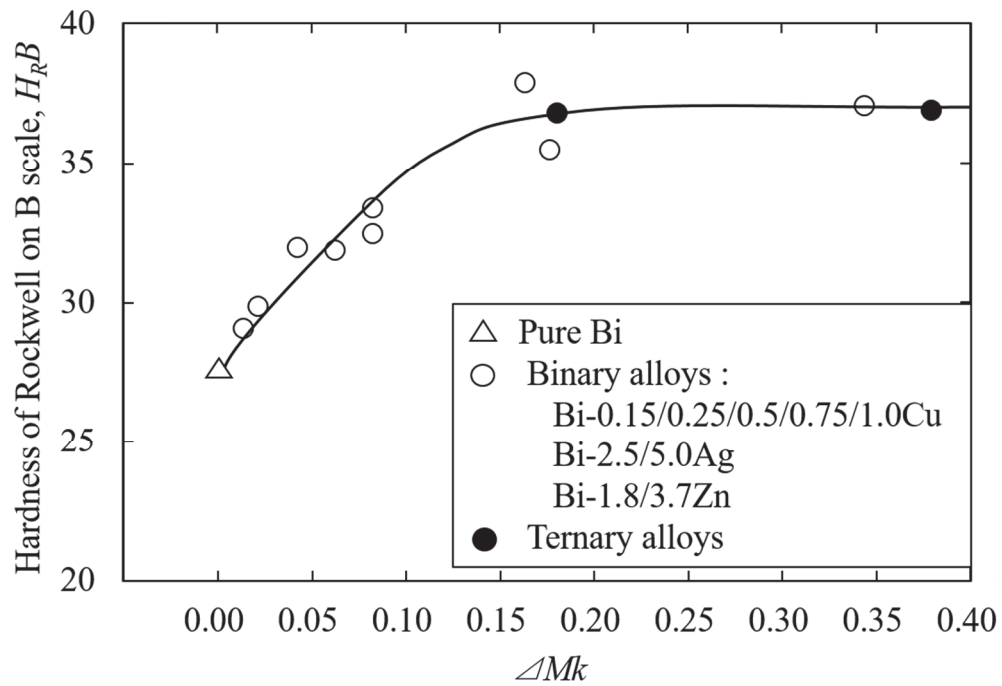


Fig. 3.15 Relation between hardness of Rockwell on B scale and ΔMk of Bi system alloys and pure Bi.

Figure 3.17 shows the relationship between the 0.2% proof stress, the ultimate tensile strength or fracture strain at 423 K and ΔMk . It is also found that the 0.2% proof stress, the ultimate tensile strength or fracture strain at 423 K could be also predicted using their estimation lines obtained from binary Bi system alloys. Moreover, this relationship at 423 K was similar to that seen at 293 K.

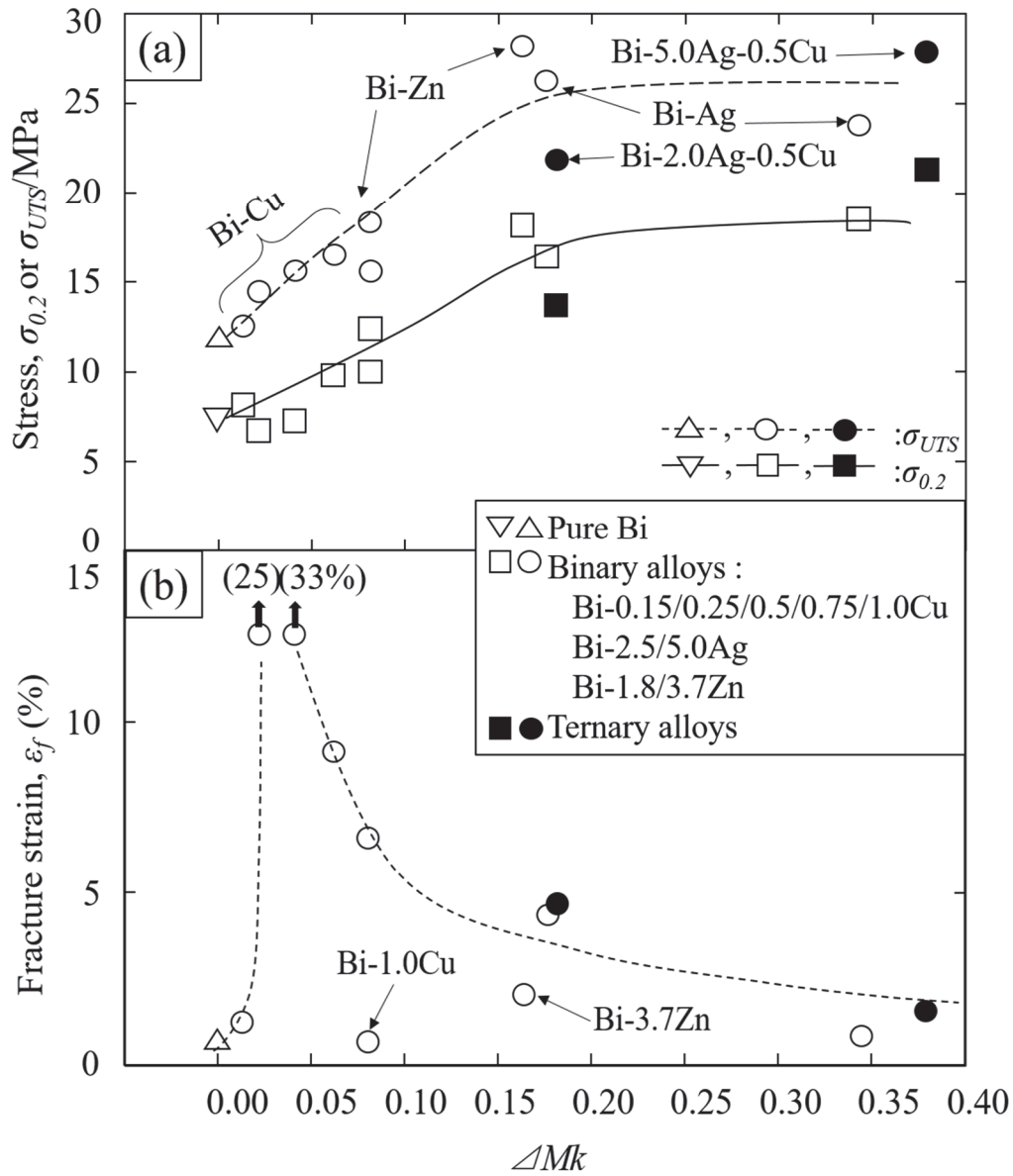


Fig. 3.16 Relation between the (a) 0.2% proof stress, ultimate tensile strength or (b) fracture strain and ΔMk of Bi system alloys at 293 K.

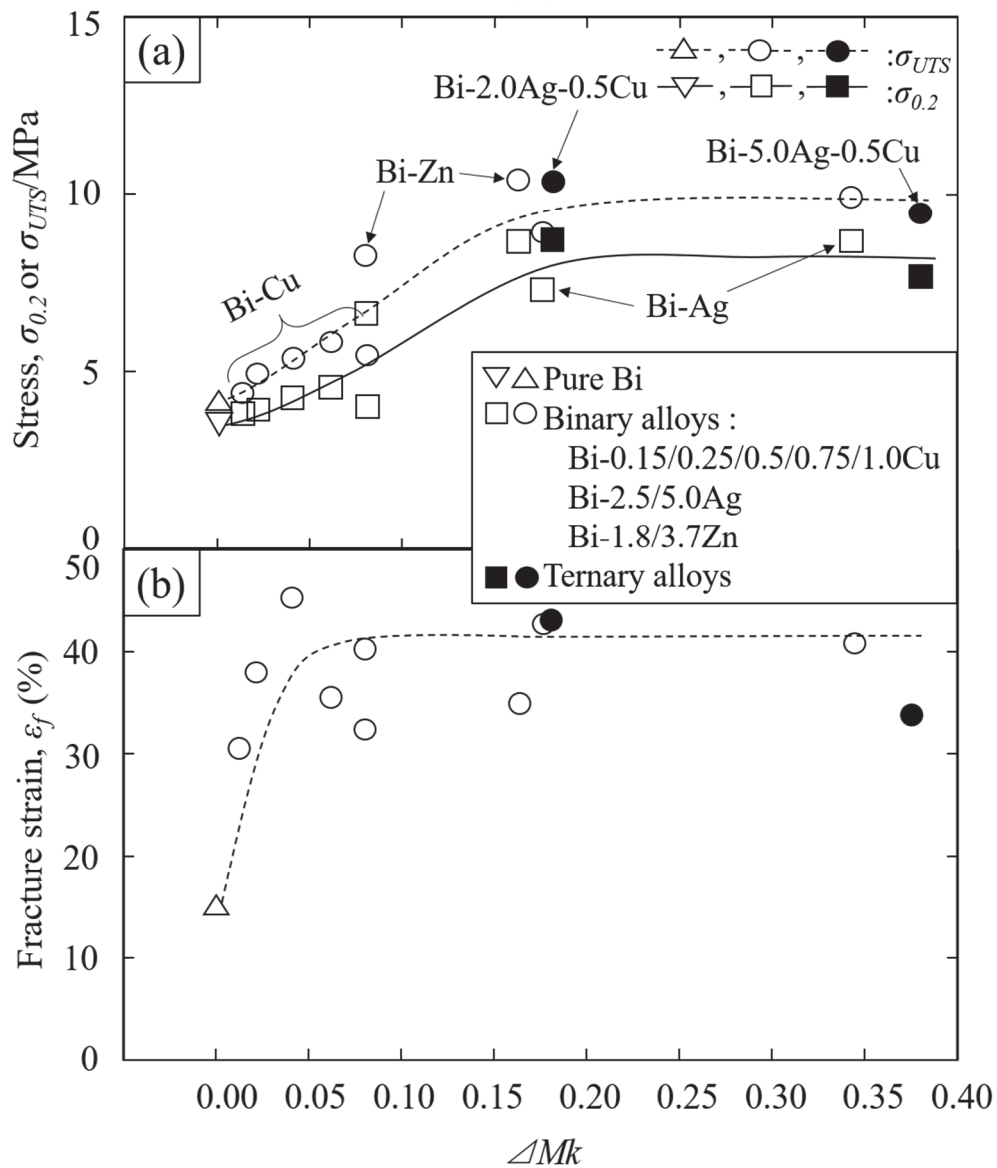


Fig. 3.17 Relation between the (a) 0.2% proof stress, ultimate tensile strength or (b) fracture strain and ΔMk of Bi system alloys at 423 K.

3.3.3 Melting points

Figure 3.18 showed the DTA heating curves of the ternary Bi system alloys. The solidus temperatures of the Bi-2Ag-0.5Cu and Bi-5.0Ag-0.5Cu alloys were 536 and 538 K, because of the eutectic structure shown in Fig. 3.9, respectively. Based on these

results, it can be surmised that the compositionally optimized Bi-Ag-Cu system alloys are suitable for use in practical applications requiring a melting point higher than 533 K¹).

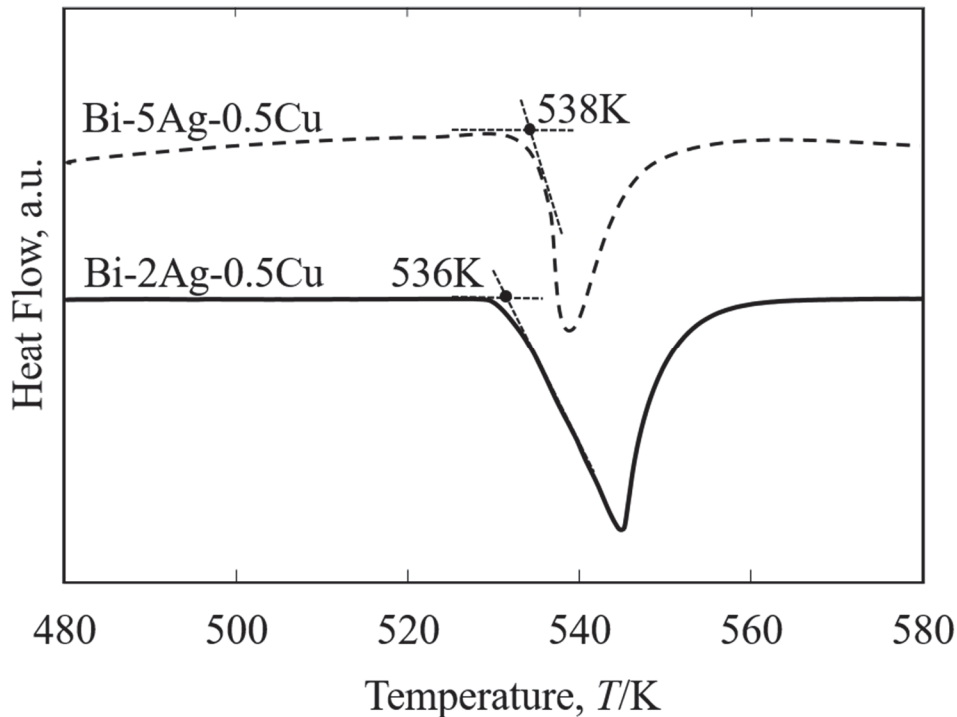


Fig. 3.18 DTA curves of Bi-2.0Ag-0.5Cu and Bi-5.0Ag-0.5Cu alloys.

3.3.4 Wettability

Figure 3.19 shows typical droplets of pure Bi, Bi-0.75Cu, Bi-2.0Ag-0.5Cu, and Bi-5.0Ag-0.5Cu on a Cu plate at 973 K in an Ar atmosphere. The contact angles for all the experimental alloys are listed in Table 3.2. It can be seen that the contact angles for all the specimens were 24~30 degree (i.e., less than 90 degree), making the alloys suitable for use in practical applications.

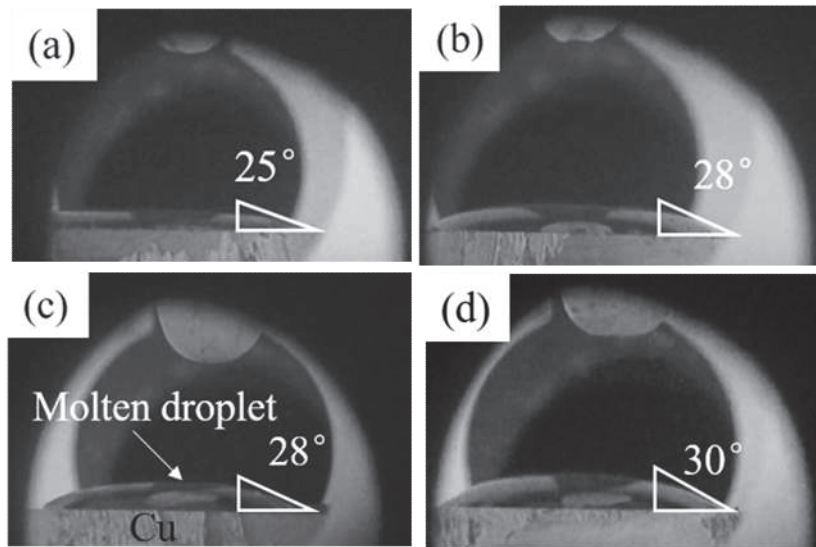


Fig. 3.19 Typical molten droplets of (a) pure Bi, (b) Bi-0.75Cu, (c) Bi-2.0Ag-0.5Cu and (d) Bi-5.0Ag-0.5Cu on Cu plate.

Table 3.2 Contact angles between droplets of experimental alloys and Cu plate as measured at 973 K in Ar atmosphere.

Alloys (mass.%)	Contact angle (degree)	Alloys (mass.%)	Contact angle (degree)
Pure Bi	25	Bi-2.5Ag	25
Bi-0.15Cu	26	Bi-5.0Ag	24
Bi-0.25Cu	27	Bi-1.8Zn	32
Bi-0.5Cu	29	Bi-3.7Zn	33
Bi-0.75Cu	28	Bi-2.0Ag-0.5Cu	28
Bi-1.0Cu	29	Bi-5.0Ag-0.5Cu	30

3.3.5 Thermal conductivity

The thermal conductivity (λ) values of the Bi-2.0Ag-0.5Cu and Bi-5.0Ag-0.5Cu alloys were measured at 293–373 K. Figure 3.20 shows the temperature and compositional dependence of λ . As can be seen from the figure, λ decreased monotonously with an increase in the temperature; this was the case regardless of the alloy composition. Bi-5.0Ag-0.5Cu showed higher λ values compared with Bi-2.0Ag-0.5Cu, because of large amount of Ag in alloys. As the temperature is increased, the movement of the electrons becomes even more chaotic, resulting in a reduction in conductivity. Moreover, the λ values of the alloys could be estimated using expressions that were functions of the temperature. For the same temperature, the λ values of the designed alloys were lower than those of the conventional Pb-5Sn alloy. However, the λ values of the ternary alloys need to be increased further in order for the alloys to be practically applicable.

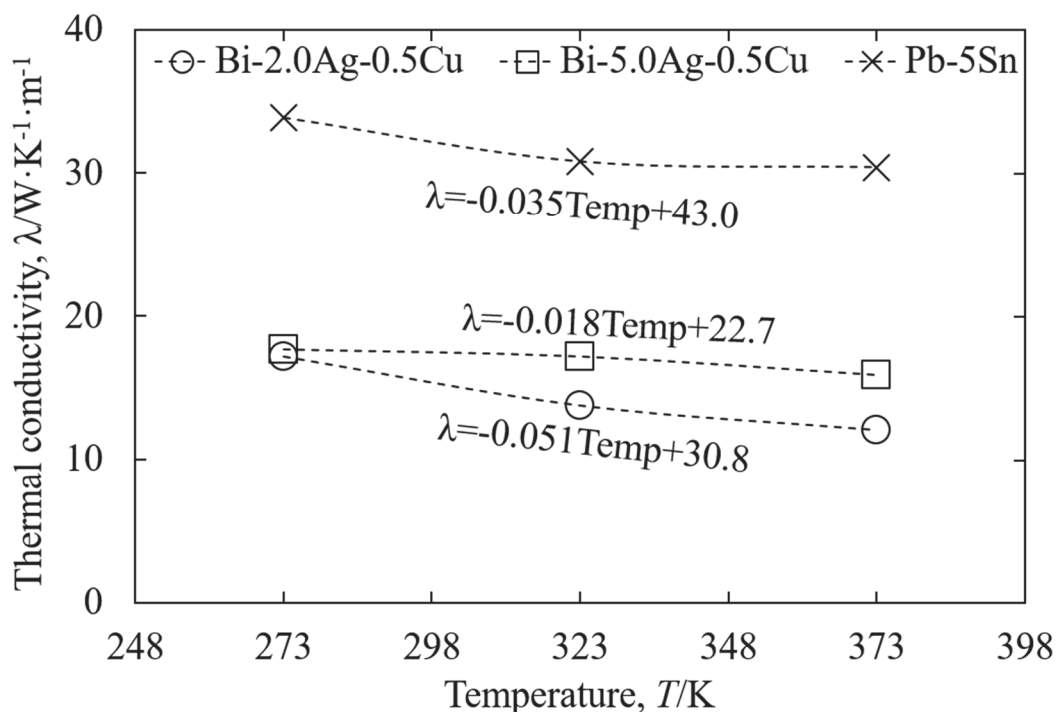


Fig. 3.20 Thermal conductivities of Bi-2.0Ag-0.5Cu, Bi-5.0Ag-0.5Cu and Pb-5Sn alloys for temperatures of 273-373 K.

3.4 Summary

(1) The proposed Bi-2.0Ag-0.5Cu and Bi-5.0Ag-0.5Cu with ΔMk of 0.180 and 0.379 as ternary alloys, respectively, showed the improved tension and hardness properties, compared with pure Bi. It is found that their ultimate tensile strength, fracture strain and hardness values could be also predicted using their estimation lines obtained from binary Bi system alloys regardless of temperature.

(2) The melting point of Bi-2.0Ag-0.5Cu and Bi-5.0Ag-0.5Cu alloys were measured to be 536 and 538 K, respectively; which resulted in the range of melting temperature of the high-temperature solder. The thermal conductivity shows lower value than Pb-5Sn. Moreover, the values in wettability to the Cu plate were satisfied for the practical application (<90 degree).

References

- 1) S. Masayoshi, Y. Tomohiro, S. Kunio, N. Hiroshi, T. Tadashi: *Trans. JWRI* **41** (2012) 51-54.
- 2) H. Schoeller, S. Bansal, A. Knobloch, D. Shaddock, J. Cho: *Mater. Sci. Eng. A* **528** (2011) 1063-1070.
- 3) G. Zeng, S. McDonald, K. Nogita: *Microelectron. Reliab.* **52** (2012) 1306-1322.
- 4) S. Sakuyama, T. Akamatsu, K. Uenishi and T. Sato: *Trans. JIEP* **2** (2009) 98-103.
- 5) C. Leinenbach, F. Valenza, D. Giuranno, H. Elsener, S. Jin, R. Novakovic: *Electron. Mater.* **40** (2011) 1533-1541.
- 6) J. Pstrus, P. Fima, T. Gancarz: *Mater. Eng. Perform.* **21** (2012) 606-613.
- 7) T. Gancarz, J. Pstrus, P. Fima, S. Mosinska: *Mater. Eng. Perform.* **21** (2012) 599-605.
- 8) S. Kim, K.S. Kim, S.S. Kim, K. Suganuma: *Electron. Mater.* **38** (2009) 266-272.
- 9) Z. Xu, Y. Choi, T. Niimi, M. Yu, S. Motozuka, K. Matsugi, K. Suetsugu: *Mater. Trans.* **57** (2016) 553-557.
- 10) J. Song, H. Chuang, Z. Wu: *Electron. Mater.* **55** (2006) 1041-1049.
- 11) J. Song, H. Chuang, T. Wen: *Metall. Mater. Trans. A* **38** (2007) 1371-1375.
- 12) C. Wang, H. Chen, P. Li: *Mater. Chem. Phys.* **136** (2012) 325-333.
- 13) C. Leinenbach, F. Valenza, D. Giuranno, H.R. Elsener, S. Jin, R. Novakovic: *Electron. Mater.* **40** (2011) 1533.
- 14) T. Iseki, M. Takamori: *J. J. Inst. Electron. Packag.* **15** (2012) 153.
- 15) J. C. Slater, *Quantum theory of molecules and solids*, Vol. 4, McGraw-Hill, New York (1974).
- 16) R. Ninomiya, *Doctoral thesis, Toyohashi University of Technology* (1996) pp.124-130.
- 17) M. Tsukada, H. Adachi and C. Satoko: *Prog. Surf. Sci.* **14** (1983) 113.

- 18) M. Morinaga and N. Yukawa: *Computer Aided Innovation of New Materials*, ed. by M. Doyama *et al.*, (North-Holland, 1991) pp. 803-808.
- 19) M. Morinaga, N. Yukawa and H. Adachi: *Tetsu-to-Hagane* **72** (1986) 555-562.
- 20) M. Morinaga, N. Yukawa, H. Adachi and H. Ezaki: *Superalloys* 1984, (The Metallurgical Society of AIME, Warrendale, PA, 1984) pp. 523-532.
- 21) K. Matsugi, S. Yamamura, Z. F. Xu, Y. B. Choi, K. Sugio, G. Sasaki and N. Oda: *Mater. Trans.* **56** (2015) 1675-1682.
- 22) 株式会社日立ハイテクサイエンス：示差熱分析 (DTA) の解説
<http://www.hitachihightech.com/hhs/products/tech/ana/thermal/descriptions/dta.html>
- 23) 金属の熱伝導率の一覧表 - ダイヤモンドホイール
<http://www.toishi.info/metal/k.html>
- 24) E. A. Eid, A. N. Fouda, E. M. Duraia: *Mater. Sci. Eng. A* **657** (2016) 104-114.

Chapter 4

Practical applications of high temperature solders

4.1 Introduction	86
4.2 Experimental procedure	88
4.2.1 Materials and manufacturing process	88
4.2.2 Evaluation of some properties	88
4.3 Results and discussion	92
4.3.1 Heat cycle behaviors	92
4.3.1.1 Comparison of Bi system alloy and practically used alloys in heat cycle measurements	92
4.3.1.2 Microstructures of solder/Cu diffusion couples	99
4.3.1.3 Growth behavior of intermetallic compounds	105
4.3.1.4 Diffusion mechanism between solder alloys and Cu	108
4.3.2 Shearing test of Bi-5.0Ag-0.5Cu and Cu substrates with Bi coating	111
4.3.3 Comparison between promising alloys and Pb-xSn alloys in view of soldering	114
4.4 Summary	116
References	117

4.1 Introduction

With the development of the electronics industry, the package form has gradually developed toward fine pitch and high density. Due to lead pollution to the environment, the packaging material also changed from the original lead contained alloy to the lead-free solder alloys¹⁾. Solder joints play a role of both mechanical and electrical connection in the package. With the development of miniaturization and multi-functionalization of electronic products, the density of electronic packaging continues to increase. The size of solder joints is getting smaller and smaller, and the electrical, mechanical, and thermal loads on them are getting higher and higher²⁻⁵⁾. Failure of one solder joint may lead to failure of the entire component. This puts higher requirements on the performance of the joint to ensure reliable operation of the electronic system. Statistics show that, among all the failure causes of electronic devices or electronic machines, about 70% of them are caused by joint failure⁶⁾. However, in most cases, the reliability of the electronic system is not caused by the failure of the electronic device function, but by the mechanical failure of the solder joints^{7, 8)}.

The failure of solder joints is often caused by the grown of the intermetallic compound (IMC) layer. When the solder is in contact with the plating metal, an interface reaction takes place, and an IMC having a certain thickness is generated depending on the solder and the plating metal. It is a sign of reliable solder joints. However, during the service of the package structure, temperature changes may occur due to power cycle or changes in the external environment. Under the effect of temperature, the thickness of IMC layer will grow, and the mismatch of the thermal expansion coefficients of the various parts of the package structure will generate thermal stress, which will degrade the connection reliability⁹⁻¹³⁾. Moreover, some researchers reported that the strength of solder joints decreases as the thickness of the IMC layer increases, and the IMC interface is considered to be the starting point for microcracks¹⁴⁻¹⁶⁾. Therefore, the existence of the IMC layer has a great influence on the failure of solder joints.

H. T. Lee et al. studied the effect of IMC on the fracture path of solder joints, when the thickness of IMC is less than 1 μ m, the fracture path extends along the solder; when

the thickness of IMC is less than 10 μm , the fracture path is between the solder and the IMC; when the IMC thickness is more than 10 μm , the fracture path extends along the IMC¹⁷⁾. Guo et al. reported that the thickness and shape of the Cu_6Sn_5 IMC in the solder joint interface area have a great influence on the reliability of the solder joint, especially when a very thick reaction layer is formed, the difference in coefficient of thermal expansion between Cu_6Sn_5 , the substrate and the solder is large and cracks are easily generated¹⁸⁾.

In this study, the reliability for promising composition of Bi system alloy were investigated. The reliability for the solder joints of Bi-5.0Ag-0.5Cu with Bi coating substrate and Bi-5.0Ag-0.5Cu, Sn-3.0Ag-0.5Cu and Pb-20Sn with Sn coating substrate after heat cycle were compared. Then, the diffusion mechanism of these 4 couples were also measured to evaluate the failure of solder joints. The shearing test of Bi-5.0Ag-0.5Cu and Cu substrate with Bi coating was measured at last.

4.2 Experimental procedure

4.2.1 Materials and manufacturing process

The melt equipment and the casting mold were same with chapter 2. Stick-like Bi (purity of 99.99%), granular Ag (purity of 99.99%), laminar Cu (purity of 99.9%), granular Sn (purity of 99.99%), and laminar Pb (purity of 99.9%) were placed in a graphite crucible, which was then set in an electric furnace in air. The diameters of the Bi, Ag and Sn samples were 2–3 mm, while the thickness of the Cu and Pb sample was 1 mm. Once all the starting materials had melted, the melt was mixed with a ceramic stick at 773 K and held at this temperature for 1.8 ks. Next, the melt was poured into a casting mold heated to 773 K. The resulting ingot which had a diameter of 15 mm and height of 115 mm, was air cooled to 293 K.

4.2.2 Evaluation of some properties

Microstructural observation of these samples by the SEM and quantitative analyses of elements were conducted by the electron probe micro-analyzer (EPMA; JEOL JXA-8200, Japan).

Heat cycle test was used to determine the reliability of the high-temperature solder alloys. Figure 4.1 (a) shows the external view of the substrate for heat cycle test, and the points on the substrate was numbered as shown in Fig. 4.1 (b). After soldering the experimental alloy weighed to 10 - 30 mg at each position, heat cycle from 0 to 1000 was applied by a gas phase heat shock test apparatus (ES-56L, Hitachi Appliances). Figure 4.2 shows profiles of temperature for heat cycle test. The heat cycle test was performed in the temperature range of 223 K to 423 K. For one cycle time, the test time at 223 K, 293 K and 423 K were 1.8 ks, 300 s and 1.8 ks, respectively. Moreover, the recovery time for the test temperature reach 223 K and 423 K should be less than 300 s. The heat cycle test was also carried out for Sn - Ag - Cu alloys and Pb - Sn alloys for high temperature which are generally used for lead-free solders as comparative alloys. In general, Sn coating is used in order to improve wettability with the substrate, but in order to observe the superiority of Bi coating, the heat cycle test were carried out with

Bi system alloy on both Sn and Bi coating. The experimental conditions are shown in Table 4.1.

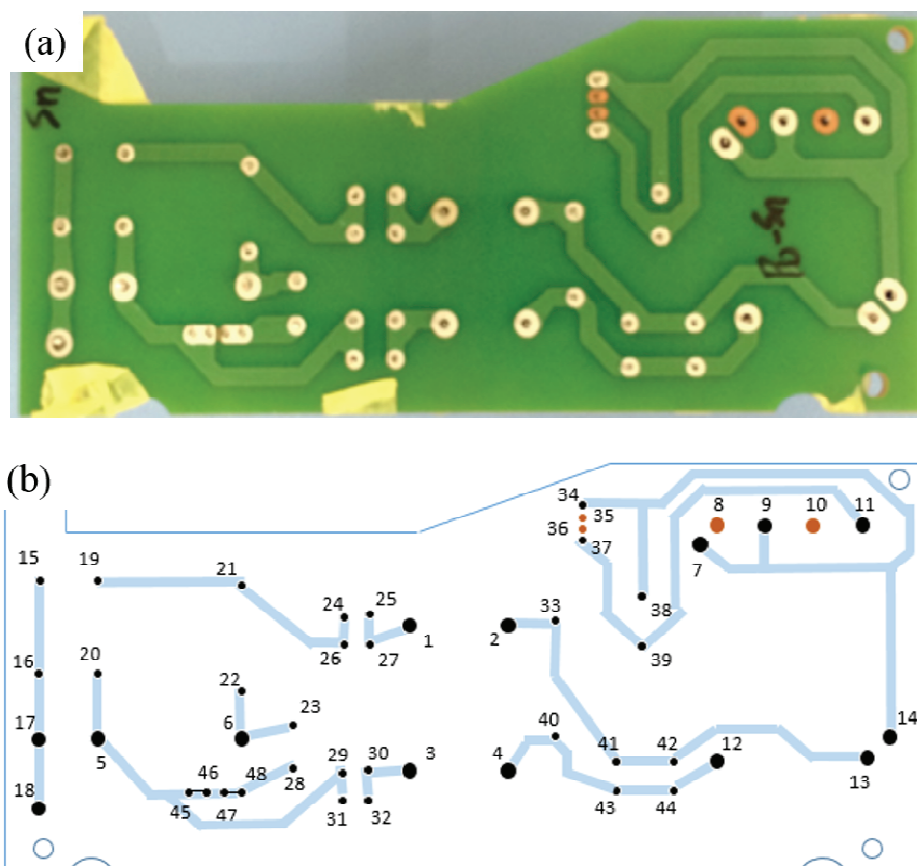


Fig. 4.1 (a) An apparatus and (b) a schematic diagram showing current path of practical substrate for heat cycle tests.

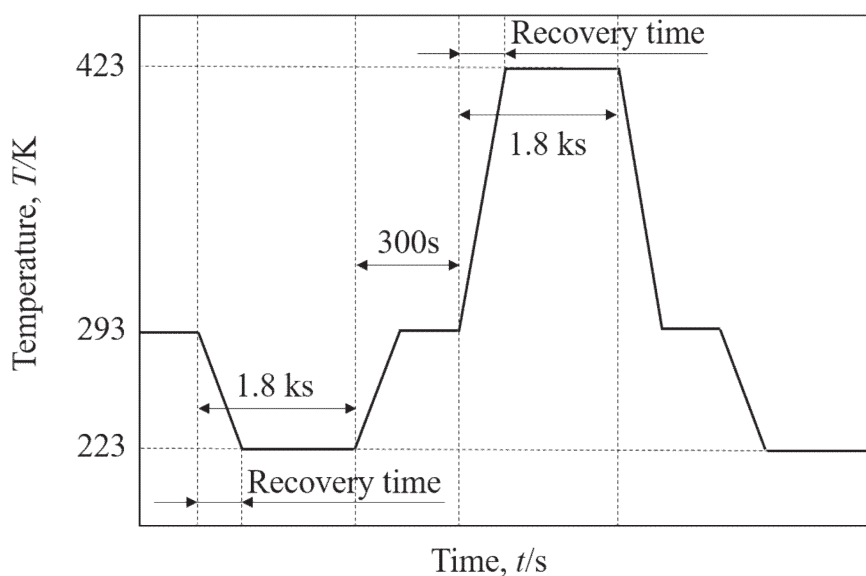


Fig. 4.2 Profile of time vs temperature for heat cycle test.

Table 4.1 Some test conditions for heat cycle tests.

Experimentally solder alloys (mass.%)	Surface treatment of substrate	Temperature range (K)
Bi-5.0Ag-0.5Cu	Bi coating	223~423
Sn-3.0Ag-0.5Cu	Sn coating	
Pb-20Sn		

Diffusion couples were prepared to observe the reaction on the interface between the solder and substrates with coating layers. A schematic diagram of diffusion couple is shown in Fig. 4.3. The Sn and Bi coating treatments were performed with, which is same with heat cycle tests. And the Cu substrate was further plated to a thickness of 75 μm to form the diffusion couple. Experimental samples and temperature ranges were made in the same manner as in the heat cycle test described above, polishing was performed in the direction perpendicular to the coating surface of the sample after 0, 100, 200, 300 and 400 cycles, and the reaction at the interface was observed using EPMA.

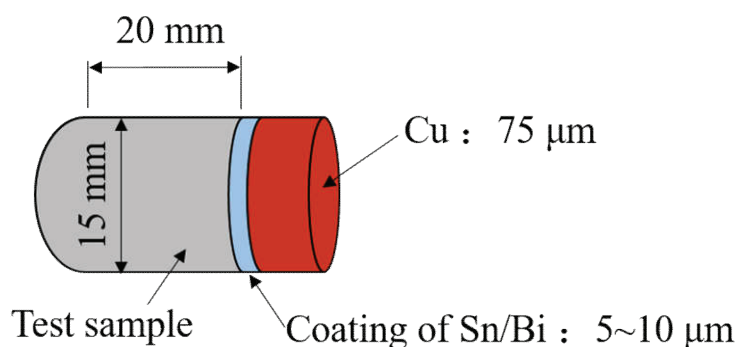


Fig. 4.3 A schematic diagram of diffusion couple.

The combination of Bi-5.0Ag-0.5Cu and Cu substrate with Bi coating were used to measure the shearing test. Figure 4.4 shows the schematic assembly of the Cu substrate used for the shearing test of this study. Shearing test was carried out using two Cu substrates shown in Fig. 4.4. Figure 4.5 shows a schematic diagram of the bonding of the Cu substrate and Bi alloy for this test. The melting alloy melted in the indentation of the Cu substrate to bond the Cu plate. The surface (a) in Fig. 4.5 is the surface coated with release agent and the surface (b) is the surface on which the Cu substrate and the Bi type alloy are soldered without applying the release agent. This shearing test pieces were performed in air by using a mechanical testing machine (Autograph DCS-R-5000, Shimadzu Corporation, Japan) with a cross-head speed of $0.5\text{mm}\cdot\text{min}^{-1}$ at 293 K.

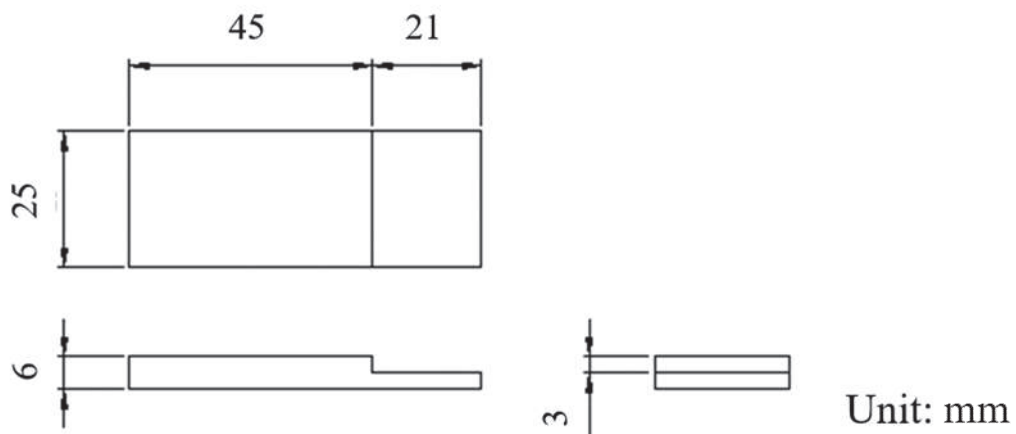


Fig.4.4 Schematic diagrams of Cu substrate in shearing strength test.

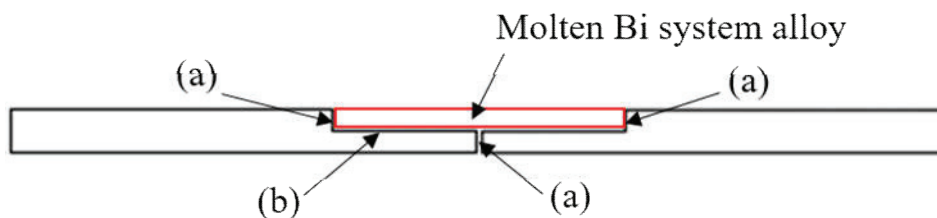


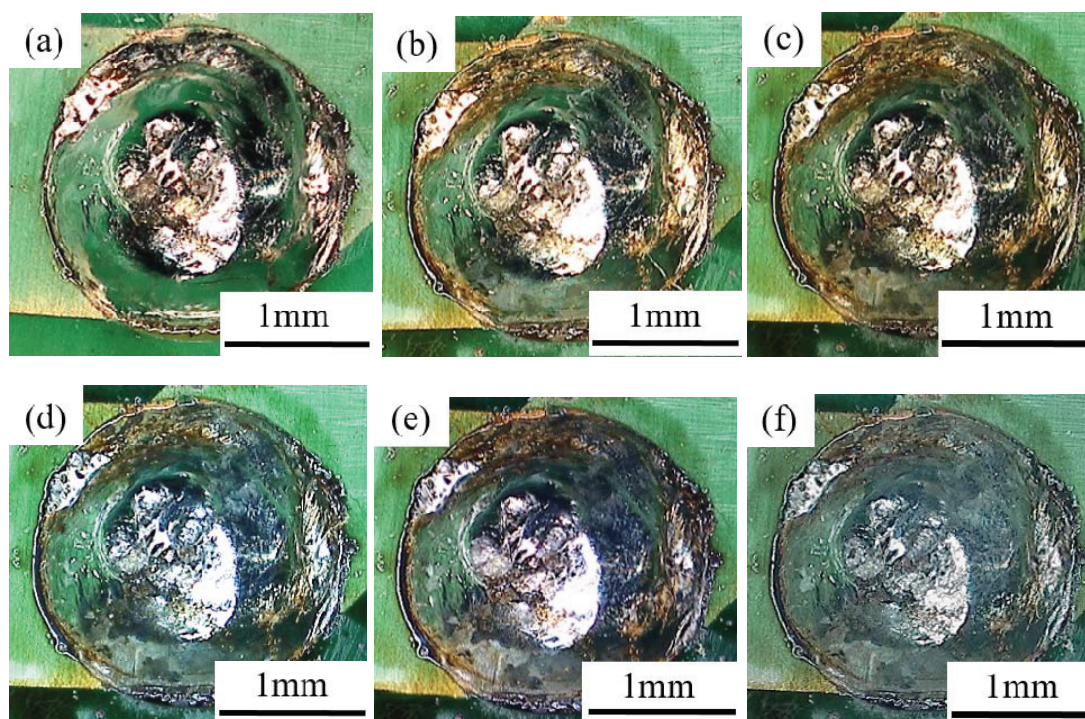
Fig. 4.5 Schematic representation of a method for soldering Cu substrate and Bi system alloy.

4.3 Results and discussion

4.3.1 Heat cycle behaviors

4.3.1.1 Comparison of Bi system alloy and practically used alloys in heat cycle measurements

The stereo microscopic images of Bi-5.0Ag-0.5Cu with Bi and Sn coating, Sn-3.0Ag-0.5Cu and Pb-20Sn with Sn coating after 0, 50, 100, 200, 300, 400, 500, 600, 700, 800, 900 and 1000 heat cycles are shown in Figs. 4.6 to 4.9, respectively. The observation place on these substrates were observed with the No. 42 in Fig. 4.1 (b) as an example for all the solder joints. Figure 4.6 shows no crack occurred until 600 cycles for Bi-5.0Ag-0.5Cu solder joint on Bi coating. In contrast, as shown in Fig. 4.7, Fig. 4.8, Fig. 4.9, the Bi-5.0Ag-0.5Cu solder joint with Sn coating, Sn-3.0Ag-0.5Cu solder joint with Sn coating, and Pb-20Sn solder joint with Sn coating appeared after 50 and 100 cycle, respectively.



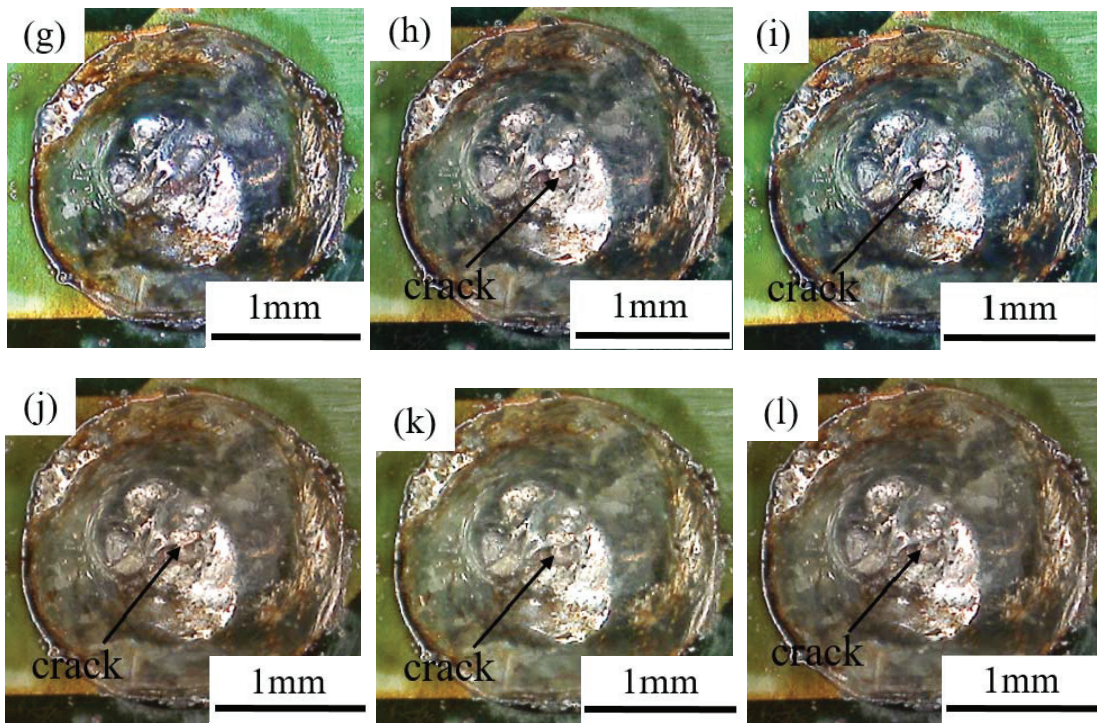
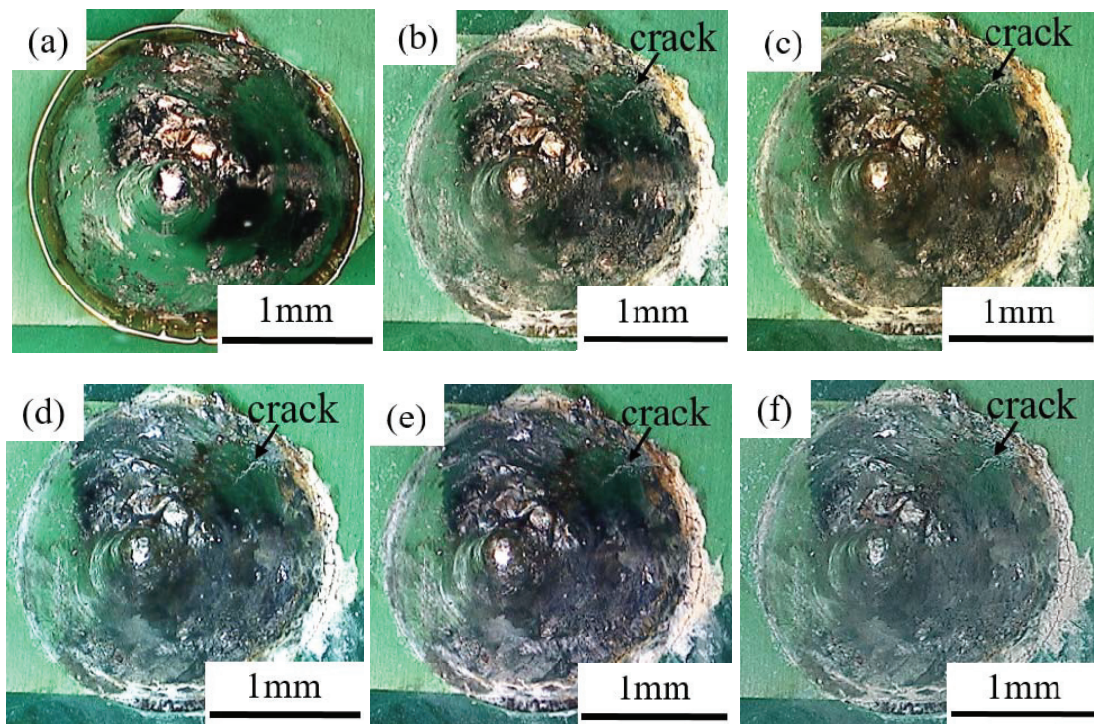


Fig. 4.6 Stereo microscope images of Bi-5.0Ag-0.5Cu with Bi coating (a) before heat cycle, (b) after 50 heat cycles, (c) after 100 heat cycles, (d) after 200 heat cycles, (e) after 300 heat cycles, (f) after 400 heat cycles, (g) after 500 heat cycles, (h) after 600 heat cycles, (i) after 700 heat cycles, (j) after 800 heat cycles, (k) after 900 heat cycles and (l) after 1000 heat cycles for No. 42 solder point in Fig. 4.1 (b).



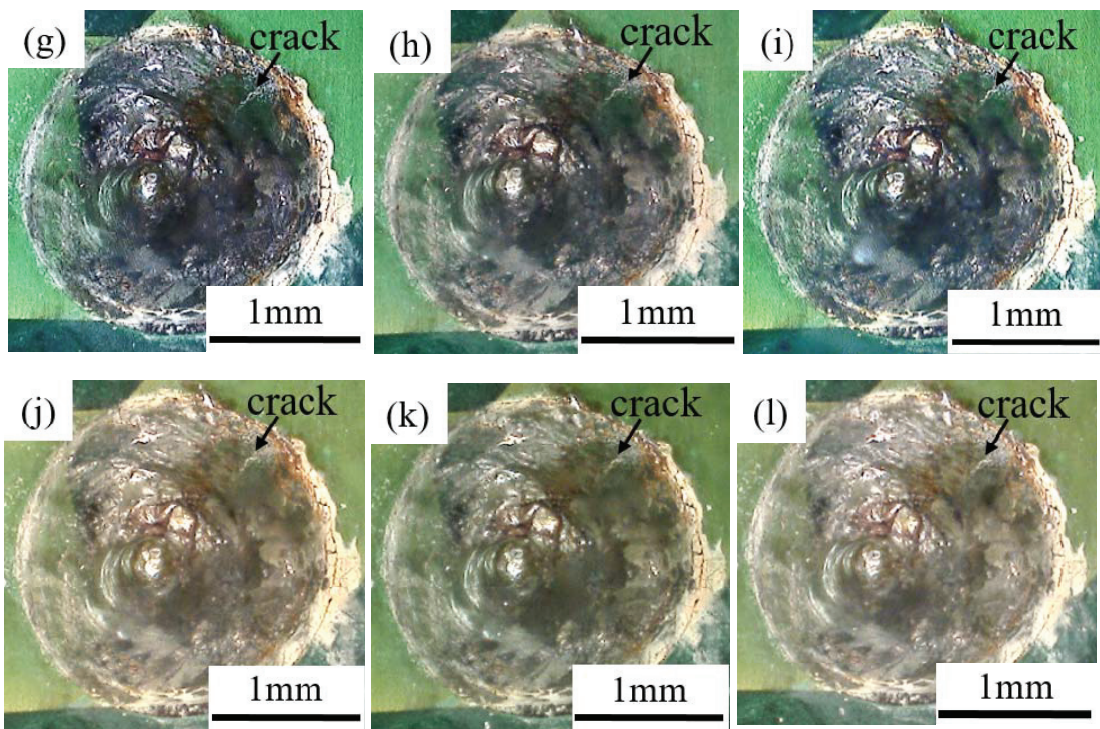
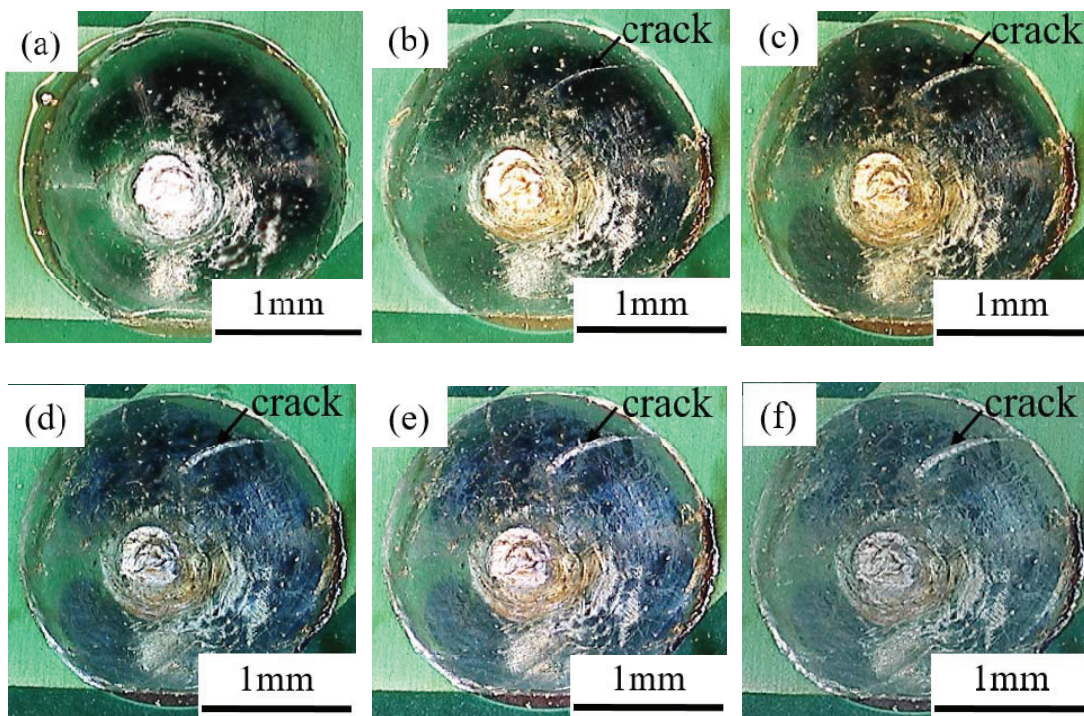


Fig. 4.7 Stereo microscope images of Bi-5.0Ag-0.5Cu with Sn coating (a) before heat cycle, (b) after 50 heat cycles, (c) after 100 heat cycles, (d) after 200 heat cycles, (e) after 300 heat cycles, (f) after 400 heat cycles, (g) after 500 heat cycles, (h) after 600 heat cycles, (i) after 700 heat cycles, (j) after 800 heat cycles, (k) after 900 heat cycles and (l) after 1000 heat cycles for No. 42 solder point in Fig. 4.1 (b).



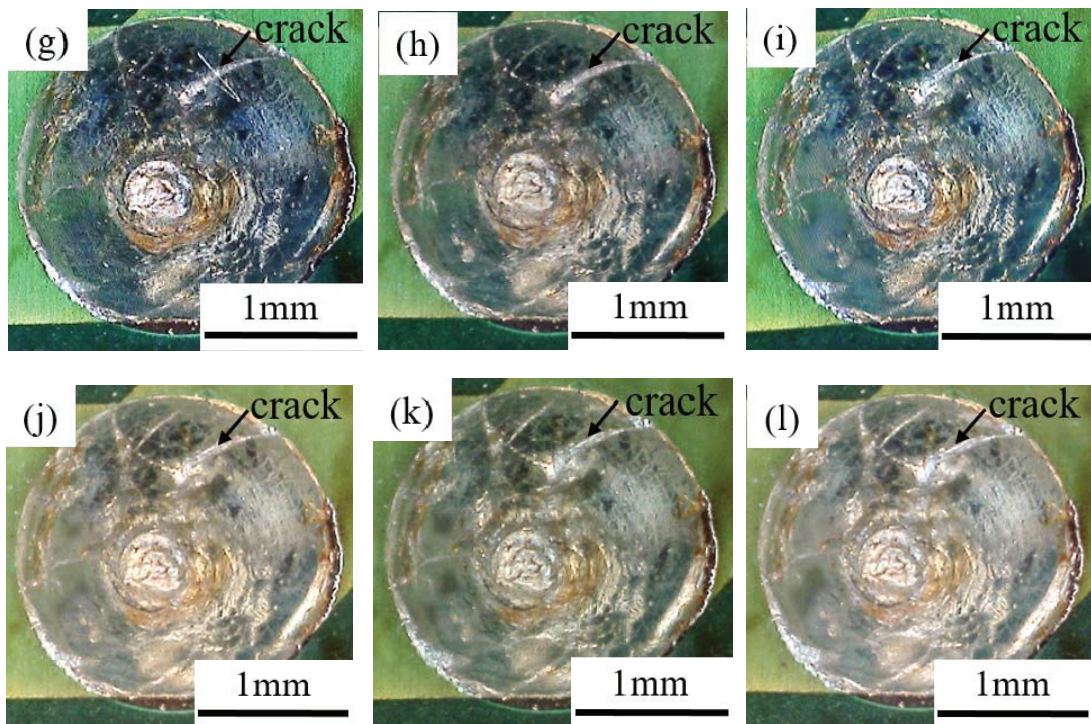
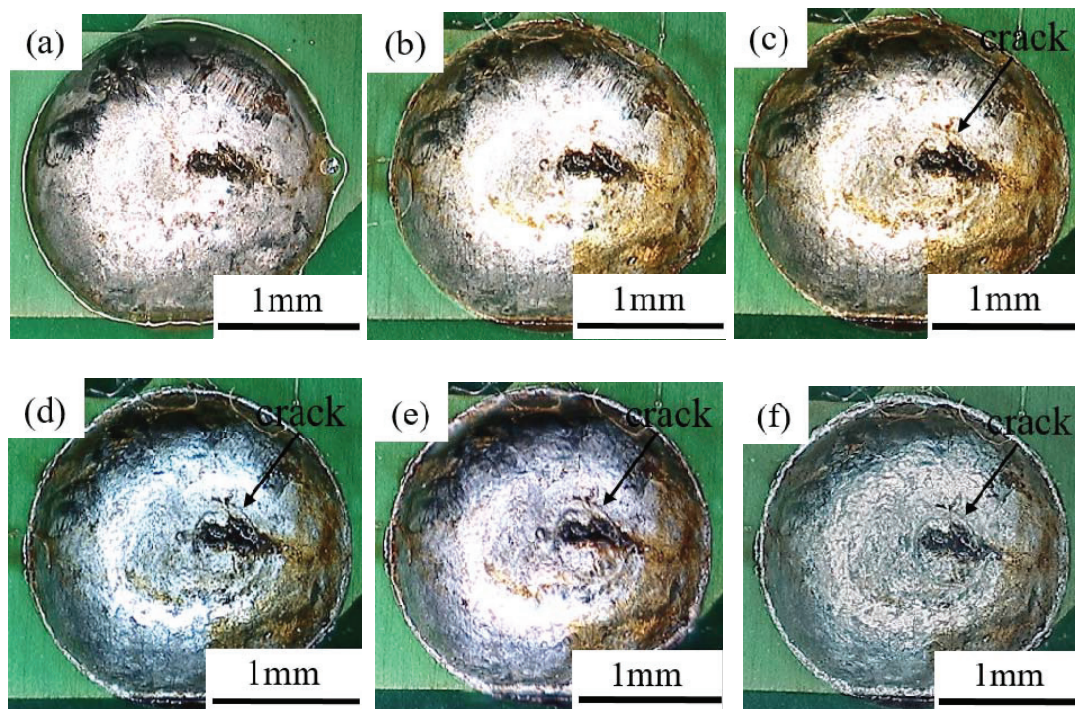


Fig. 4.8 Stereo microscope images of Sn-3.0Ag-0.5Cu with Sn coating (a) before heat cycle, (b) after 50 heat cycles, (c) after 100 heat cycles, (d) after 200 heat cycles, (e) after 300 heat cycles, (f) after 400 heat cycles, (g) after 500 heat cycles, (h) after 600 heat cycles, (i) after 700 heat cycles, (j) after 800 heat cycles and, (k) after 900 heat cycles and (l) after 1000 heat cycles for No. 42 solder point in Fig. 4.1 (b).



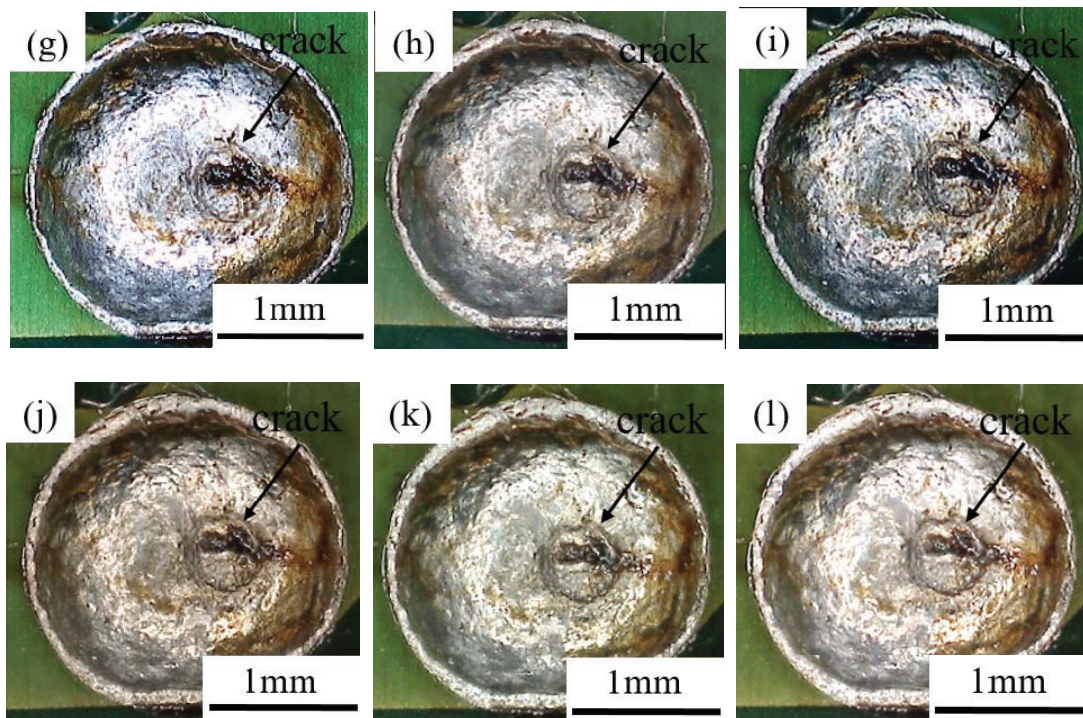


Fig. 4.9 Stereo microscope images of Pb-20Sn with Sn coating (a) before heat cycle, (b) after 50 heat cycles, (c) after 100 heat cycles, (d) after 200 heat cycles, (e) after 300 heat cycles, (f) after 400 heat cycles, (g) after 500 heat cycles, (h) after 600 heat cycles, (i) after 700 heat cycles, (j) after 800 heat cycles and, (k) after 900 heat cycles and (l) after 1000 heat cycles for No. 42 solder point in Fig. 4.1 (b).

Figure 4.10 shows the relation between number of cycles and the number on the experimental solder joints. Just one crack occurs on Bi-5.0Ag-0.5Cu with Bi coating after 600 heat cycles. Moreover, for Bi-5.0Ag-0.5Cu and Pb-20Sn solder joints with Sn coating, the number of crack were not grown with the increasing heat cycles. However, 4 cracks appeared after 500 cycles on Sn-3.0Ag-0.5Cu solder joint with Sn coating. Bi-5.0Ag-0.5Cu and Pb-20Sn solder joints with Sn coating shows almost same status of crack during the heat cycles.

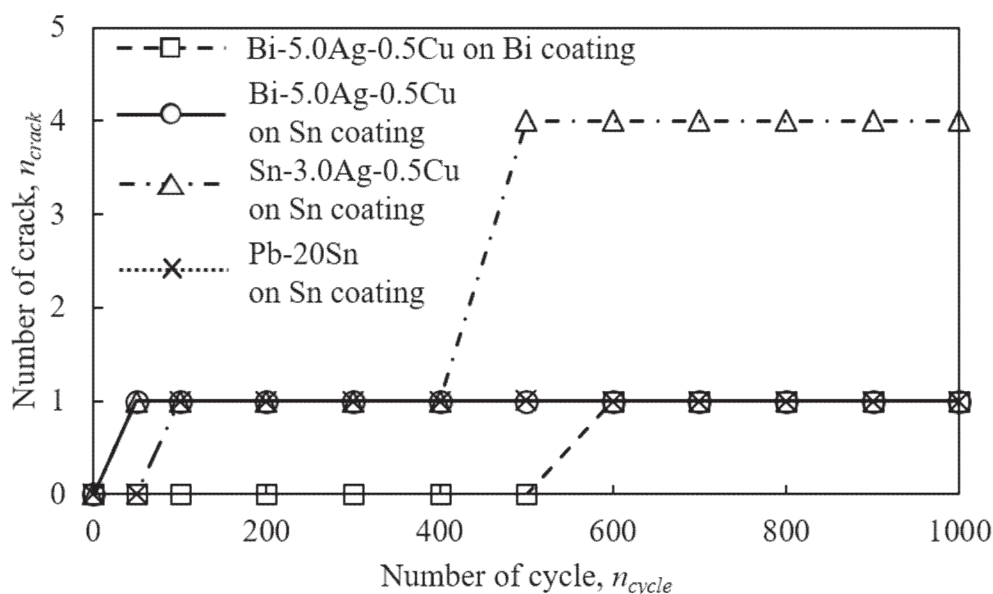


Fig. 4.10 Relation between cycle time and the number of crack for each alloy on No.42 solder point in Fig. 4.1 (b).

The relation between width or length in crack and heat cycles of Bi-5.0Ag-0.5Cu and Sn-3.0Ag-0.5Cu with Sn coating for No. 42 solder point in Fig. 4.1 (b) are shown in Fig. 4.11 (a) and (b), respectively. It should be noted that the width and length in crack of for Bi-5.0Ag-0.5Cu with Sn coating remain constant with the cycle time. In comparison, although the length in crack of Sn-3.0Ag-0.5Cu on Sn coating is also constant with increasing cycle time, the width increased with an increase in cycle time till 500 cycle. Table 4.2 lists the rate of crack occurrence for heat cycle test after 1000 cycles for all the solder points shown in Fig. 4.1. R_c is the rate of crack occurrence, which can be expressed by:

$$R_c = N_c/N \quad (3-2)$$

where, N_c is the number of observed points of cracks and N is the number of soldering points. It can be seen that Bi-5.0Ag-0.5Cu with Bi coating shows lowest rate of crack occurrence, which means the best thermal fatigue resistance for these 4 conditions.

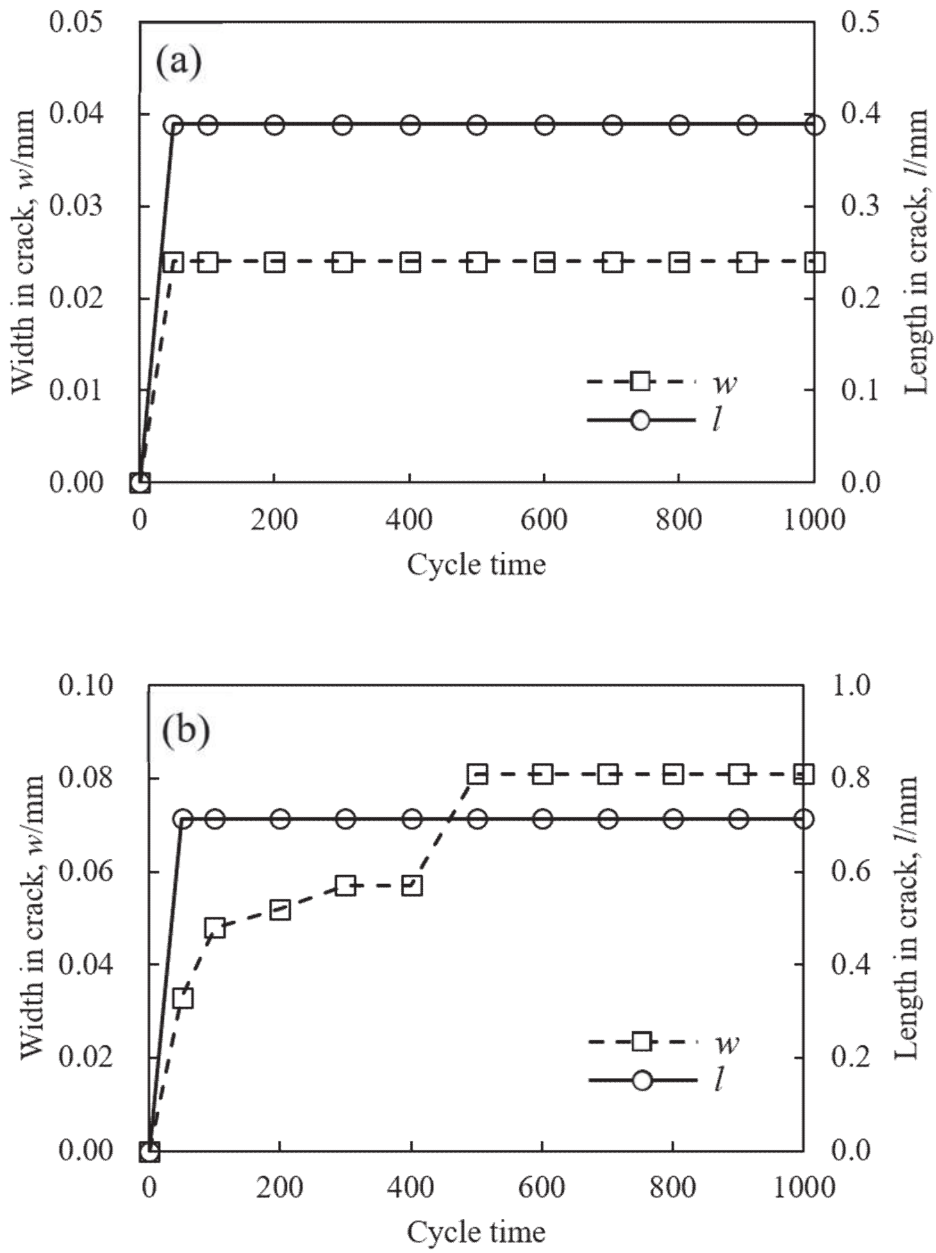


Fig. 4.11 Relation between width or length in crack and cycle time for (a) Bi-5.0Ag-0.5Cu with Sn coating and (b) Sn-3.0Ag-0.5Cu with Sn coating for No. 42 solder point in Fig. 4.1 (b).

Table 4.2 The rate of crack occurrence for heat cycle test after 1000 cycles.

Experimental alloys (mass.%)	Coating materials of Cu substrate	Rc (%)
Bi-5.0Ag-0.5Cu	Bi	26.1
	Sn	50.0
Sn-3.0Ag-0.5Cu		73.8
Pb-20Sn		46.3

4.3.1.2 Microstructures of solder/Cu diffusion couples

The compositional images and EPMA mappings near the interfaces of Bi-5.0Ag-0.5Cu with Bi coating, Bi-5.0Ag-0.5Cu with Sn coating, Sn-3.0Ag-0.5Cu with Sn coating and Pb-20Sn with Sn coating on Cu substrate for 0, 100, 200, 300 and 400 heat cycles are shown in Figs. 4.12 to 4.15, respectively. Figure 4.12 shows no intermetallic compounds (IMC) occurred between Bi-5.0Ag-0.5Cu solder alloy, Bi coating and Cu substrate. In contrast, as shown in Fig. 4.13, Fig. 4.14, Fig. 4.15, the diffusion reaction between Bi-5.0Ag-0.5Cu, Sn-3.0Ag-0.5Cu and Pb-20Sn with Sn coating and Cu substrate formed the Cu-Sn IMC layer after 100 heat cycle. Table 4.3 lists the composition of this IMC, which identified as a result of quantitative analyses by EPMA. And the diffusion reaction occurs in Sn coating part.

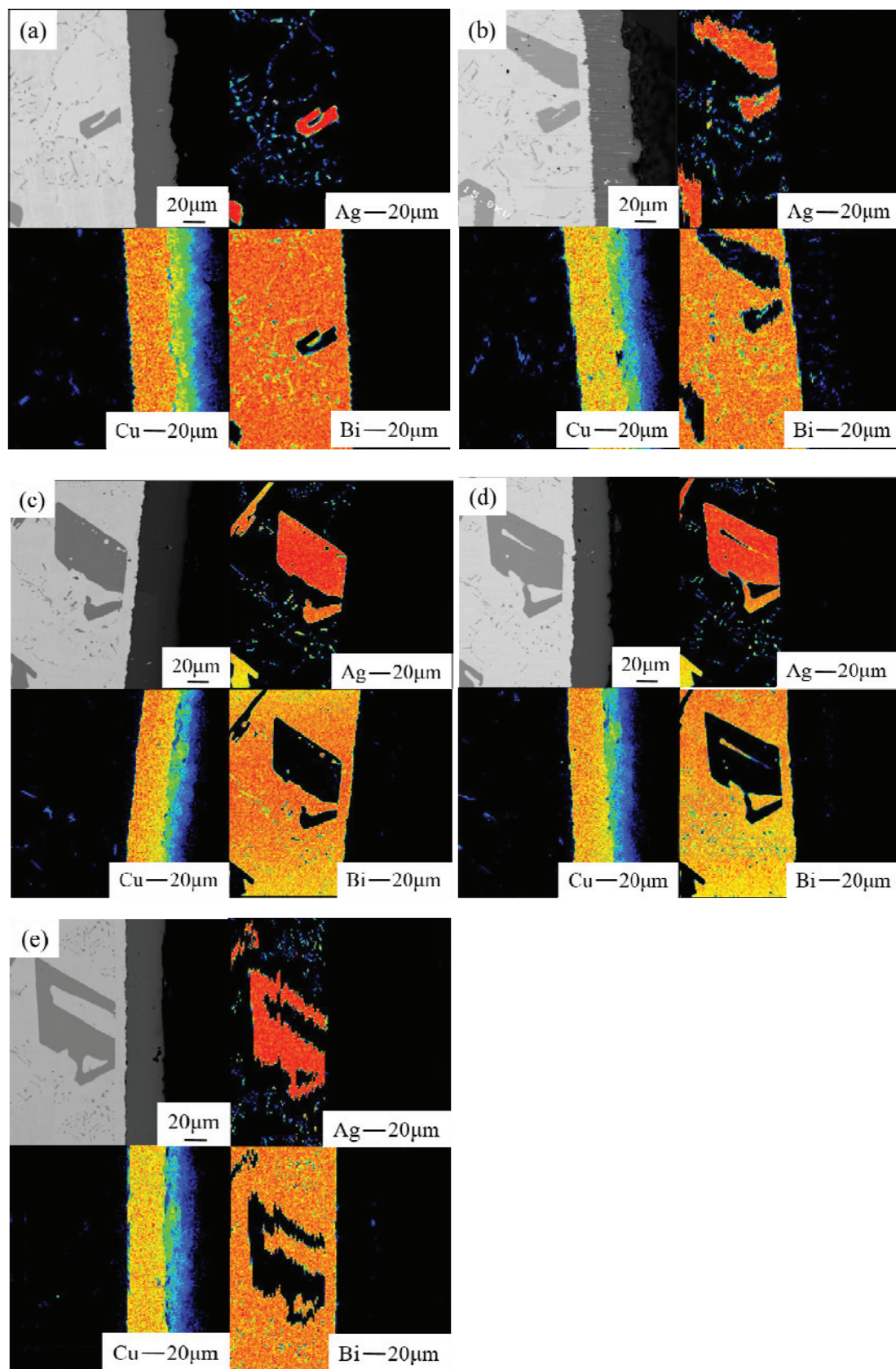
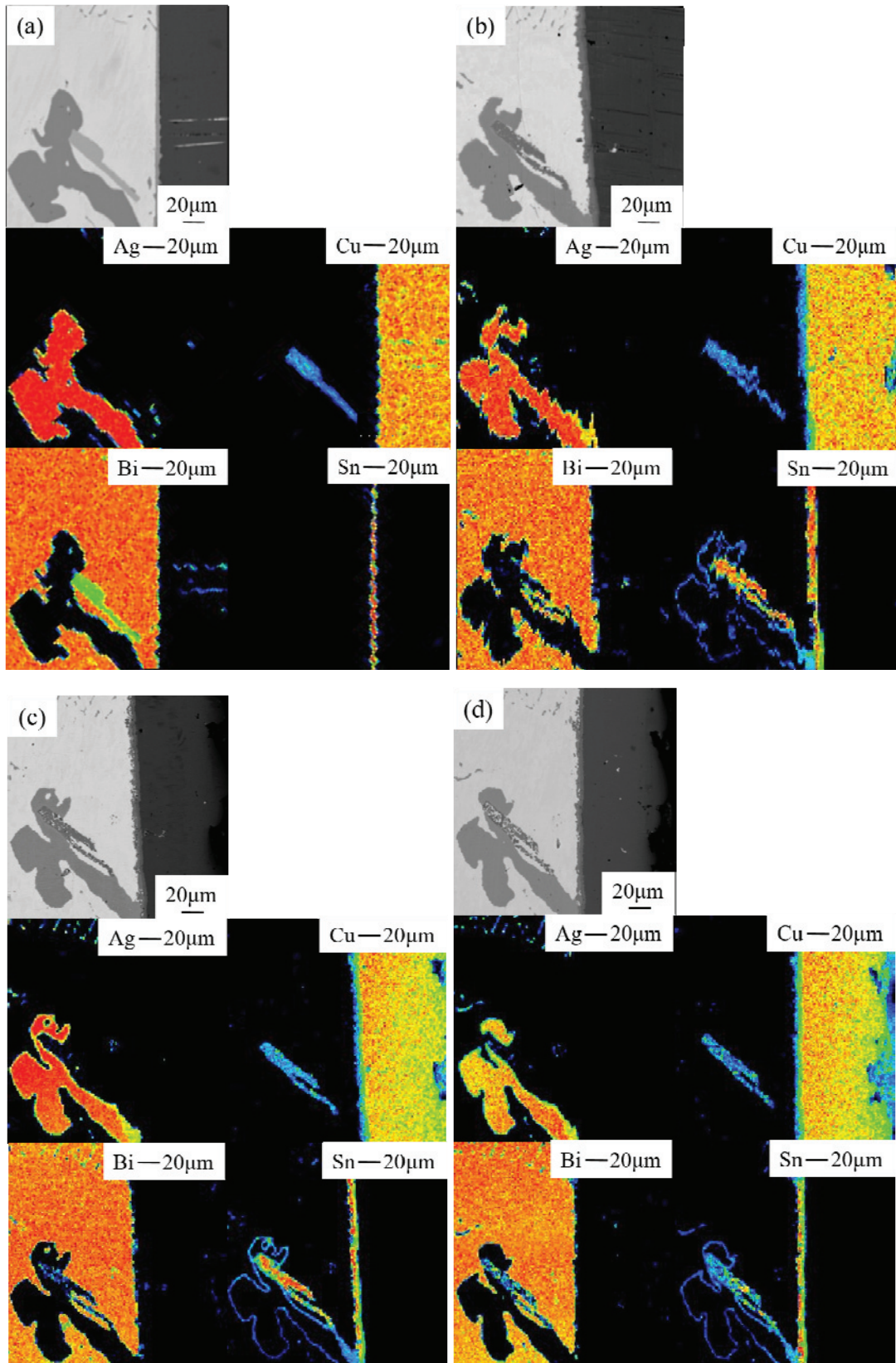


Fig. 4.12 Compositional images and EPMA mappings of Bi-5.0Ag-0.5Cu with Bi coating after (a) 0, (b) 100, (c) 200, (d) 300 and (e) 400 heat cycles.



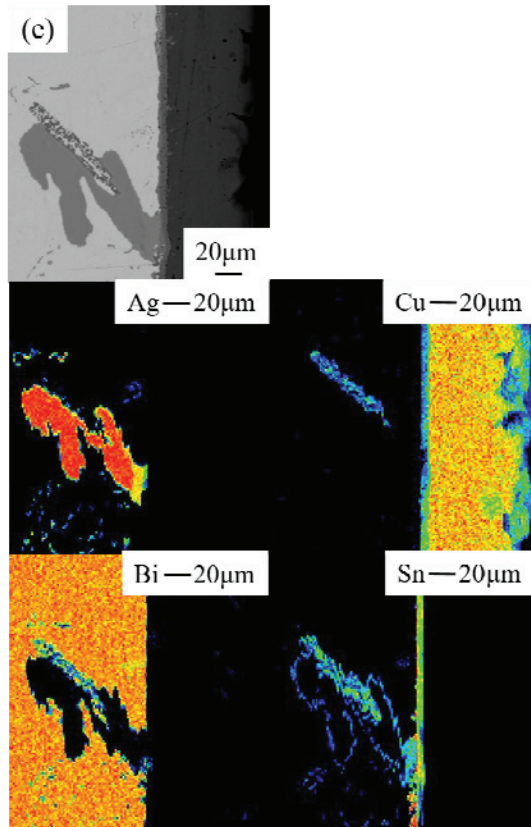


Fig. 4.13 Compositional images and EPMA mappings of Bi-5.0Ag-0.5Cu with Sn coating after (a) 0, (b) 100, (c) 200, (d) 300 and (e) 400 heat cycles.

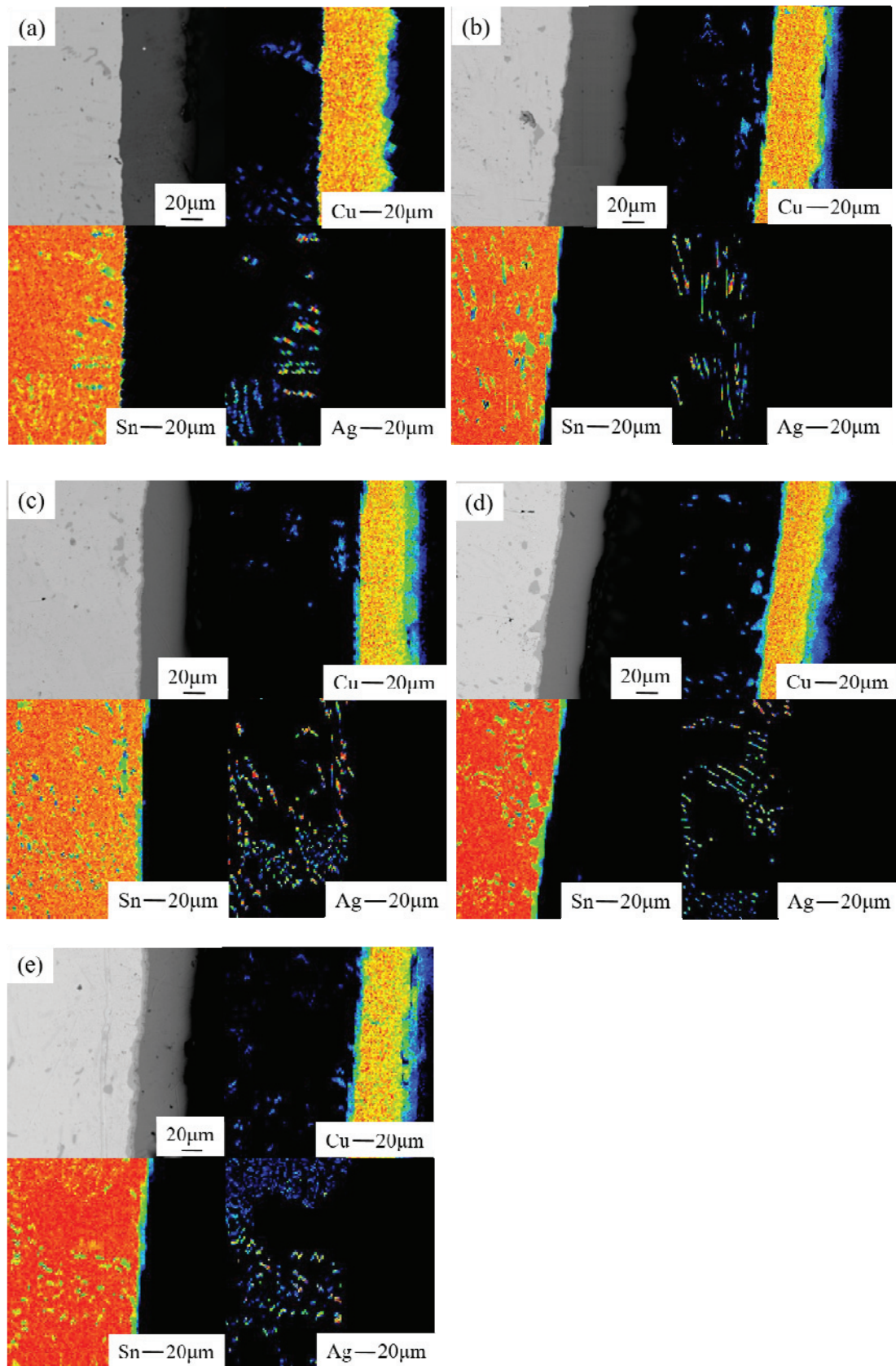


Fig. 4.14 Compositional images and EPMA mappings of Sn-3.0Ag-0.5Cu with Sn coating after (a) 0, (b) 100, (c) 200, (d) 300 and (e) 400 heat cycles.

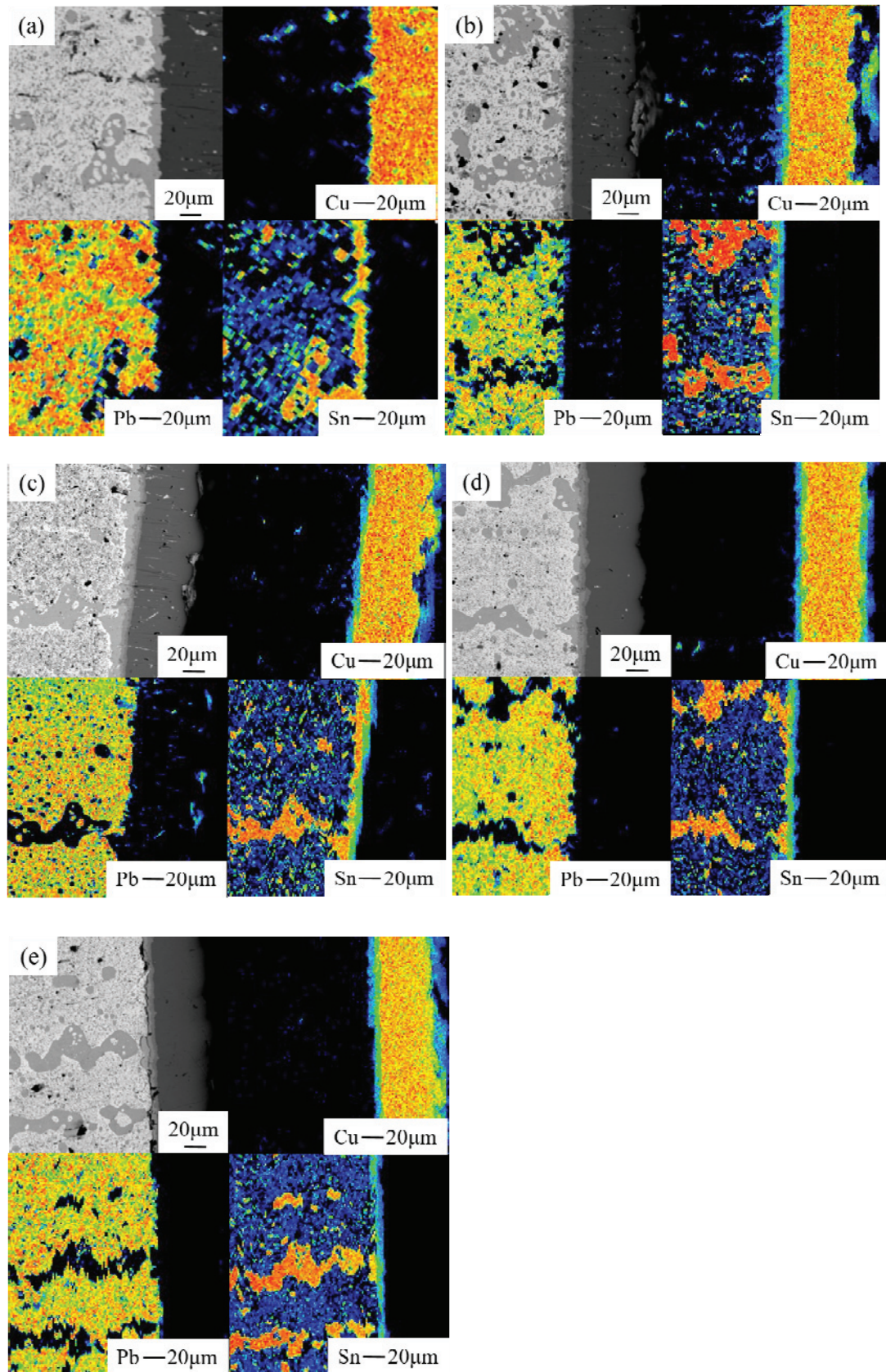


Fig. 4.15 Compositional images and EPMA mappings of Pb-20Sn with Sn coating after (a) 0, (b) 100, (c) 200, (d) 300 and (e) 400 heat cycles.

Table 4.3 The IMC phases for diffusion couples after 100 heat cycle.

Test alloys (mass.%)	Plating process of substrate	IMC phases
Bi-5.0Ag-0.5Cu	Bi	--
	Sn	Cu ₆ Sn ₅ , Cu ₃ Sn
Sn-3.0Ag-0.5Cu		Cu ₆ Sn ₅ , Cu ₃ Sn
Pb-20Sn		Cu ₆ Sn ₅ , Cu ₃ Sn

4.3.1.3 Growth behavior of intermetallic compounds

The statistics of the thickness of the IMC layer at the reaction interface can be used to obtain the regularity of the average thickness of the IMC layer and the heat cycles. Figure 4.16 shows the relation between average thickness of IMC layers and cycle time for Bi-5.0Ag-0.5Cu, Sn-3.0Ag-0.5Cu and Pb-20Sn with Sn coating on Cu substrate. It can be seen that the thickness of the IMC layer of these 3 alloys with Sn coating increased with increasing cycle time. At the beginning of cycle, the growth rate of the IMC layer is fast, and then it decreases with the increasing cycle time. Sn-3.0Ag-0.5Cu with Sn coating shows fastest growth rate and largest thickness of IMC layer in these three alloys.

In the initial stage of heat cycling, the thickness of the IMC layer is relatively thin, which has little effect on the diffusion of Cu and Sn atoms. However, as the increasing cycle time, the thickness of the IMC layer gradually increases, which starts to slow the diffusion rate of the two atoms, and the growth rate of the IMC layer also slows down. When the diffusion rate of the two elements is reduced to a critical value, the thickness of the IMC layer changes very little.

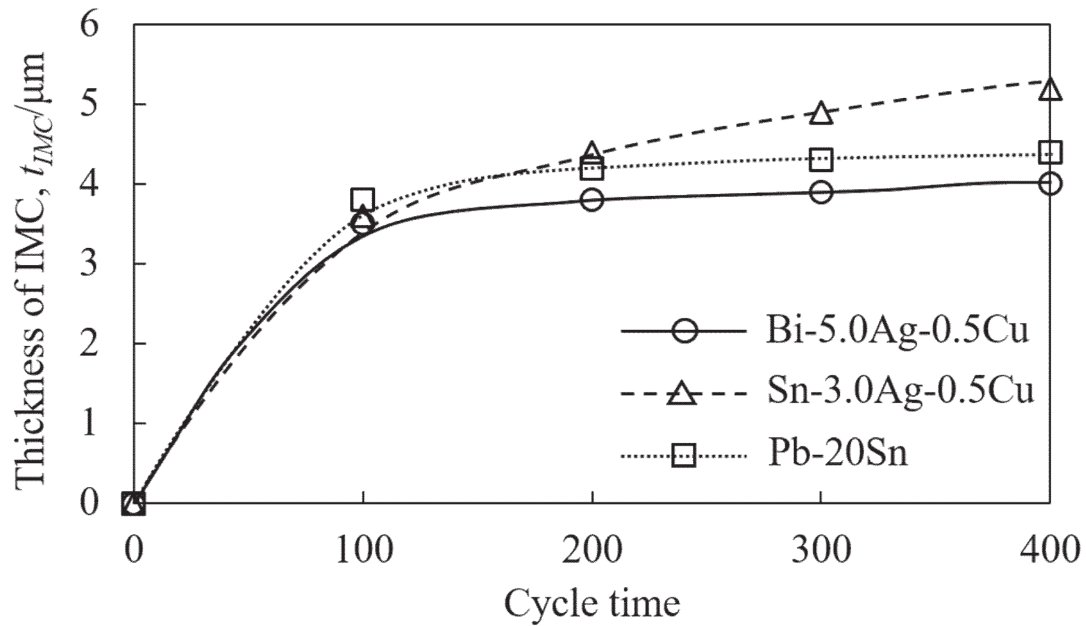


Fig. 4.16 Relation between average thickness of IMC layers and cycle time for Bi-5.0Ag-0.5Cu, Sn-3.0Ag-0.5Cu and Pb-20Sn with Sn coating.

Figure 4.17 shows the compositional images of Bi-5.0Ag-0.5Cu with Bi coating, Bi-5.0Ag-0.5Cu with Sn coating, Sn-3.0Ag-0.5Cu with Sn coating and Pb-20Sn with Sn coating diffusion couples after 200 cycle. With the growth of IMC layer, Bi-5.0Ag-0.5Cu, Sn-3.0Ag-0.5Cu and Pb-20Sn with Sn coating shows void and crack near the formed IMC layer. Bi-5.0Ag-0.5Cu with Bi coating confirms a better morphology at the interface, which shows no IMC layer and crack after 200 cycle. Further, as shown in Fig. 4.18, there are cracks on the interface of Bi coating and Cu substrate after 400 cycle. The void and crack on the IMC layer caused the cracks on the solder joint as mentioned in the term 4.3.1.1. Thus, it can be considered that Bi-5.0Ag-0.5Cu with Bi coating exhibited better thermal fatigue resistance characteristics compared with these 3 alloys with Sn coating.

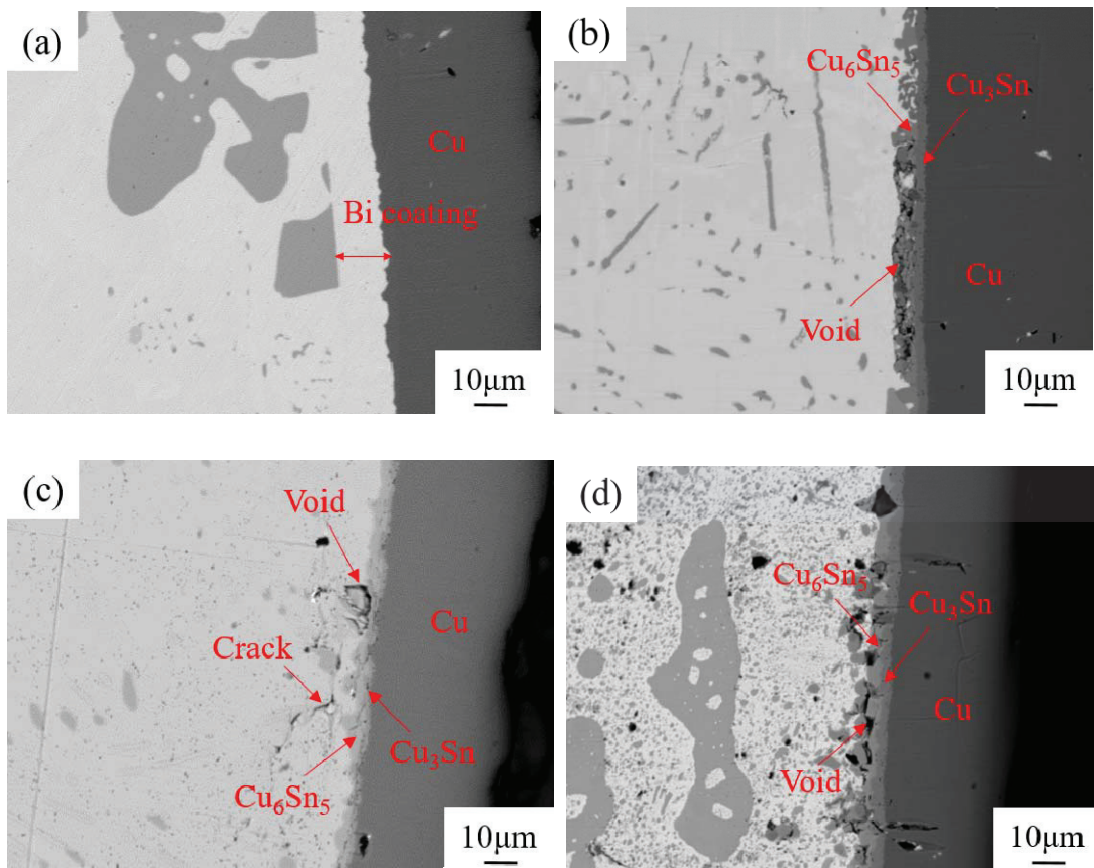


Fig. 4.17 Compositional images of (a) Bi-5.0Ag-0.5Cu with Bi coating, (b) Bi-5.0Ag-0.5Cu with Sn coating, (c) Sn-3.0Ag-0.5Cu with Sn coating and (d) Pb-20Sn with Sn coating diffusion couples after 200 heat cycle.

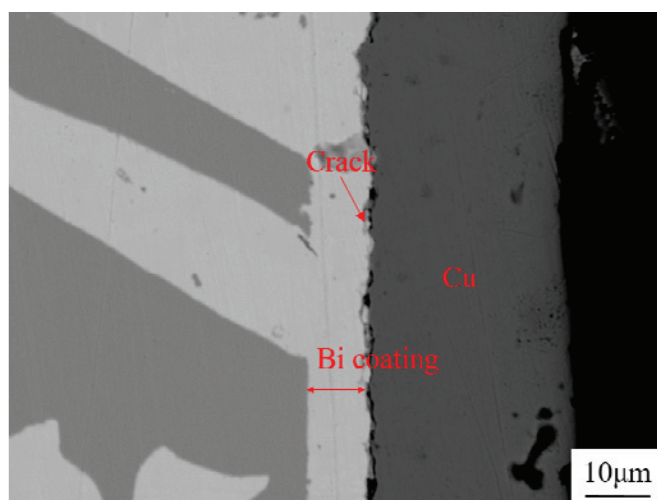


Fig. 4.18 Compositional images of Bi-5.0Ag-0.5Cu with Bi coating diffusion couples after 400 cycle.

4.3.1.4 Diffusion mechanism between solder alloys and Cu

In the heat cycle, the diffusion reactions occurring in the diffusion couples of Bi-5.0Ag-0.5Cu, Sn-3.0Ag-0.5Cu and Pb-20 with Sn coating are ¹⁹⁾:

Interface of Cu₃Sn/Cu (The elements in brackets represent diffuse elements):



Interface of Cu₆Sn₅/Cu₃Sn:



Interface of Cu₆Sn₅/Cu₃Sn:



Interface of solder/ Cu₆Sn₅:



Figure 4.19 shows the diffusion reaction between solder alloys and Cu substrate with Sn coating. At the Cu₃Sn/Cu interface, Cu atoms leave the substrate, some directly participate in the interfacial reaction to form the Cu₃Sn phase, and the other part diffuses into the Cu₃Sn layer. Diffusion and reaction at the interface of Cu₆Sn₅/Cu₃Sn are more complicated. Equations (4-2) to (4-5) jointly express a dynamic diffusion reaction process: The Cu₆Sn₅ phase at the interface can react with Cu atoms from the substrate to form the Cu₃Sn phase, and can also be directly decomposed into Sn atoms and Cu₃Sn phases. The decomposed Sn atoms can diffuse into the Cu₃Sn/Cu interface to participate in the reaction. At the same time, the Cu₃Sn phase at the interface not only reacts with the Sn atoms from the solder matrix to form the Cu₆Sn₅ phase, but also decomposes into Cu atoms and Cu₆Sn₅ phases. This part of the Cu atoms can diffuse into the Solder/Cu₆Sn₅ interface and participate in the reaction. Equations (4-2), (4-3) and (4-4), (4-5) are reciprocal reactions. In the actual reaction process, there will eventually be two dominant reaction modes, so that the reaction proceeds in one direction, that is, the Cu₆Sn₅/Cu₃Sn interface will migrate to the substrate or the solder side. At the solder/Cu₆Sn₅ interface, part of the Sn released from the solder matrix reacts to form the Cu₆Sn₅ phase, and the other part diffuses into the Cu₆Sn₅ layer.

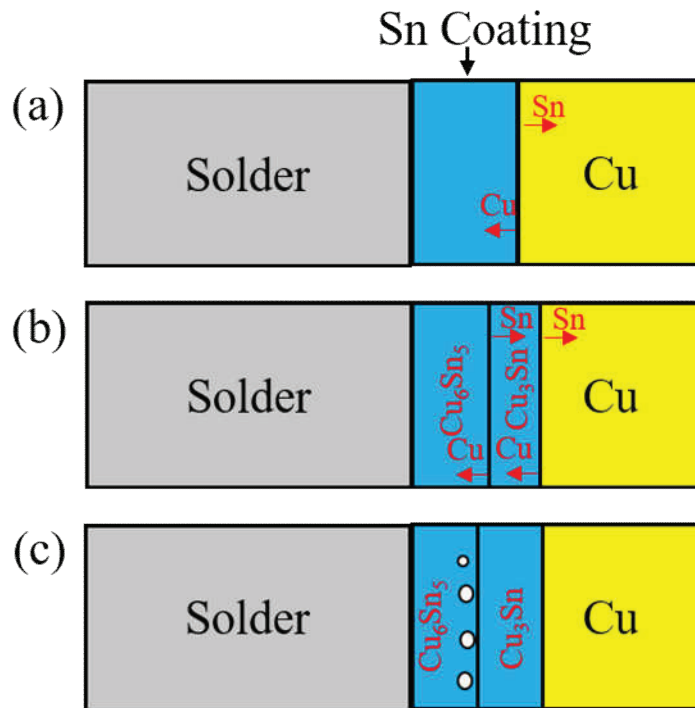


Fig. 4.19 Schematic diagrams of diffusion between solder alloys and Cu substrate with Sn coating.

In Sn coating diffusion couples, the thickness of Sn coating is limited, Cu atoms can diffuse from the reaction interface to the other side of the Sn coating in a relatively short time, so the Sn coating is quickly consumed and converted into a Cu_6Sn_5 phase. With the increasing cycle time, the Cu substrate is continuously consumed, the $\text{Cu}_3\text{Sn}/\text{Cu}$ interface continues to migrate to the substrate side as shown in Fig. 4.19 (b). And after the Sn coating is completely converted to Cu_6Sn_5 , the Cu_6Sn_5 phase transition to Cu_3Sn phase occurs at $\text{Cu}_6\text{Sn}_5/\text{Cu}_3\text{Sn}$ interface, the $\text{Cu}_6\text{Sn}_5/\text{Cu}_3\text{Sn}$ interface migrate to the Cu_6Sn_5 side. The limited Sn content causes the lower growth rate and thickness of IMC layer. In the initial stage of heat cycle, the diffusion rate of Cu and Sn at the interface is faster, and the growth rate of Cu_6Sn_5 layer is also faster. The thickening of the Cu_6Sn_5 layer retards the diffusion of Cu and Sn. With the prolongation of heat cycle, the residual amount of Sn coating is getting less and less, so that the diffusion rate of Sn at the interface rapidly decreases, resulting in an increase in the unbalanced diffusion of Cu and Sn. Therefore, a small amount voids are formed at the IMC layer as shown in Fig.

4.19 (c). The schematic diagram shown in Fig. 4.19 is consistent with the EPMA results in 4.3.1.2 and 4.3.1.3.

Because of the unbalanced diffusion of Sn and Cu, there were some voids occurred near the IMC layer of Bi-5.0Ag-0.5Cu, Sn-3.0Ag-0.5Cu and Pb-20Sn diffusion couples with Sn coating, as shown in Fig. 4.17. The formed voids lead to the lower bonding strength between the solder joints and substrate. Moreover, the formation and growth of the IMC phase at the reaction interface can cause local volume changes, resulting in the residual stresses on the diffusion reaction area. As listed in Table 4.4, the mismatched thermal expansion causes thermal stress in the solder joints. The residual and thermal stresses lead to the cracks occurrence near the voids in the diffusion couples. The voids and cracks make great influence on the failure of solder joints. On the other hand, because of the no IMC layer and the lower difference value of coefficient of thermal expansion between Bi-5.0Ag-0.5Cu and Cu substrate with Bi coating, the cracks on the interface between the Cu substrate and Bi coating occurred latest after 400 cycle, as shown in Fig. 4.18.

Table 4.4 The coefficient of thermal expansion for solder alloys, IMC and Cu.

Alloy (mass.%)	CTE (K ⁻¹)
Bi-5.0Ag-0.5Cu	13.4×10 ⁻⁶
Sn-3.0Ag-0.5Cu	25.4×10 ⁻⁶
Pb-20Sn	27.0×10 ⁻⁶
Cu ₆ Sn ₅ ²⁰⁾	16.3×10 ⁻⁶
Cu ₃ Sn ²⁰⁾	19.0×10 ⁻⁶
Cu ²⁰⁾	17.7×10 ⁻⁶

4.3.2 Shearing test of Bi-5.0Ag-0.5Cu and Cu substrates with Bi coating

Two Cu substrates with Bi coating were joined by the melting Bi-5.0Ag-0.5Cu solder alloy. Figure 4.20 shows photographs of the shearing test pieces of Bi-5.0Ag-0.5Cu alloy and Cu substrates. From this figure, it can be confirmed that this alloy is satisfactorily jointing to the Cu substrates with Bi coating.

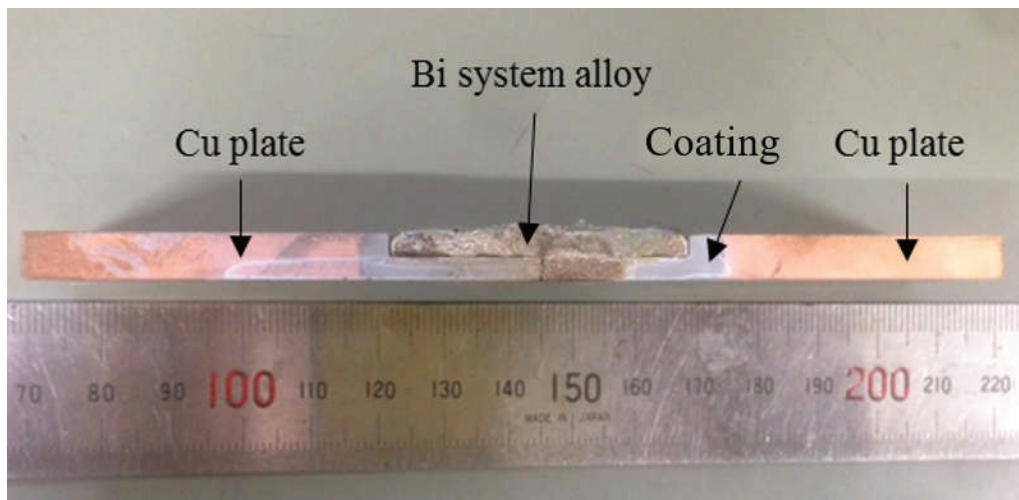
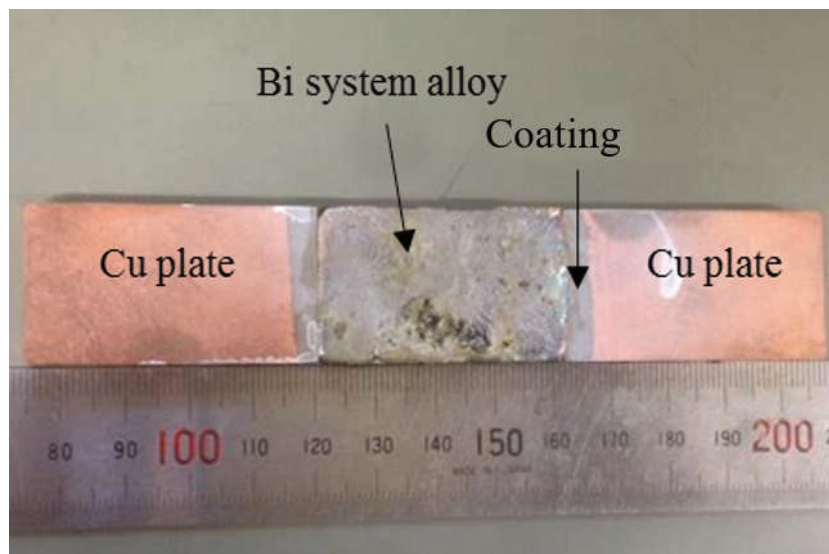


Fig. 4.20 Photographs of Bi-5.0Ag-0.5Cu and Cu substrates with Bi coating after soldering.

The photograph after shearing test are shown in Fig. 4.21. The test piece does not break at the interface with the Cu substrate, but on the soldered alloy. The solder joint

does not peel off from the Cu substrates until the allowable stress of the alloy was reached.

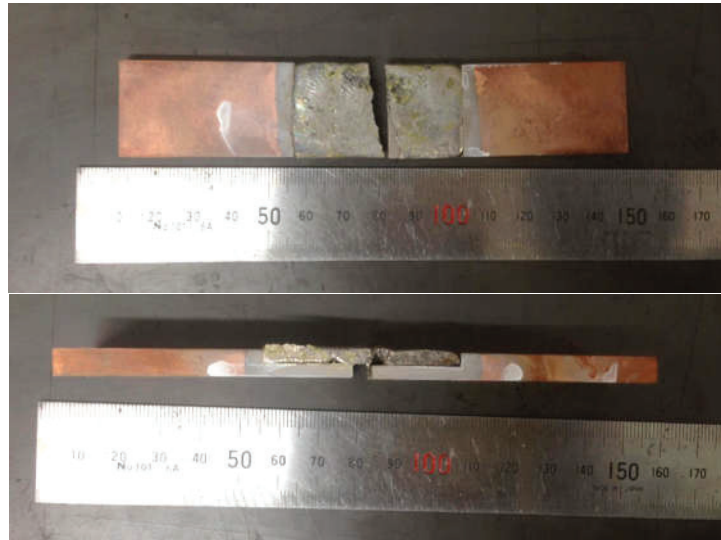


Fig. 4.21 Photographs of Bi-5.0Ag-0.5Cu and Cu substrates with Bi coating after shearing test.

The load-time curve for shearing test and stress-strain curve for tensile test of Bi-5.0Ag-0.5Cu alloy at 293 K are shown in Fig. 4.21. The dimensions of the gauge section of the tensile test specimens were 6 mm (diameter) \times 20 mm (length), which mentioned in chapter 2. Table 4.5 lists the ultimate tensile strength, maximum load and fracture strain obtained by the shearing test and the tensile test. The maximum load of shearing test is higher than tensile test. It can be confirmed that Bi-5.0Ag-0.5Cu was well jointed to the Cu substrates with Bi coating and the shearing strength between Bi-5.0Ag-0.5Cu and Cu substrates with Bi coating can afford the practical applications.

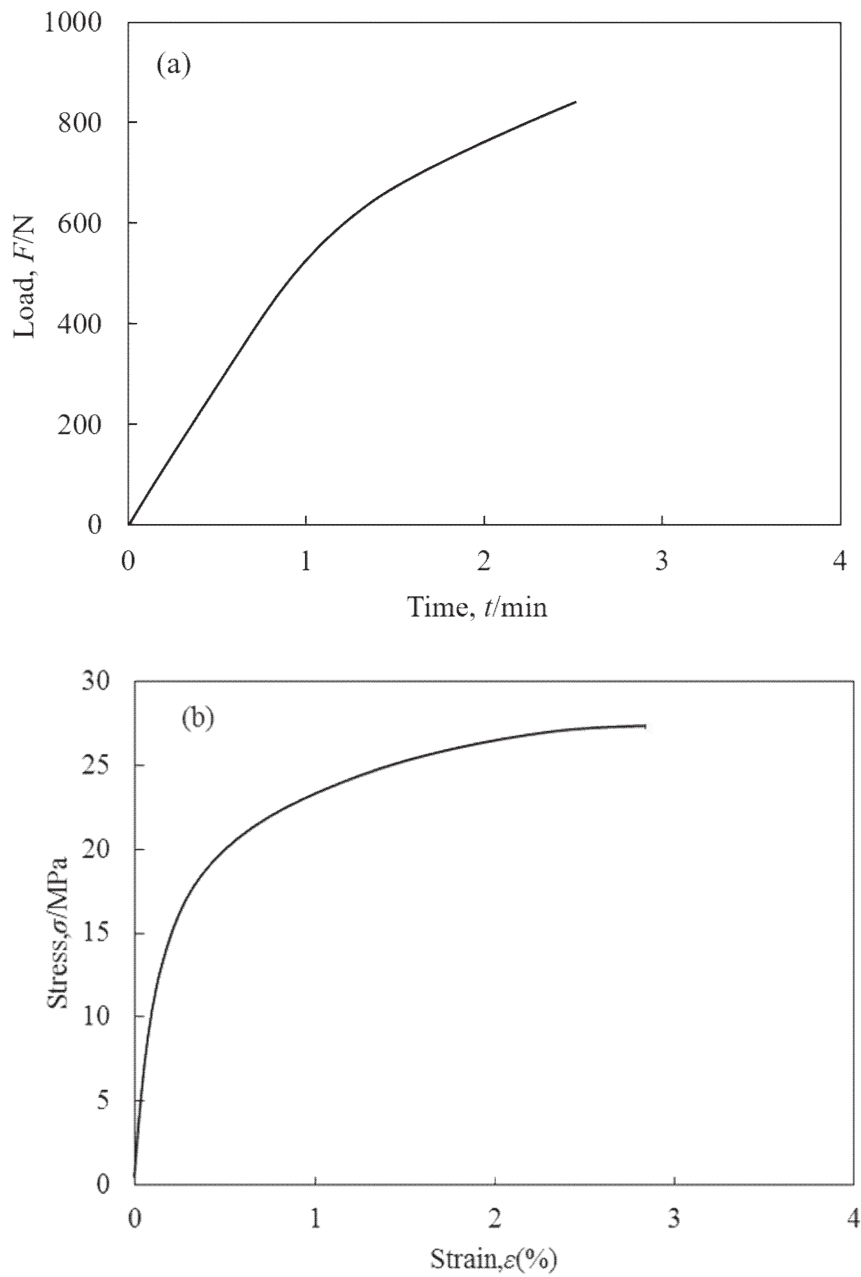


Fig. 4.21 (a) Load-time curve of shearing test and (b) stress-strain curve of tensile test for Bi-5.0Ag-0.5Cu alloy.

Table 4.5 Mechanical properties of shearing and tensile test for Bi-5.0Ag-0.5Cu alloy.

Alloy (mass.%)	Tests	σ_{UTS} (MPa)	F_{max} (N)	ϵ (%)
Bi-5.0Ag-0.5Cu	Shearing test	--	817.1	--
	Tensile test	27.3	771.5	2.8

4.3.3 Comparison between promising alloys and Pb-xSn alloys in view of soldering

Bi-2.0Ag-0.5Cu and Bi-5.0Ag-0.5Cu are the promising designed alloys according to the results show in Chapter 3. Table 4.6 shows the mechanical, physical and thermal properties of Bi-2.0Ag-0.5Cu, Bi-5.0Ag-0.5Cu and Pb-xSn alloys.

Table 4.6 Mechanical and thermal properties of Bi-2.0Ag-0.5Cu, Bi-5.0Ag-0.5Cu and Pb-xSn alloys.

Alloys (mass. %)	σ_{UTS} (MPa)	ε (%)	Melting point (K)	Contact angle (degree)	λ (W·K ⁻¹ ·m ⁻¹)
Bi-2.0Ag-0.5Cu	21.7	4.7	536	28	18.7
Bi-5.0Ag-0.5Cu	27.3	2.8	538	30	19.1
Pb-5Sn	22.1	38.6	544	22	35.5
Pb-10Sn	24.3	18.7	540	20	37.1
Pb-20Sn	26.7	16.8	457	20	40.2

The ultimate tensile strength were almost same level among these alloys. The two promising Bi alloys show the ultimate tensile strength higher than the target value of 20MPa. However, the fracture strain of Pb-5Sn, Pb-10Sn and Pb-20Sn alloys were 38.6, 18.7 and 16.8 %, respectively, which were much higher than Bi-2Ag-0.5Cu and Bi-5.0Ag-0.5Cu. The ductility of proposed Bi alloys should be improved. The melting points of Bi-2Ag-0.5Cu and Bi-5.0Ag-0.5Cu solder alloys were measured to be 536 and 538 K, respectively. It is considered on the basis of the practical application that the melting temperature above 533 K was satisfied in the proposed Bi system alloy. The contact angles of Bi-2Ag-0.5Cu, Bi-5.0Ag-0.5Cu, Pb-5Sn, Pb-10Sn and Pb-20Sn to Cu plate were 28, 30, 22, 20 and 20 degree, respectively. Although the contact angle of Bi-2Ag-0.5Cu was the largest, but this value was less than 90 degree. The λ values of the

designed alloys were lower than those of the Pb-Sn alloy. However, the λ values of the promising alloys need to be increased further in order for the alloys to be practically applicable.

4.4 Summary

(1) It is found that there was no diffusion reaction between Bi-5.0Ag-0.5Cu with Bi coating and Cu substrate, however, the diffusion reaction between Bi-5.0Ag-0.5Cu, Sn-3.0Ag-0.5Cu and Pb-20Sn with Sn coating and Cu substrate formed the IMC layer of Cu_6Sn_5 and Cu_3Sn after 100 heat cycle.

(2) In the three diffusion couples of Bi-5.0Ag-0.5Cu, Sn-3.0Ag-0.5Cu and Pb-20Sn with Sn coating and Cu substrate, the thickness of the IMC layer increases with the heat cycle time, and then gradually stabilizes. The thickening of the IMC layer inhibits the diffusion of the two elements, which retarding the growth of the IMC layer itself.

(3) With the prolongation of heat cycle, voids occurs on the formed IMC layer. The unbalanced diffusion of Cu and Sn causes voids at the IMC layer. And the different thermal expansion causes the cracks occurrence near the voids in the diffusion couples. That has a great influence on the failure of solder joints.

(4) The shearing test piece of Bi-5.0Ag-0.5Cu and Cu substrates with Bi coating break on the soldered alloy, the shearing strength can afford the practical applications. The values in the mechanical and thermal properties of promising Bi alloys can almost reach the target value compared to those on practically Pb-Sn alloys.

References

- 1) Y. Gu, and B. Yang: *Journal of Functional Materials* **36** (2005) 490-494.
- 2) E. B. Liao, A. A. O. Tay, and S. S. T. Ang: *IEEE Transactions on Components and Packaging Technologies* **29** (2006) 560-569.
- 3) C. K. Wong, J. H. Pang, J. W. Tew: *Microelectronics Reliability* **48** (2008) 611–621.
- 4) Z. Huang, P. P. Conway and E. Jung: *Journal of Electronic Materials* **35** (2006), 1761–1772.
- 5) H. Lu, Y. Takagi, and Y. Suzuki: 2014 IEEE 64th Electronic Components and Technology Conference (ECTC). IEEE, 2014: 1416-1420.
- 6) H. Y. Son, G. J. Jung, B. J. Park and K. W. Paik: *J. Electron. Mater.* **37** (2008) 1832–1842.
- 7) D. A. Shnawah, M. F. Sabri, and I. A. Badruddin: *Microelectronics Reliability* **52** (2012) 90–99.
- 8) Y. Tian, C. Hang, and C. Wang: *Mater. Sci. Eng. A* **529** (2011) 468–478.
- 9) X. Y. Li, F. H. Li, and F. Guo: *J. Electron. Mater.* **40** (2011) 51–61.
- 10) J. Chen, Y. S. Lai and C. Y. Ren: *Appli. Phys. Letters* **92** (2008) 901-903.
- 11) J. O. S. Amistoso, and V. A. J. Morsolo: *IEEE Transactions on Components and Packaging Technologies* **32** (2009) 405–414.
- 12) L. H. Xu and H. L. P. John: Piscataway, IEEE. (2006).
- 13) L. H. Xu, H. L. P. John and F. X. Che: Piscataway, IEEE. (2005).
- 14) W. Bang, M. W. Moon and C. U. Kim: *J. Electron. Mater.* **37** (2008) 417-428.
- 15) C. T. Peng, K. N. Chiang and T. Ku: *Microelectronics Reliability* **46** (2006) 523-523.
- 16) Y. M. Ryu, E. P. Yoon, and M. H. Rhee: *J. Mater. Sci. Lett.* **19** (2000) 1103–1105.
- 17) H. T. Lee, M. H. Chen and H. M. Jao: *Mater. Sci. Eng. A* **358** (2003) 134–141.
- 18) F. Guo, J. P. Lucas, K. N. Subramanian: *J. Mater. Sci.* **12** (2001) 27–35.
- 19) A. Paul: Doctoral dissertation, Technical University of Eindhoven (2004).
- 20) J. Nan, J. A. Clum and R. R. Chromik: *Scripta Materialia* **37** (1997) 1851-1854.

Conclusions

In this research, Bi system alloys were selected as a candidate for a high temperature lead-free solder alloys and promising alloys were developed for practical applications. The compositions of this alloy have been proposed using ΔMk parameter, the compositional average of s-orbital energy level (Mk) in order to satisfy the mechanical properties as solders. Moreover, ultimate tensile strength and fracture strain at room temperature higher than 20 MPa and 5%, respectively, and melting point over 533 K, thermal conductivity over $20 \text{ W} \cdot \text{K}^{-1} \cdot \text{m}^{-1}$, contact angle less than 90 degree were chosen as target values of various characteristics. The conclusions of this thesis are summarized as follows:

1. Cu, Ag and Zn were chosen as binary elements in Bi system alloys, their alloys with compositions near the eutectic and their values of ΔMk were from 0.013 to 0.343. The ultimate tensile strength and fracture strain were higher than those of pure Bi. The 0.2% proof stress, ultimate tensile strength of binary Bi system alloys were increased with increasing of ΔMk until approximately 0.17, regardless of the kinds and amount of alloying elements. Then the ultimate tensile strength became to almost constant in the range of ΔMk more than 0.17. In contrast, the maximum values, 25 and 33%, in the fracture strain were shown in Bi-0.25Cu and -0.5Cu alloys with ΔMk of 0.021 and 0.042, respectively. The mechanical properties such as tension and hardness were roughly predicted by the values of ΔMk . Moreover, the proposed Bi-2.0Ag-0.5Cu and Bi-5.0Ag-0.5Cu with ΔMk of 0.180 and 0.379 as ternary alloys, respectively, showed the improved tension and hardness properties, compared with pure Bi. It is found that their ultimate tensile strength, fracture strain and hardness values even in ternary Bi system alloys, could be also predicted using their estimation lines obtained from binary Bi system alloys.

2. It was found that the 0.2% proof stress, ultimate tensile strength, and fracture strain of the designed binary Bi system alloys at 423 K were higher than those of pure Bi. The 0.2% proof stress and ultimate tensile strength of the binary Bi system alloys increased with an increase in ΔMk till approximately 0.17 and then remained almost constant. In contrast, the fracture strain increased with an increase ΔMk till approximately 0.08 and then remained almost constant. The binary Bi system alloys exhibited excellent ductility, showing a fracture strain of more than 30% at 423 K. The relationship between the strength at 423 K and ΔMk was similar to that observed during tests at 293 K. The compositionally optimized alloys Bi-2.0Ag-0.5Cu and Bi-5.0Ag-0.5Cu also showed improved tensile properties at 423 K as compared to those of pure Bi and the binary Bi-Cu alloys. Moreover, a transition from ductility to brittleness was observed at approximately 348–373 K in the case of both ternary alloys. It was found that the manner in which the mechanical properties of alloys can be predicted based on the ΔMk value would also be applicable in the case of the Bi system alloys investigated in this study, regardless of their composition and the tensile test temperature.

3. The melting points of the alloys Bi-2.0Ag-0.5Cu and Bi-5.0Ag-0.5Cu were determined to be 536 and 538 K, respectively; these were within the desired range of melting temperatures for high-temperature solders. Further, the contact angles of molten droplets of 10 of the binary and ternary experimental alloys and a Cu plate at 973 K were determined to be 24–30 degree. This confirmed that the alloys exhibited suitable wettability with respect to Cu in soldering. In addition, the ternary alloys, Bi-2.0Ag-0.5Cu and Bi-5.0Ag-0.5Cu showed thermal conductivities of 18.7 and 19.1 $\text{W} \cdot \text{K}^{-1} \cdot \text{m}^{-1}$, respectively.

4. The diffusion reaction between Bi-5.0Ag-0.5Cu, Sn-3.0Ag-0.5Cu or Pb-20Sn and Cu substrate with Sn coating revealed the formation of Cu_6Sn_5 and Cu_3Sn intermetallic compounds (IMC) after 100 heat cycle. The thickness of IMC layer increases with the increasing cycle time, and the growth rate of the IMC layer decreases with the increasing cycle time. The unbalanced diffusion of Cu and Sn caused the voids on the formed IMC layer. Moreover, significant change of volume and the mismatched thermal expansion lead to the cracks occurrence near the voids in the diffusion couples. That has a great influence on the failure of solder joints. Bi-5.0Ag-0.5Cu and Cu

substrate with Bi coating shows the cracks on the interface between the Cu substrate and Bi coating occurred latest after 400 cycle. It can be considered that Bi-5.0Ag-0.5Cu with Bi coating exhibited excellent thermal fatigue resistance characteristics compared with these 3 alloys with Sn coating. The shearing test piece of Bi-5.0Ag-0.5Cu and Cu substrates with Bi coating break on the soldered alloy. It can be confirmed that Bi-5.0Ag-0.5Cu was well soldered to the Cu substrates with Bi coating and the shearing strength between Bi-5.0Ag-0.5Cu and Cu substrates with Bi coating can afford the practical applications. The values in the strength of promising Bi alloys were similar to those on practically Pb-Sn alloys, and the melting points and contact angles also satisfied for the practical application. The ductility and thermal conductivity should be improved compare with the practically Pb-Sn alloys.

Acknowledgements

I would like to express my sincere gratitude to Professor Kazuhiro Matsugi for his great guidance and insight throughout this study. He gave me full support not only on my research, but also on my life and career, which has played an important role in both of my professional and personal development. I am also greatly indebted Assistant Professor Yongbum Choi and Assistant Professor Zhefeng Xu. They gave me so much positive help on the research, the accumulation of the knowledge and my life, and I have learnt so much from them. In addition, I would like to express my heartfelt thanks to Professor Gen Sasaki, Professor Atsushi Sugeta, Associate Professor Kenjiro Sugio, and Associate Professor Hiroyuki Akebono for their technical advice and experimental assistance. I would like to acknowledge the helpful comments and suggestions from Professor Ken-ichiro Suetsugu, Kobe University and Professor Satoshi Motozuka, Gifu College. The heat cycle test is supported by OM Sangyo Co. Ltd. and IDEC Corporation.

I would like to thank Mr. Shaoming Kang, Mr. Takuma Konishi, Mr. Youki Yagi, Mr. Yuto Yoshida and Mr. Yuki Ogawa for considerable assistance and help in my experiments and my life. Moreover, I would also like to thank all the past and present members of Property Control of Materials Laboratory, in Department of Mechanical Physical Engineering, Hiroshima University, for their enthusiastic help to both of my life and study.

Then, my thanks would go to my beloved family for their loving considerations and great confidence in me all through these years. I also owe my sincere gratitude to my friends who gave me their help and time in helping me work out my problems during the difficult course of the thesis.

Finally, I would like to thank to China Scholarship Council for three years scholarship to support my research and life in Japan.

Published papers in regards to this thesis

1. **M. Q. Yu**, Z. F. Xu*, Y. B. Choi, T. Konishi, K. Matsugi, J. K. Yu, S. Motozuka, K. Suetsugu. Tensile properties of Bi alloys and a case study for alloy Design in their application to high temperature solder. *Materials transactions*. 2017(58)2: 140-147. (Chapter 2 & 3)
2. **M. Q. Yu**, K. Matsugi, Z. F. Xu*, Y. B. Choi, J. K. Yu, S. Motozuka, Y. Nishimura, K. Suetsugu. High temperature characterization of binary and ternary Bi alloys microalloyed with Cu and Ag. *Materials transactions*. 2018(59)2: 303-310. (Chapter 2 & 3)
3. **M. Q. Yu**, Z. F. Xu*, Y. B. Choi, K. Matsugi, S. Motozuka, K. Suetsugu, J. K. Yu. Some properties of the compositional optimized Bi-2Ag-0.5Cu alloy for high temperature solders. *The Ninth Pacific Rim International Conference on Advanced Materials and Processing (PRICM9)*, Ed. by T. Furuhashi, M. Nishida and S. Miura, The Japan Institute of Metals and Materials, 2016: 225-230. (Chapter 4)

Presentations

1. **Meiqi Yu**, Zhefeng Xu, Yong Bum Choi, Kazuhiro Matsugi, Satoshi Motozuka, Ken-ichiro Suetsugu and Jinku Yu. Some Properties of the Compositional Optimized Bi-2Ag-0.5Cu Alloy for High Temperature Solders. The Ninth Pacific Rim International Conference; August 1-5, 2016, Kyoto, Japan; Kyoto International Conference Center

2. **Meiqi Yu**, Zhefeng Xu, Yong Bum Choi, Kazuhiro Matsugi, Satoshi Motozuka, Ken-ichiro Suetsugu and Jinku Yu. Design of Bi System Alloys for High Temperature Solders and Their Mechanical Properties. 日本鉄鋼協会・日本金属学会中国四国支部鉄鋼第59回・金属第56回合同講演大会 August 22, 2016, Shimane, Japan ; Shimane University

3. 許哲峰、于美琪、八木祐樹、崔龍範、松木一弘、本塚智、末次憲一郎. 鉛フリー高温はんだ用Bi系合金の設計と高温特性. 日本鑄造工学会第168回全国講演大会 2016年9月23日（金）～26日（月）, 高知市文化プラザかるぼーと

4. **Meiqi Yu**, Kazuhiro Matsugi, Zhefeng Xu, Yong Bum Choi, Jinku Yu, Satoshi Motozuka, Ken-ichiro Suetsugu. Some Properties of the Bi System Alloys at High Temperature. 日本金属学会2017年(第160回)春期講演大会. March 15-17, 2017, Tokyo, Japan; Tokyo Metropolitan University

5. Yuto Yoshida, Kazuhiro Matsugi, Yongbum Choi, Zhefeng Xu, **Meiqi Yu**, Ken-ichiro Suetsugu, Satoshi Motoduka. Design and characterization of Bi alloy for high temperature soldering. 第30回DV-X α 研究会, 2017年8月3-4日, 兵庫県立大学姫路工学キャンパス.

6. **Meiqi Yu**, Kazuhiro Matsugi, Zhefeng Xu, Yongbum Choi, Jinku Yu, Satoshi Motozuka, Ken-ichiro Suetsugu. Some Properties of Ternary Bi System Alloys with Optimized Compositions. 日本鉄鋼協会・日本金属学会 中国四国支部 鉄鋼第59回・金属第57回 合同講演大会. August 21, 2017, Kochi, Japan; Kochi University of Technology

7. **Meiqi Yu**, Kazuhiro Matsugi, Yongbum Choi, Jinku Yu, Satoshi Motozuka, Ken-ichiro Suetsugu and Zhefeng Xu. Design and Development of Bi System Alloys for

High Temperature Solders. The 3rd International Symposium on Metastable Materials
Science & Technology in Qnhuangdao, China, 12-16 Oct. 2017